

AD-A046 342

LOCKHEED-GEORGIA CO MARIETTA
FURTHER DEVELOPMENT OF A VISCOUS VORTEX/WING INTERACTION PROGRAM--ETC(U)
JUN 77 C J DIXON , R M SCRUGGS

F/6 20/4

N00014-74-C-0151

UNCLASSIFIED

TOP 2
AD
A046342

L677ER0209

ONR-CR215-233-3

NL



AD No.
DDC FILE COPY

ADA046342



REPORT ONR-CR215-233-3

FURTHER DEVELOPMENT OF A VISCOUS VORTEX/WING INTERACTION PROGRAM.

CHARLES J. DIXON
Lockheed-Georgia Co.,
Marietta, Georgia

ROY M. SCRUGGS
Sybucor, Inc.

CONTRACT NO 00014-74-C-0151
ONR TASK 215-233

NOV 14 1977

Approved for public release: distribution unlimited.

PREPARED FOR THE

OFFICE OF NAVAL RESEARCH • 800 N. QUINCY ST. • ARLINGTON • VA • 22217



210065

100

UNCLASSIFIED

SECURITY CLASSIFICATION OF THIS PAGE (When Data Entered)

REPORT DOCUMENTATION PAGE		READ INSTRUCTIONS BEFORE COMPLETING FORM
1. REPORT NUMBER ONR CR215-233-3	2. GOVT ACCESSION NO.	3. RECIPIENT'S CATALOG NUMBER
4. TITLE (and Subtitle) FURTHER DEVELOPMENT OF A VISCOUS VORTEX/WING INTERACTION PROGRAM		5. TYPE OF REPORT & PERIOD COVERED Interim Technical Report 1 July 76 - 31 May 77
7. AUTHOR(s) C. J. Dixon Roy M. Scruggs		6. PERFORMING ORG. REPORT NUMBER LG77ER0209
9. PERFORMING ORGANIZATION NAME AND ADDRESS Lockheed-Georgia Company, Marietta GA 30063 Sybucon, Inc., Atlanta, GA		8. CONTRACT OR GRANT NUMBER(s) N00014-74-C-0151
11. CONTROLLING OFFICE NAME AND ADDRESS Office of Naval Research Vehicle Technology Program, Code 211 800 N. Quincy Street, Arlington, Va. 22217		10. PROGRAM ELEMENT, PROJECT, TASK AREA & WORK UNIT NUMBERS NR 215-233
14. MONITORING AGENCY NAME & ADDRESS (if different from Controlling Office)		12. REPORT DATE 1 June 1977
		13. NUMBER OF PAGES
		15. SECURITY CLASS. (of this report) Unclassified
		15a. DECLASSIFICATION/DOWNGRADING SCHEDULE
16. DISTRIBUTION STATEMENT (of this Report) Approved for public release; distribution unlimited		
17. DISTRIBUTION STATEMENT (of the abstract entered in Block 20, if different from Report) D D C REFACILIFIED NOV 14 1977 REFUGITIVE B		
18. SUPPLEMENTARY NOTES		
19. KEY WORDS (Continue on reverse side if necessary and identify by block number) Vortex Lift, vortex control, viscous mixing, Navier-Stokes, computational fluid mechanics, delta wings, high angle of attack, laser velocimeter		
20. ABSTRACT (Continue on reverse side if necessary and identify by block number) A computational fluid mechanical model developed for analyzing the loads and flow mechanism due to vortex/wing interactions has been further improved and evaluated. The model provides vorticity, velocity vectors, and pressures for viscous flow on the upper surface of the wing with a leading edge vortex. Viscous parametric investigations have been conducted showing the effects of such parameters as leading edge sweep, leading edge feeding vorticity, and (Continued on reverse)		

UNCLASSIFIED

SECURITY CLASSIFICATION OF THIS PAGE(When Data Entered)

viscosity. Effects of grid size and various boundary conditions are presented.

Boundary conditions are determined from potential flow models by an iteration procedure. Directions and an example of the interaction procedure is presented. A simple 65° delta wing at 22° angle of attack is used for the analyses. Iterations for this model are not complete, but the results are instructive for analyzing other models and completing the 65° wing investigation. The method is not limited to thin delta wings. Arbitrary planforms can be evaluated. Thick wings with rounded leading edges are under current investigation.

Experimental laser velocimeter data are presented for boundary conditions at one station on the 65° delta wing at 22° angle of attack.

deg

deg

ACCESSION NO.	
WHS	Life Section <input checked="" type="checkbox"/>
PDC	Diff. Section <input type="checkbox"/>
UNARMED	<input type="checkbox"/>
JUSTIFICATION	
BY	
DISTRIBUTION/AVAILABILITY CODES	
Dist.	AVAIL. and/or <input checked="" type="checkbox"/> SPECIAL
A	

UNCLASSIFIED

SECURITY CLASSIFICATION OF THIS PAGE(When Data Entered)

PREFACE

This research of the three-dimensional viscous vortex/wing interaction theory was performed under Contract No. N00014-74-C-0151 for the Office of Naval Research. The work was done in the Lockheed-Georgia Company Advanced Flight Sciences Department, managed by Mr. H. R. Leslie. Major contributors to the effort came from consultants Drs. J. F. Nash and R. M. Scruggs of Sybucor, Inc. The program monitor is Dr. R. E. Whithead, Office of Naval Research, Arlington, Va. This work is continuing currently.

SUMMARY

A computational fluid mechanical model developed for analyzing the loads and flow mechanism due to vortex/wing interactions has been further improved and evaluated. The model provides vorticity, velocity vectors, and pressures for viscous flow on the upper surface of a wing with a leading edge vortex. Viscous parametric investigations have been conducted showing the effects of such parameters as leading edge sweep, leading edge feeding vorticity, and viscosity. Effects of grid size and various boundary conditions are presented.

Boundary conditions are determined from potential flow models by an iteration procedure. Directions and an example of the interaction procedure is presented. A simple 65° delta wing at 22° angle of attack is used for the analyses. Iterations for this model are not complete, but the results are instructive for analyzing other models and completing the 65° wing investigation. The method is not limited to thin delta wings. Arbitrary planforms can be evaluated. Thick wings with rounded leading edges are under current investigation.

Experimental laser velocimeter data are presented for boundary conditions at one station on the 65° delta wing at 22° angle of attack.

CONTENTS

	<u>Page</u>
SUMMARY	iv
LIST OF FIGURES	vii
1. INTRODUCTION	1
2. THE VISCOUS MODEL	3
2.1 Further Developments of the Viscous Model	3
2.2 Significance of the Leading Edge Vorticity	8
2.3 Accuracy, Mesh Size, and Viscosity	14
2.4 Effect of Sweep and Flow Angularity at the Leading Edge	16
2.5 Computation of Pressure in the Viscous Region	20
2.6 Iteration and Step-Length Sensitivity	22
3. INTEGRATION OF THE VISCOUS BOX AND ELLIPTIC POTENTIAL FLOW MODELS .	30
3.1 General	30
3.2 Modeling Technique	30
3.3 Approximation of Estimating Vortex Strength and Position . . .	36
3.4 Vortex Lattice Method	43
3.5 Interface Between Different Size Vorticity Boxes	45
3.6 The Leading Edge Problem	50
3.7 Distributed Circulation from Viscous Box Results	55
3.8 Results of First Iteration for Thin Delta Wing	58
4. LASER VELOCIMETER EXPERIMENTS	70
4.1 General Description	70
4.2 The Model, Wind Tunnel, and Seeding	70
4.3 Results of Delta Wing Test	72
5. CONCLUSIONS	75
6. RECOMMENDATIONS	76
REFERENCES	77
LIST OF SYMBOLS	79
APPENDIX: VORTICITY BOX PROGRAM DOCUMENTATION AND TYPICAL OUTPUT . . .	80

LIST OF FIGURES

<u>Figure</u>		<u>Page</u>
1 Augmented Numerical Model	5	5
2 Comparison of First and Second Order Accurate Differencing, ξ -Component	6	6
3 Comparison of First and Second Order Accurate Differencing, W Velocity Component	7	7
4 Simulation of Delta Wing for Green's Function Application . . .	9	9
5 Velocity Vectors and Contours of ξ Component of Vorticity With Simulated Plane of Symmetry	10	10
6 Leading Edge Conditions	12	12
7 Effect of Leading Edge Vorticity on Vorticity Contour	13	13
8 Effect of Mesh Size on Ω and ξ_{\max}	15	15
9 Variation of Ω with v	17	17
10 Effect of Viscosity Coefficient on a Typical Velocity Profile	18	18
11 Schematic of Leading Edge Separation as a Function of Leading Edge Shape	19	19
12 Effect of Angular Position of Leading Edge Vorticity	21	21
13 Pressure Coefficient Contours	23	23
14 Iteration History of Starting Solution for X-Step of 10^6 . . .	25	25
15 XI Component of Vorticity and In-plane Velocity Vectors . . .	27	27
16 Behavior of U-Component for $X = 10^6$, Vortex Center at $Z = 0.40$.	28	28
17 Effect of Initial Values on Iteration	29	29
18 Flow Diagram for Wing Vortex Viscous/Potential Flow Interaction Models	32	32
19 Viscous Box System for 65° Delta Wing	33	33
20 Vortex Core Location for Flat Delta Wings	37	37
21 Vortex Core Location for Flat Delta Wings (Effect of a) . . .	38	38
22 Delta Wing Leading Edge Vortex Strength Distribution	39	39

<u>Figure</u>		<u>Page</u>
23	Vortex Strength Input for 65° Delta Wing	41
24	Wing with Strakes and Free Vortices	42
25	Delta Wing Vortex Lattice Arrangements	44
26	Discrete Leading Edge Vortex System	44
27	Velocities at Top Edge of Box 2 Face	46
28	Velocities from Vortex Lattice at Side Edge of Box 2 Face	46
29	Distributed Leading Edge Vortex System	47
30	Box Interface Interpolation	49
31	Procedure for Advancing the Viscous Solution	51
32	Effect of Changing Leading Edge Radius	52
33	Section Showing First and Second Order Boundary Layer Domains	54
34	Isovors for Aft Face of Box 1	57
35	Velocities on Line Normal to Wing L.E., $\alpha = 22^\circ$	59
36	Downstream Box 1 Contours and Velocities	61
37	Downstream Box 2 Contours and Velocities	62
38	Downstream Box 3 Contours and Velocities	63
39	Downstream Box 2 Contours and Velocities With Leading Edge Vorticity Shifted Vertically	66
40	Proposed Curvilinear Mesh	68
41	Pressure Distribution at Wall of Box 1	69
42	Laser Velocimeter Optics and Delta Wing Mounted In Induction Wind Tunnel	71
43	Experimental Edge Velocities at Box 2	74

1. INTRODUCTION

The favorable lifting effects of leading edge vortices on delta wings have been under investigation for many years. More recently, other types of favorably interfering vortices have been noted. These consist of streamwise vortices formed from leading edge "strakes", outboard leading edge extensions ("snags") as on the F-4 (aircraft) and trailing vortices from canard configurations. Now that interfering vortices are recognized aids, as well as detriments, to lift and stability augmentation, considerable emphasis is being placed on gaining knowledge concerning their formation and stability.

There have been many attempts to model the flow for delta wings with leading edge vortices. Matoi¹ has provided a good survey of many of these attempts. The efforts of most have been limited to potential flow models, assuming rotational elements for viscous effects such as the leading edge feeding sheet. The basic assumption of slender-body, conical flow have been followed by most investigators such as Mangler and Smith². Results of these early investigators have laid a good foundation for further research, but they are not successful in obtaining forces and moments over a general range of configurations. Polhamus³, with the leading edge suction analogy, has good success in predicting vortex lift. His method does not describe the pressures or flow mechanism. Good results were obtained most recently by Weber, et al.⁴ and Rao and Nathman⁵, where the trailing edge conditions of delta wings are included in the boundary conditions. Kandil⁶ has also provided a good potential flow model and convergence criteria. The latter have limits that restrain their application to certain configurations as well as raise doubt concerning their accuracy. These limits are given below.

- (1) Thin wings only are considered.
- (2) Starting conditions at leading edge must be assumed.
- (3) The viscous condition of no slip at the wing surface in the area of the free vortex is not satisfied and this can affect final vortex position and strength.

(4) No secondary vortex system is included.

(5) Vortex burst cannot be predicted.

Tools developed at the Lockheed-Georgia Company have the potential for removing all of the above limitations. The last three above are viscous problems. To solve these, Lockheed has been under contract with the Office of Naval Research for approximately two years to develop the "Viscous Box" solution. References 7 and 8 discuss previous efforts and the current efforts are published in this report. The "Viscous Box" is now a working tool. The original efforts of the viscous box development were directed to a theoretical investigation of spanwise blowing. This concept controls the leading edge vortex on straight as well as swept wings; therefore, much of the original analysis of References 7 and 8 contains spanwise blowing with straight wings. This allowed the use of a Green's function integral to supply some of the boundary conditions and the flow-field velocities. This tool has been retained to make various parametric investigations presented in this report. Application of the viscous box method to delta and other highly swept configurations forces the use of an elliptic potential flow solution to obtain boundary conditions. This report discusses the integration of the viscous box and a vortex lattice method as applied to a thin delta wing. Thick wings will be treated in a subsequent report.

2. THE VISCOUS MODEL

2.1 Further Developments of the Viscous Model

One of the major concerns with the numerical model for viscous flow, as developed in Reference 8, has been the loss of accuracy associated with the integration method. The governing equation is that of vorticity transport,

$$\bar{V} \cdot \text{grad} \bar{\omega} = \bar{\omega} \cdot \text{grad} \bar{V} + v \nabla^2 \bar{\omega} \quad (1)$$

where $\bar{\omega}$ is the vorticity vector and is regarded as the primary dependent variable, with \bar{V} determined retrospectively from

$$\nabla^2 \bar{V} = - \text{curl} \bar{\omega}. \quad (2)$$

In order to maintain convective stability in the numerical integration scheme, it was necessary from the outset to use locally upwind differencing for the first derivative of $\bar{\omega}$ in Equation (1). This resulted in first-order accuracy for integration in the cross-flow plane. Such accuracy is acceptable in the streaming direction, since the theory neglects second streamwise derivatives. For the cross-flow plane, however, this approximation can lead to significant errors even for moderate Reynolds numbers. In fact, the error, which is proportional to the product of mesh width and local velocity, results in a term additive to second derivatives and thus is often called "artificial viscosity." In order to upgrade accuracy in the cross-flow plane, first derivatives of vorticity with respect to y and z were formulated as second-order accurate upwind differences, requiring the use of two points upwind of the current point. The form of equation (1) upon expansion is,

$$F_x = AF + BF_z + CF_y + DF_{zz} + DF_{yy} \quad (3)$$

where $F = (\xi, n, \zeta)$, the vorticity vector, and A through D are 3×3 matrices involving the velocities and their gradients. Thus, the first y -derivative of the vector F is given by

$$F_{y_{m,n}} = \frac{1}{2\Delta y} (3 F_{m,n} - 4 F_{m-1,n} + F_{m-2,n}), \quad V > 0 \quad (4)$$

$$= \frac{1}{2\Delta y} (3 F_{m,n} - 4 F_{m+1,n} + F_{m+2,n}), \quad V < 0$$

and the z-derivative is

$$F_{z_{m,n}} = \frac{1}{2\Delta z} (3 F_{m,n} - 4 F_{m,n+1} + F_{m,n+2}), \quad W > 0 \quad (5)$$

$$= \frac{1}{2\Delta z} (3 F_{m,n} - 4 F_{m,n+1} + F_{m,n+2}), \quad W < 0$$

The basic integration molecule in use in the present integration scheme is depicted by the solid lines in Figure 1. This molecule results in a tri-diagonal matrix when forming the implicit solution at each cross-flow plane. Addition of another upwind point results, in general, in a pent-diagonal matrix for which the inversion time is greatly increased. To avoid this penalty, it was observed that since the basic method is a fully nonlinear Alternating Direction Implicit (ADI) scheme, the resulting solution (assuming a convergent iteration) should be a valid one if values from the previous iteration were used for the second upwind points (i.e. at $m \pm 2, n \pm 2$). These are represented by the dashed lines in Figure 1 and complete the augmented molecule for second-order accuracy. This approach provides second-order accuracy with the minimum penalty in computing time.

The effect of more accurate integration can be seen in relative terms by comparing results for a typical flow condition. Figures 2 and 3 present a comparison of the ξ -component of vorticity and the W -component of velocity, respectively, as obtained by the two methods. The flow condition is, as usual, that of a vortex over a plate with cross-flow. The vortex is located between $z = .4$ and $z = .6$ and centered at a height y of roughly .4. The effect of increased flow reversal is reflected in both figures. This is to be expected as a result of removing artificial viscosity. Some estimates of accuracy will be discussed in a later section.

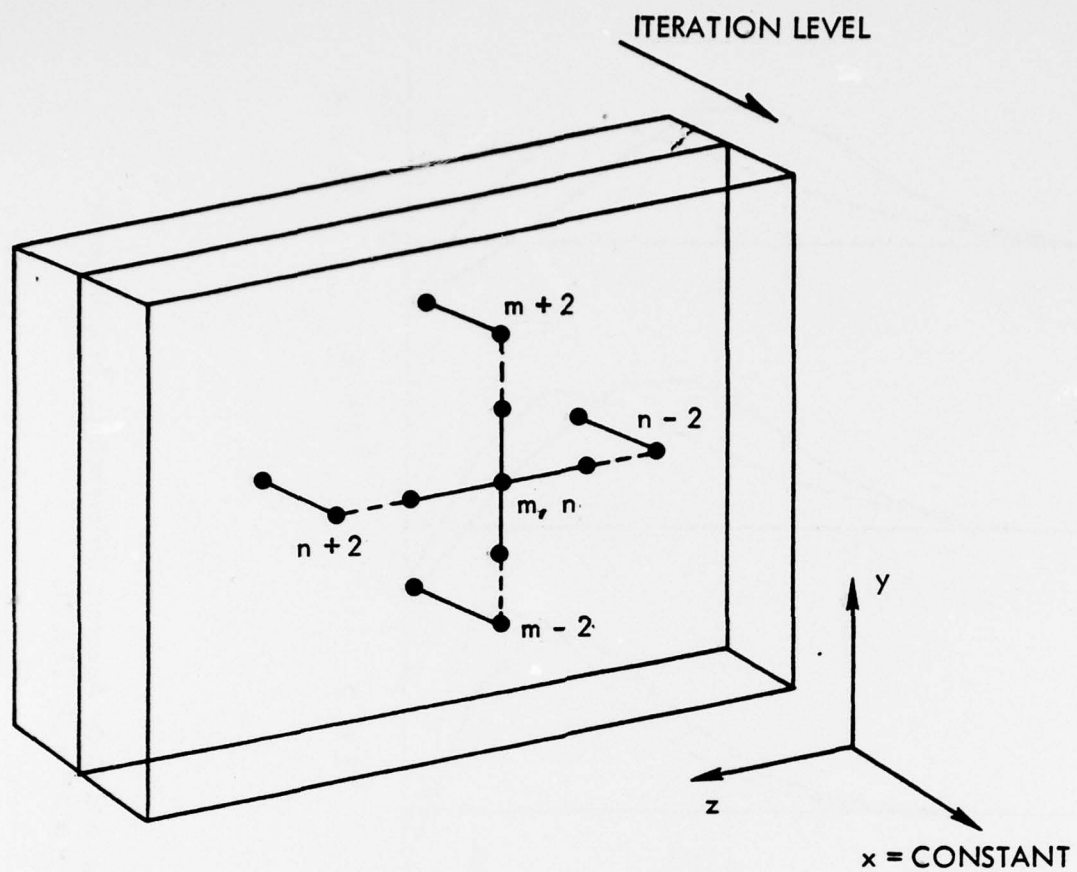


Figure 1 . Augmented Numerical Molecule

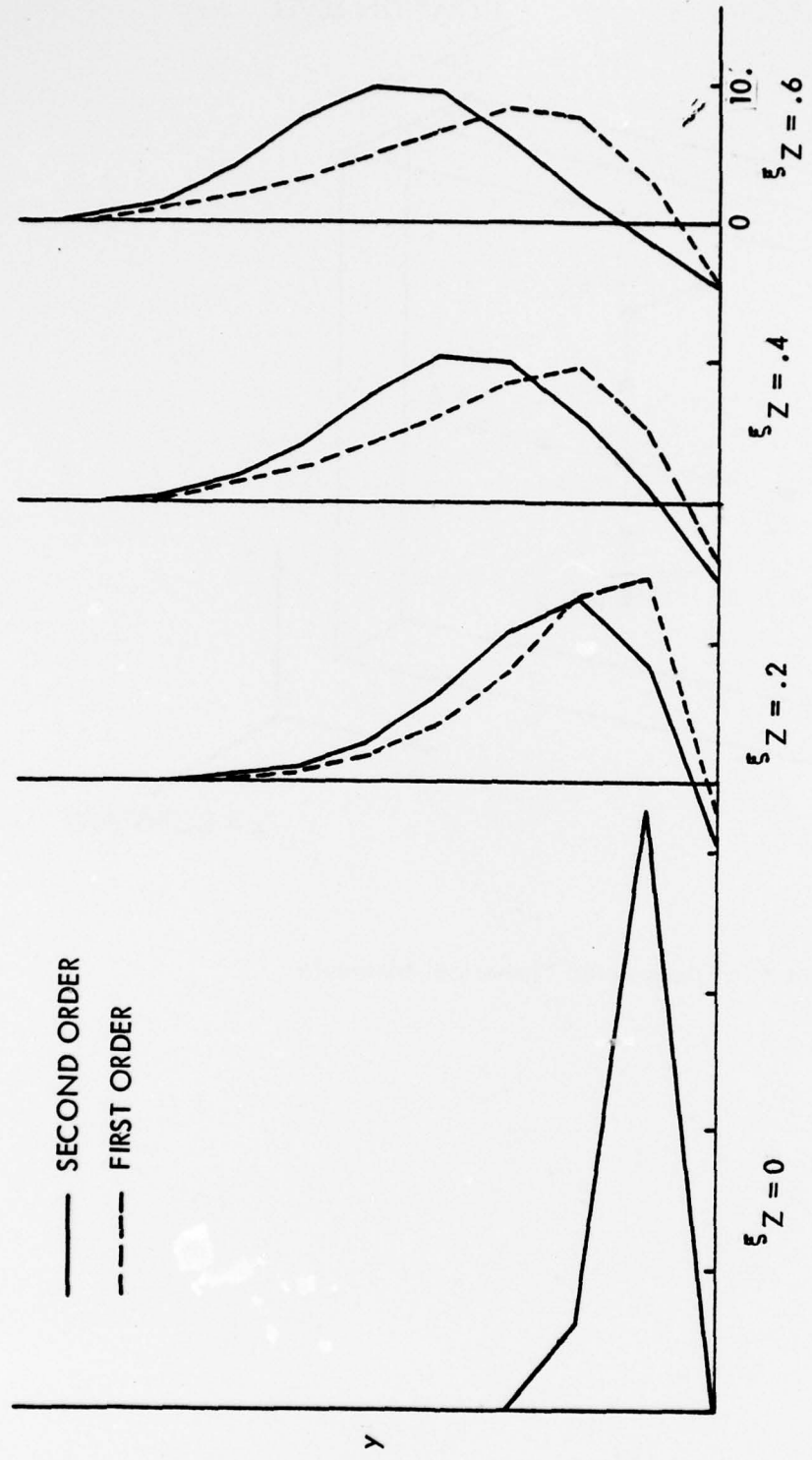


Figure 2 Comparison of First and Second Order Accurate Differencing. ξ - Component of Vorticity at $X = 3.$, $\Delta Y = \Delta Z = .1$, 11×21 .

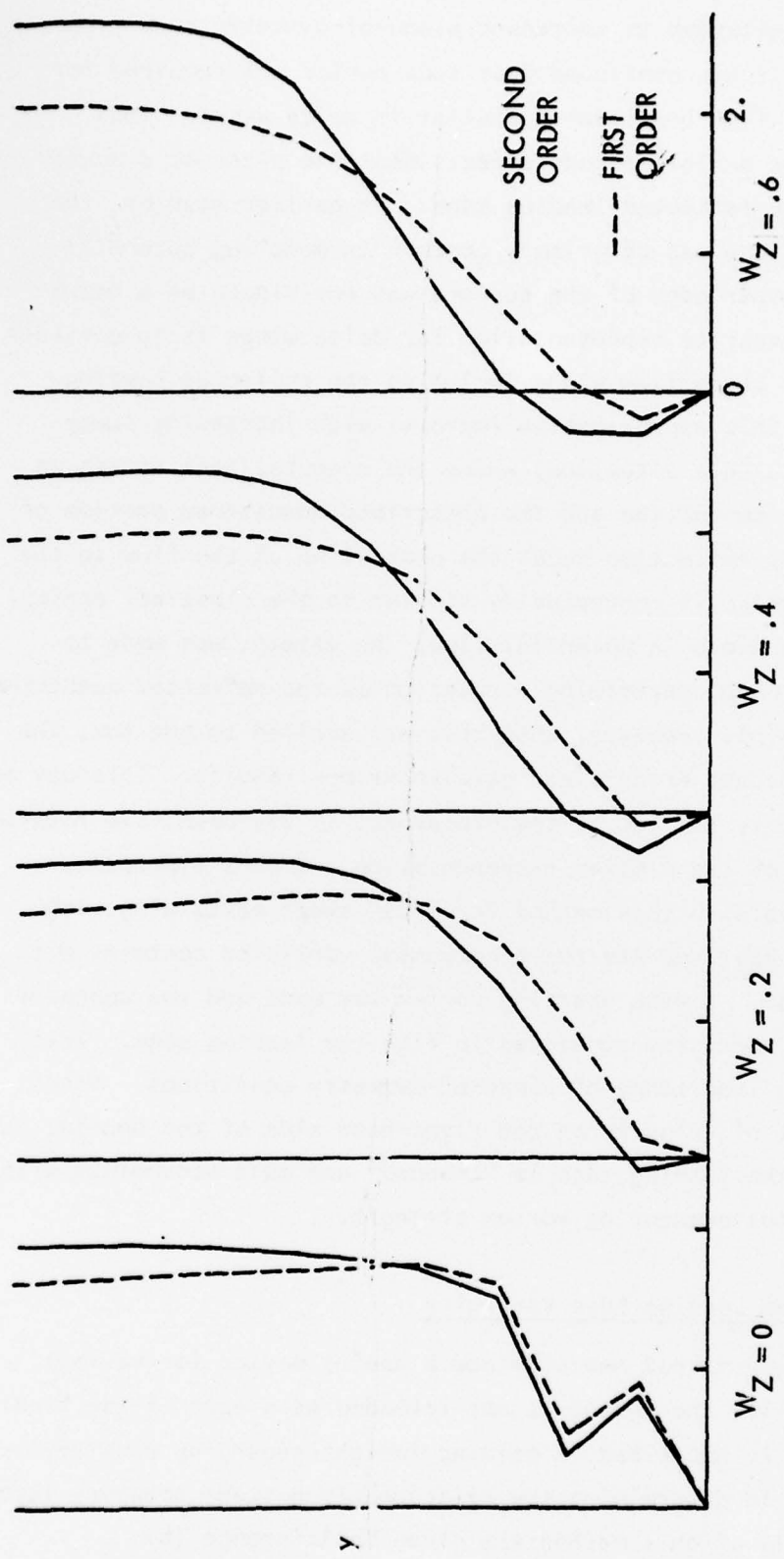
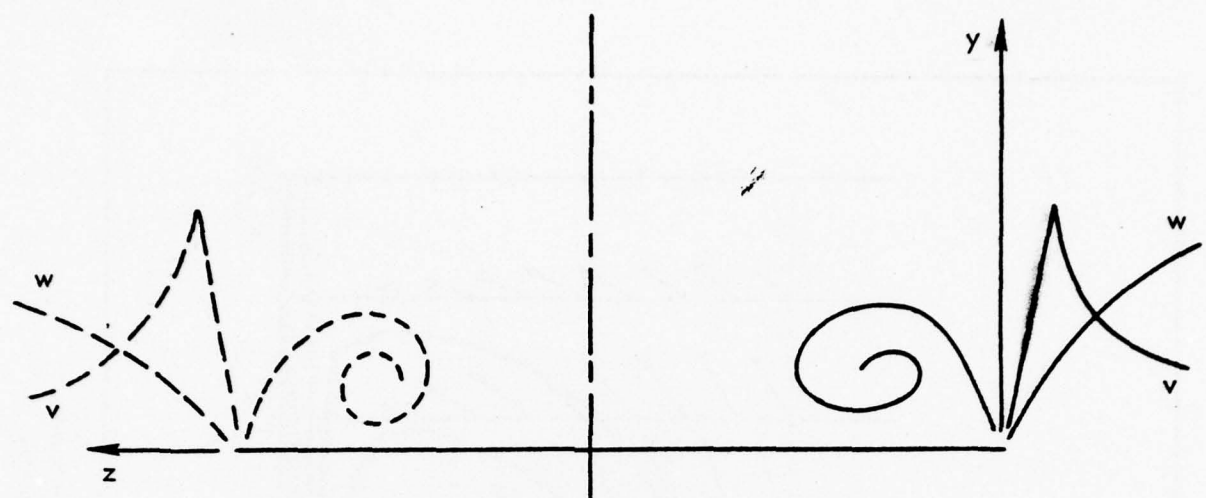


Figure 3 Comparison of First and Second Order Accurate Differencing. W Velocity Component at $X = 3, \Delta Y = \Delta Z = .1, 11 \times 21$.

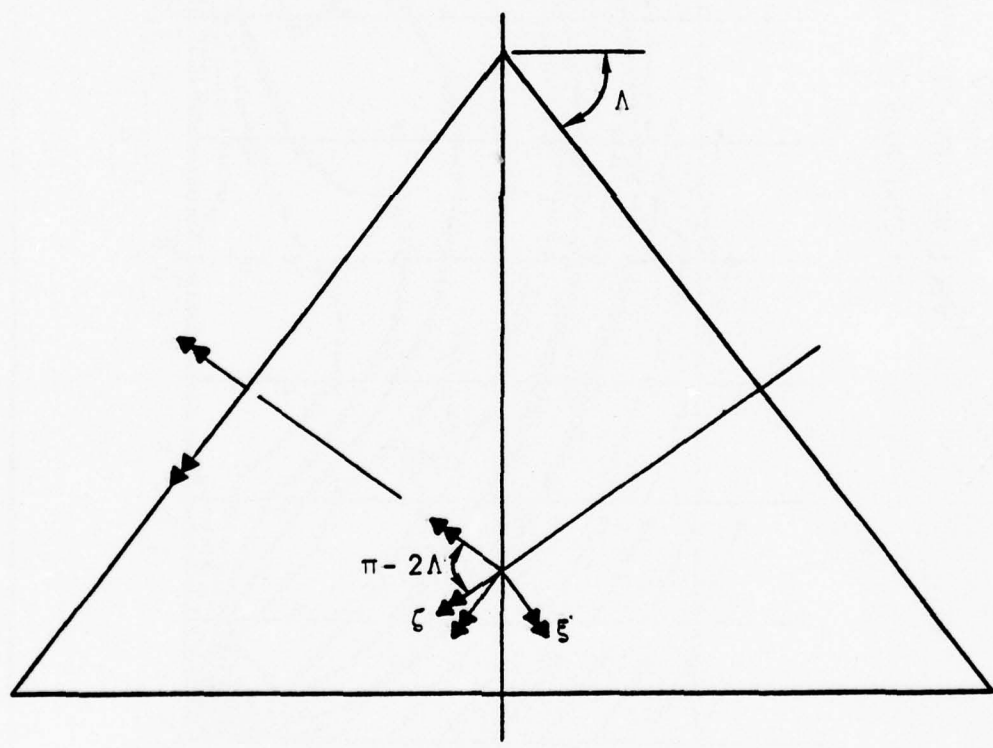
The Green's function method for approximating the potential flow field (Reference 8) has been extended to represent plane-of-symmetry conditions in the cross-flow plane. It was concluded that some device was required for approximating potential flow conditions peculiar to delta wings. Thus, highly swept delta wings exhibit strong effects near the plane of symmetry due to the vortex on the reflected leading edge. In earlier studies, the leading edge of the surface was of primary concern in modeling potential flow effects, and the other edge of the surface was envisioned as a "downstream" edge. A more accurate representation for delta wings is to consider the y-z plane to be the cross-flow plane including the reflected leading edge. The accuracy of this approximation improves with increasing sweep angle. Figure 4 depicts this situation, where the computational domain is now to the right of the centerline and the prescribed downstream portion of the flow field is just a reflection about the centerline of the flow to the right. This representation is conceptually similar to the classical conical flow treatment of delta wings in potential flow. An attempt was made to improve the approximation by performing a rotation of the reflected quantities as depicted in Figure 4(b). However, when this was applied to the box, the numerical integration became erratic and gave anomalous results. This may be related to the ellipticity implied by the procedure; in any case, the rotation was abandoned in favor of the simpler representation. Figure 5 presents typical results obtained with this method for a 65° swept delta wing with $\xi_{l.e.} = 43$ and $\alpha = 22^\circ$. Depicted are the ξ -component vorticity contours with V-W vectors superimposed. A weak starting vortex was used and the contours shown are augmented by vorticity convected in from the leading edge. This result demonstrates the importance of plane-of-symmetry conditions. Since there is no w-component of velocity on the right-hand side of the domain, the vorticity fed in from the leading edge is "trapped" and must accumulate with distance downstream, thus augmenting vortex strength.

2.2 Significance of the Leading Edge Vorticity

The Green's function method has provided a useful device for various parametric studies. While the method is not intended as a part of the final computational package, it has aided in gaining insight regarding sensitivity to edge conditions and in determining the relationship between boundary layer and vortex. The details of this method are given in Reference (8).



(a).



(b)

Figure 4 . Simulation of Delta Wing for Green's Function Application

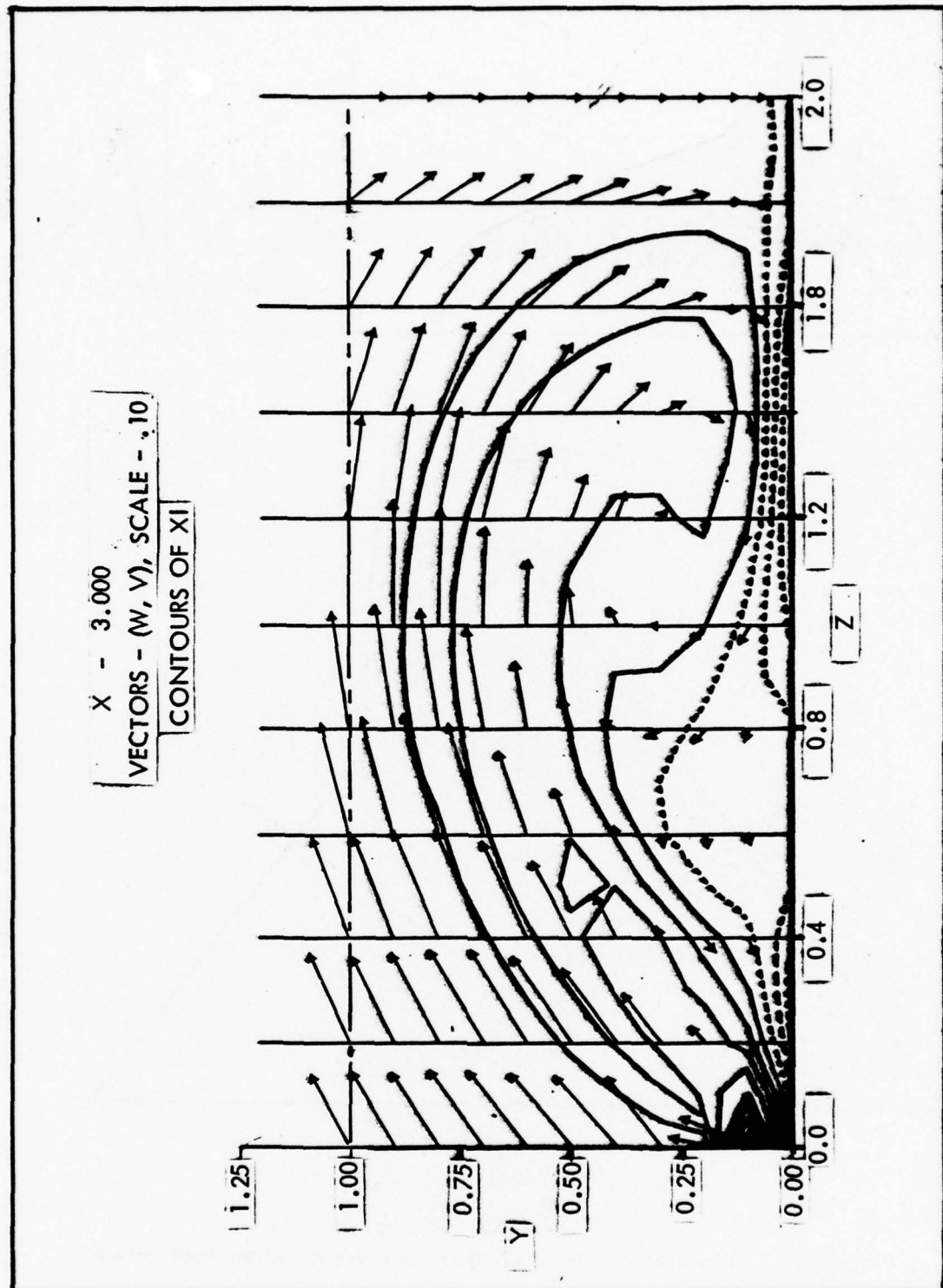


Figure 5 • Velocity Vectors and Contours of ξ Component of Vorticity with Simulated Plane of Symmetry

Some computations were performed to demonstrate that, using the Green's function method, the necessary leading edge vorticity could be obtained as a part of the boundary value solution. It appears, however, that this is not appropriate. The problem of immediate concern is that of a sharp leading edge surface. The discussion following should, however, be valid whether the leading edge is sharp or rounded, as long as separation is very near the leading edge. Examination of experimental results for the V -component very near the leading edge has shown that the original assumption used for V in the Green's function was in fact quite accurate. The situation is depicted in Figure 6. The boundary layer detachment point is shown at the forward most point of the leading edge; and in this case, the boundary layer profile is coincident in direction with V as measured from the coordinate system of the viscous box. However, within the boundary layer thickness, δ , the actual profile shape can be expected to differ from the linear one assumed for V . But the important thing is to require that the vorticity contained in the boundary layer, and thus transported into the viscous box, be represented on the box boundary. The obvious suggestion then, is to adjust the thickness δ assumed for the V -component so that the vorticity computed from the straight line segment of V is equal to the average value in the actual boundary layer. This reduces the behavior of V near the leading edge, and its associated boundary vorticity, to the specification of a single parameter: δ .

As noted before, the apparent value of vorticity appropriate to the central test condition of the 65° swept model is approximately 43. With the computer program modified to automatically fix both V and leading edge boundary vorticity upon specification of δ , a series of runs were made varying δ or $\xi_{1.e.}$ to create a range of flow conditions as depicted in Figure 7.

(Note: $\xi_{1.e.} \approx \partial V / \partial z$ across the boundary layer ahead of the box.) The values of $\xi_{1.e.}$ were 20, 30, 43, 50, and 60. For each, the characteristics of the flow are computed at the inlet face of the viscous box and at $X=1$. To illustrate the effect of this input, ξ -vorticity contours for $X=1$ are presented for each of the chosen $\xi_{1.e.}$ values in Figure 7.

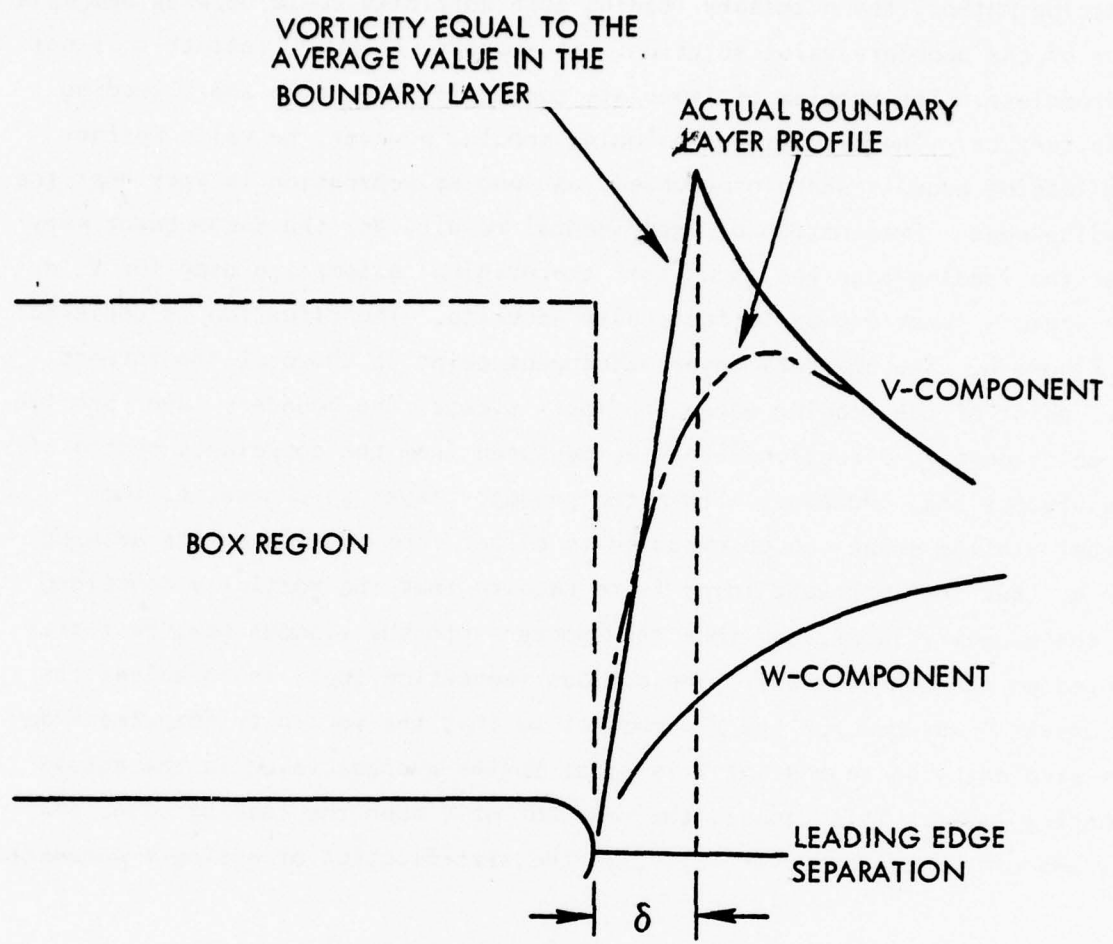


Figure 6 . Leading Edge Conditions

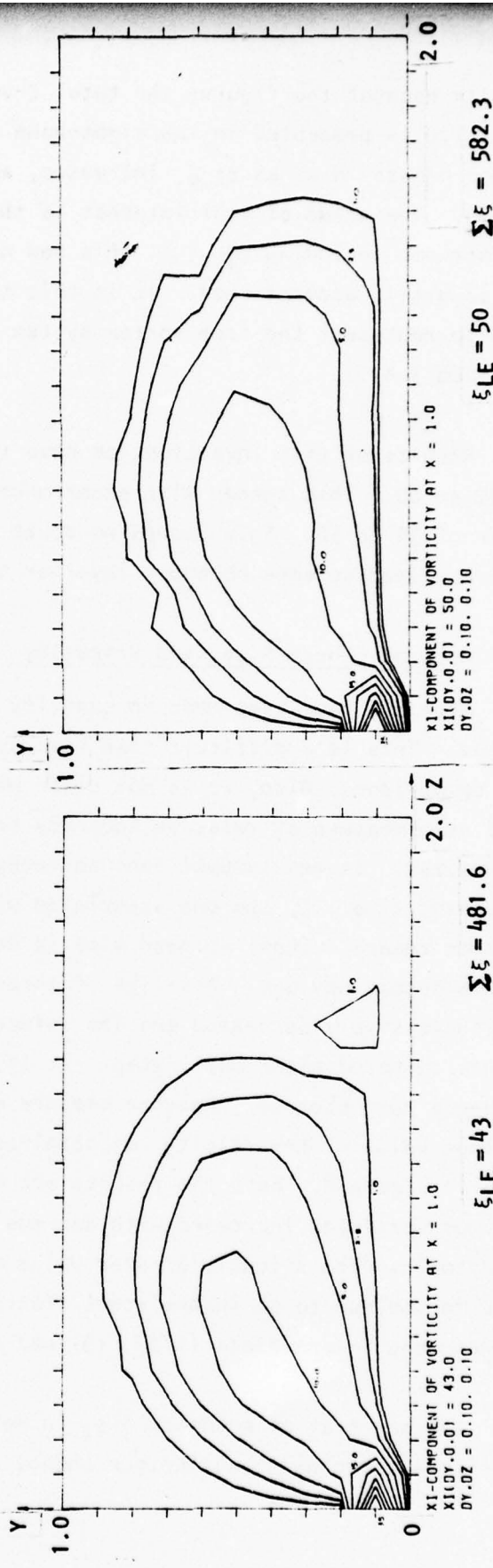
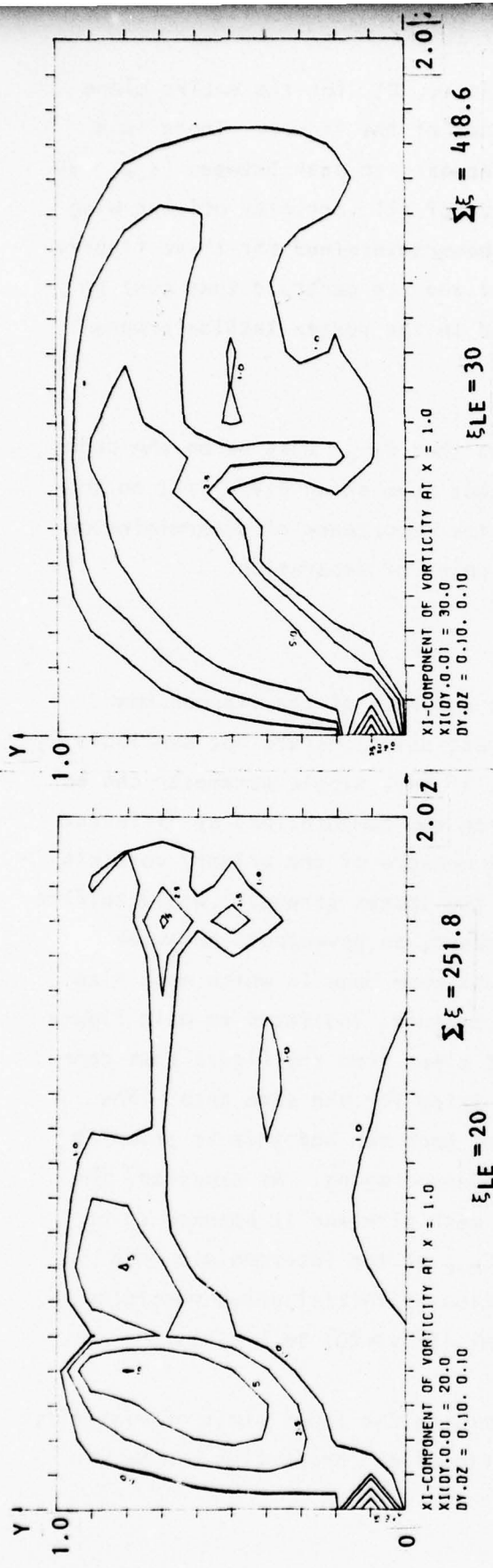


Figure 7 Effect of Leading Edge Vorticity on Vorticity Contours

In each of the figures the total ξ -vorticity, $\Sigma\xi$, for the entire plane at $X=1.0$ is presented in the right-hand corner of the figure. There is a strong growth in $\Sigma\xi$ as $\xi_{1.e.}$ increases, and appears to peak between $\xi_{1.e.} = 50$ and 60. The value of real interest is the sum of all vorticity off the wing surface not including $\xi_{1.e.}$. This has not been determined for these figures but is easily accomplished. It is this total and its centroid that must be used to represent the free vortex system used in the vortex lattice program (Section 3.4).

Results of this investigation have shown that $\xi_{1.e.}$ must be on the order of 40 to 60. This agrees with experiments that have shown $\partial(V/W_\infty)/\partial Z$ on the order of 35 to 50. This leaves no doubt of the importance of determining an accurate leading edge boundary layer at the point of separation.

2.3 Accuracy, Mesh Size, and Viscosity

Attempts have been made to quantify the accuracy of the viscous box method. This is a difficult task because exact solutions are not available for comparison. Also, it is not clear what, if any, single parameter can be used as a measure of relative accuracy between two computations at different mesh sizes. It was thought that an integral measure of the primary vorticity component (i.e., ξ , the one associated with the vortex strength) would suffice in this regard. Thus, as mesh size is decreased, an asymptotic behavior should become obvious. A series of three runs were made in which mesh size was successively decreased and the integral measure, indicated as Ω in Figure 8, was computed after one x-step. It is not clear from the figure that convergence has occurred. Another measure was tried for the same data: The maximum value of ξ -vorticity was obtained for each run and this is shown as ξ_{max} in Figure 8. Here the results are more encouraging. As expected, the maximum vorticity increased with decreasing mesh size and it appears to be asymptotic. The slightly greater value of ξ_{max} at the intermediate mesh size may be due to an inconsistent distribution of initial value vorticity between the intermediate ($1/\Delta y = 15$) and final ($1/\Delta y = 20$) mesh sizes.

Another test of accuracy lies in determining the lower limit of viscosity coefficient for which no further change in flow field properties can be

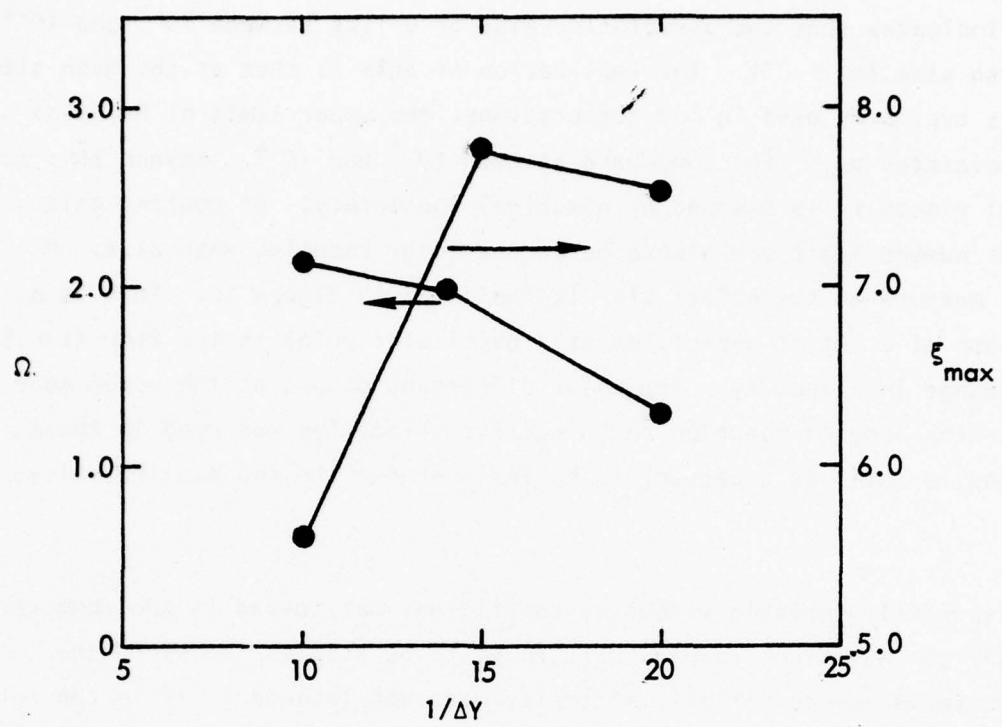


Figure 8 Effect of Mesh Size on $\Omega = \iint \xi dy dz$, and ξ_{\max}

observed. A series of three runs were made varying only the viscosity coefficient. Values of $\nu = 10^{-2}$, 10^{-3} , and 10^{-4} were used. Again, the quantity, previously referred to, was computed and this is shown in Figure 9. This figure indicates that the asymptotic value of ν lies between 10^{-3} and 10^{-4} when mesh size is 11×21 . The implication of this is that at the mesh size which is typically used in our computations, the upper limit of Reynolds number dictated by ν lies somewhere between 10^{-3} and 10^{-4} . Beyond this point the real viscosity is swamped by numerical inaccuracy. Of course, this Reynolds number limit can always be increased by reducing mesh size. A further measure of the effect of ν is indicated in Figure 10. This is a comparison of a set of W-profiles at a particular point in the flow ($z = .5$) for a change in viscosity. The major difference occurs at the outer edge of the box (the Green's function technique for velocities was used in these runs) and is seen, as expected, to be less between the two smaller values of ν .

A spatially variable viscosity coefficient was tested in the computer code, and the numerical results were found to be stable. However, the gradient terms due to variable viscosity were not included. If in the future a turbulence model is incorporated in the code, then it will be necessary to add these terms. The present investigation was intended only to demonstrate feasibility, and no use has been made of the variable viscosity feature.

2.4 Effect of Sweep and Flow Angularity at the Leading Edge

Parametric studies were performed to evaluate the effects of sweep and flow angularity on leading edge vortex behavior. The effects of both are very similar; the lower limit of sweep angle for which a vortex can be sustained is somewhat larger than 25° . The flow is definitely unstable at that angle and is probably not stable at considerably higher angles if the calculation is marched far enough outboard. The parametric study was performed using only one x-step.

The effect of flow angularity is a more interesting case and will be discussed in some detail. This effect is best discussed in conjunction with Figure 11. The vorticity feeding the leading edge of the vorticity box is, as has been discussed in the past, associated with the separating boundary

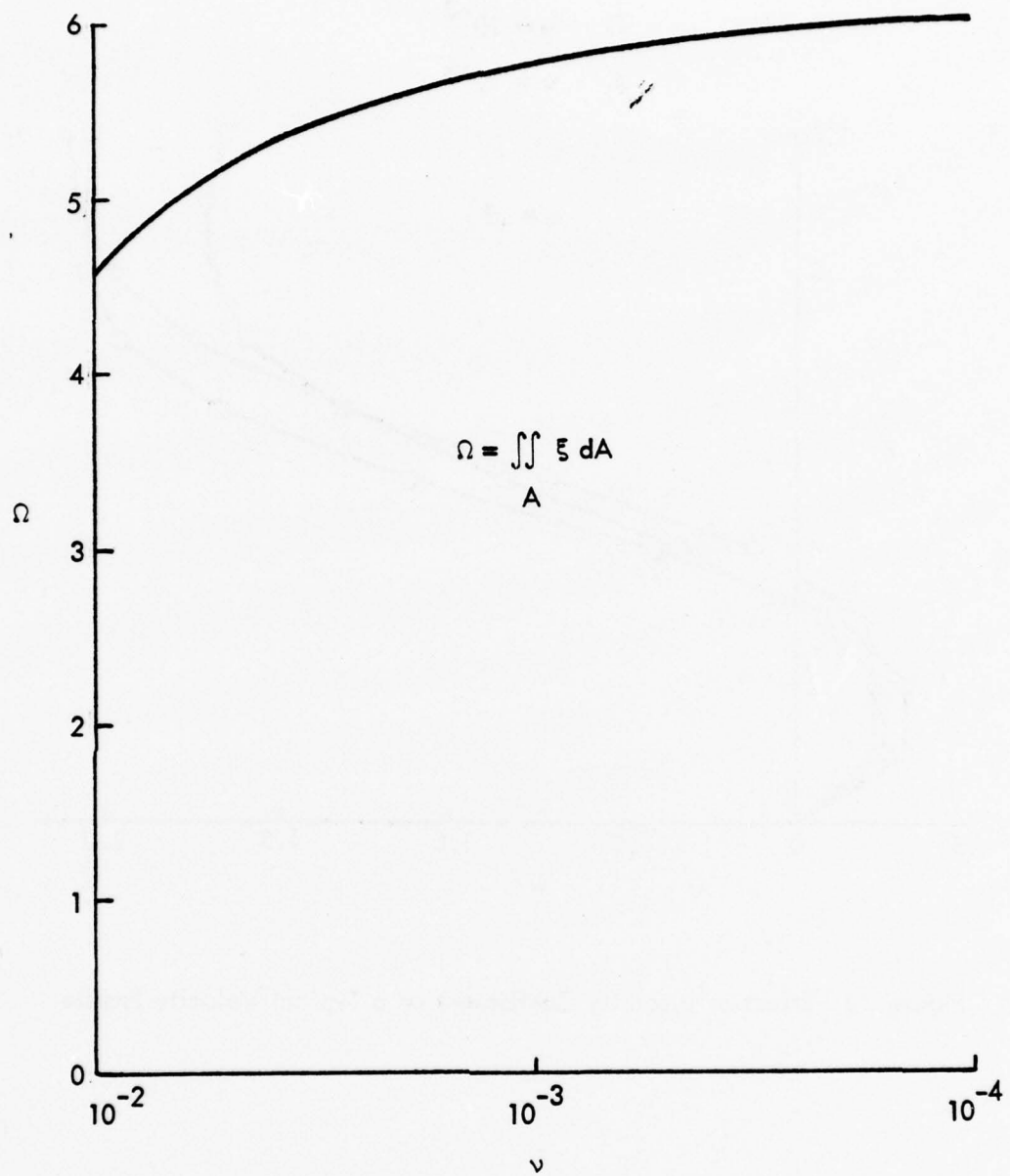


Figure 9 Variation of Ω with ν

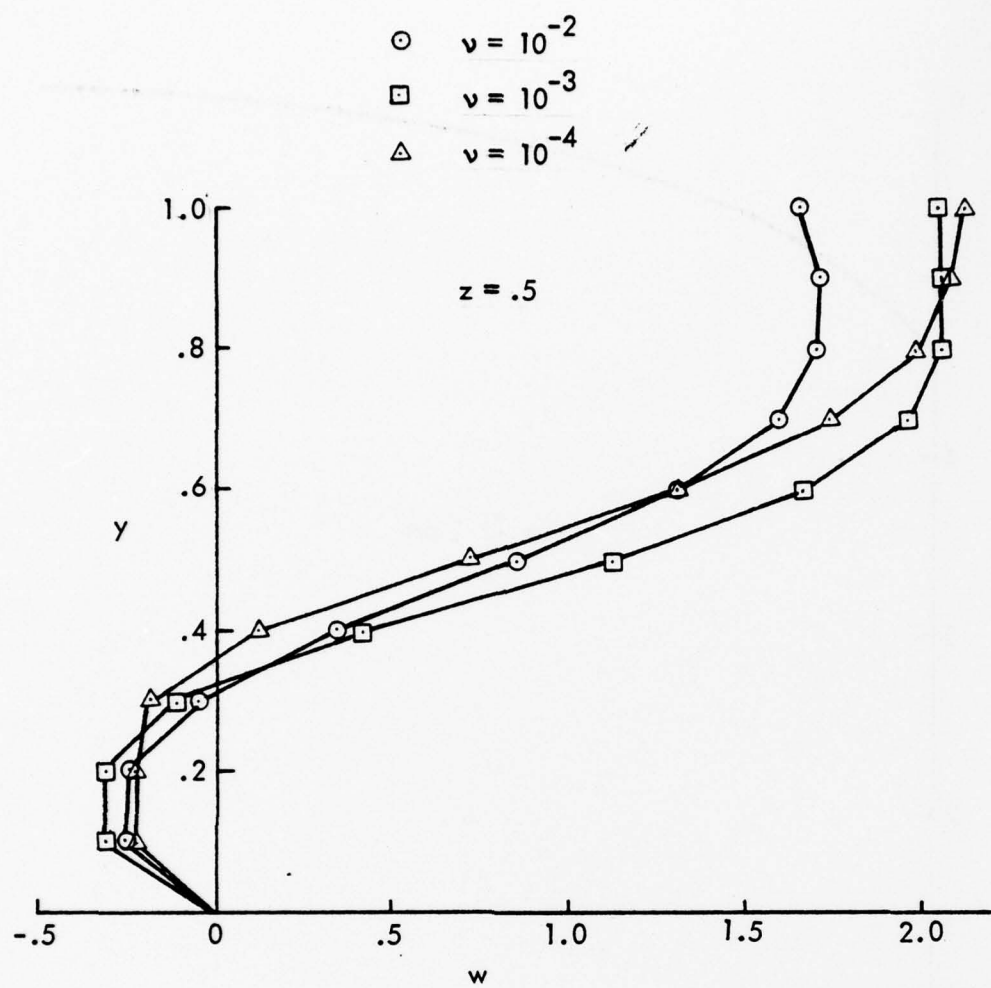


Figure 10 Effect of Viscosity Coefficient on a Typical Velocity Profile

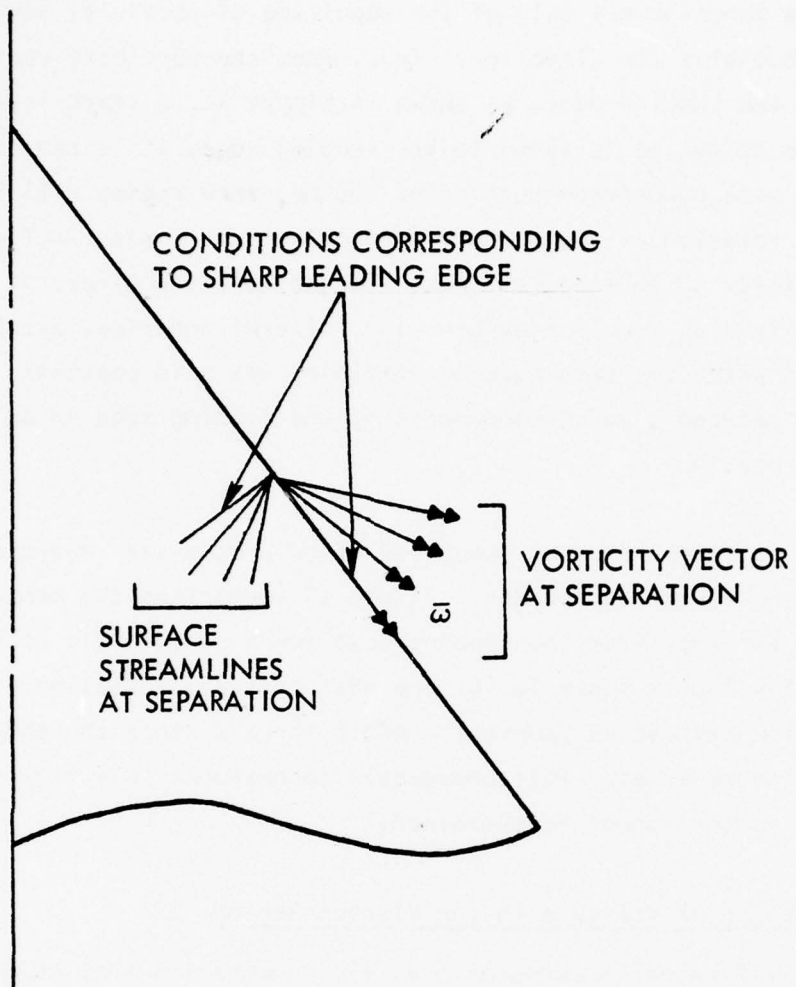


Figure 11 Schematic of Leading Edge Separation as a Function of Leading Edge Shape

region just upstream of the box. The development of this region is very much dependent on leading edge shape, and its effect on vortex development within the box is a function not only of the magnitude of vorticity emanating from the region but also its direction. Thus, when the vorticity vector is parallel to the leading edge, as shown in Figure 11, a sharp leading edge is implied. As thickness is added to the leading edge, it is reasonable to expect that some downstream turning of the boundary region will be reflected through the rotation of the surface streamline. This also implies a rotation of the vorticity which feeds the box. To estimate the effect of such a rotation on leading edge vortex behavior, several numerical experiments were performed in which the magnitude of vorticity was held constant, but was apportioned between ζ and ξ components at the leading edge so as to reflect the vector rotation.

Again, as in the case of sweep, the flow progresses toward unstable conditions as the vector is rotated. Figure 12 summarizes the behavior for a rotation of 40° away from the leading edge for a sweep angle of 65° . The U-component of velocity shown is for the most critical z-station, i.e. where the first flow approaches reversal. After three x-steps the computations diverge due to reversal. This presumably corresponds to a flow condition for which a vortex cannot be sustained.

2.5 Computation of Pressure in the Viscous Region

It is well known in computational fluid mechanics that computing pressure in a viscous flow is very sensitive to numerical differencing errors. The procedure used here is as follows: The momentum equations are

$$\begin{aligned}
 - \text{grad } \frac{p}{\rho} + v \nabla^2 \bar{v} &= \bar{v} \\
 = \text{grad } \left(\frac{v^2}{2} \right) - \bar{v} \times \bar{\omega} & \quad (6)
 \end{aligned}$$

and

$$\nabla^2 \bar{v} = - \text{curl } \bar{\omega} \quad (7)$$

then,

$$\text{grad } \left(\frac{p}{\rho} + \frac{1}{2} v^2 \right) = -v \text{curl } \bar{\omega} + \bar{v} \times \bar{\omega} . \quad (8)$$

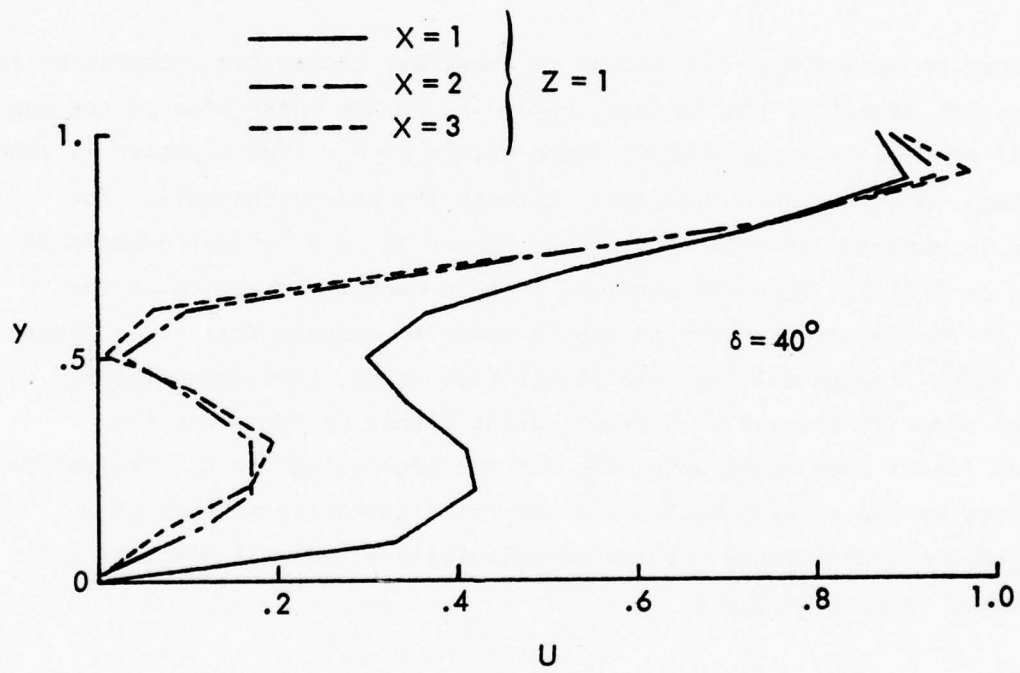
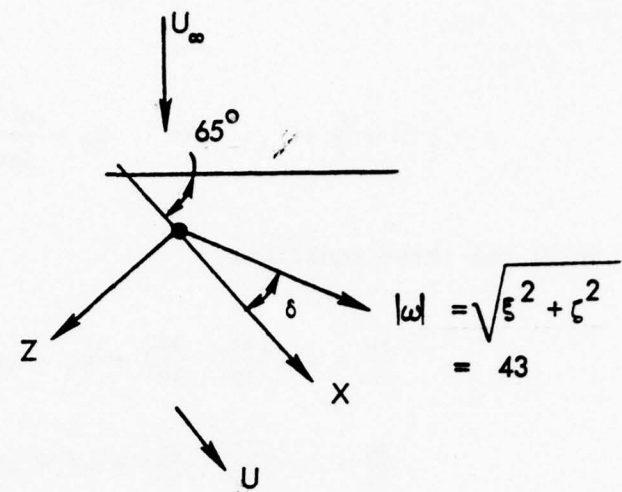


Figure 12 Effect of Angular Position of Leading Edge Vorticity

Let

$$H(x, y, z) = \frac{p}{\rho} + \frac{1}{2} v^2 \quad (9)$$

so that,

$$p = \rho(H - \frac{1}{2} v^2) \quad \text{and} \quad C_p = \frac{p - p_\infty}{\frac{1}{2} \rho v_\infty^2} . \quad (10)$$

Then any one of the three equations,

$$\frac{\partial H}{\partial x} = - v \left(\frac{\partial \xi}{\partial y} - \frac{\partial \eta}{\partial z} \right) + v \xi - w \eta \quad (11)$$

$$\frac{\partial H}{\partial y} = - v \left(\frac{\partial \xi}{\partial z} - \frac{\partial \xi}{\partial x} \right) + w \xi - u \xi \quad (12)$$

$$\frac{\partial H}{\partial z} = - v \left(\frac{\partial \eta}{\partial x} - \frac{\partial \xi}{\partial y} \right) + u \eta - v \xi \quad (13)$$

may be used to obtain C_p . The second of these was chosen for integration in the direction normal to the surface, beginning on the outer edge of the box where, if the box is large enough, there exists $H = H_\infty$. The equation is then integrated, to second-order accuracy, through the box to the wall. The pressure is computed at each mesh point; Figure 13 is a typical example of pressure coefficient contours obtained in this manner. Pressure at the surface is the important quantity and in order to compute this it is necessary to march through all the mesh points from above, thus accumulating numerical error at the wall. However, using either of the other two equations leaves some doubt about the correct edge value for H . Evaluation of accuracy by the present method and several alternative methods is a subject of continuing study. Detailed calculations for wall pressure will be discussed in Section 3.8.3.

2.6 Iteration and Step Length Sensitivity

The major difficulty with the parabolized flow approximation as used in the viscous box is sensitivity to initial conditions. This is expected of parabolic systems when the marching variable is not far removed from its starting value. When this variable becomes large, however, the solution

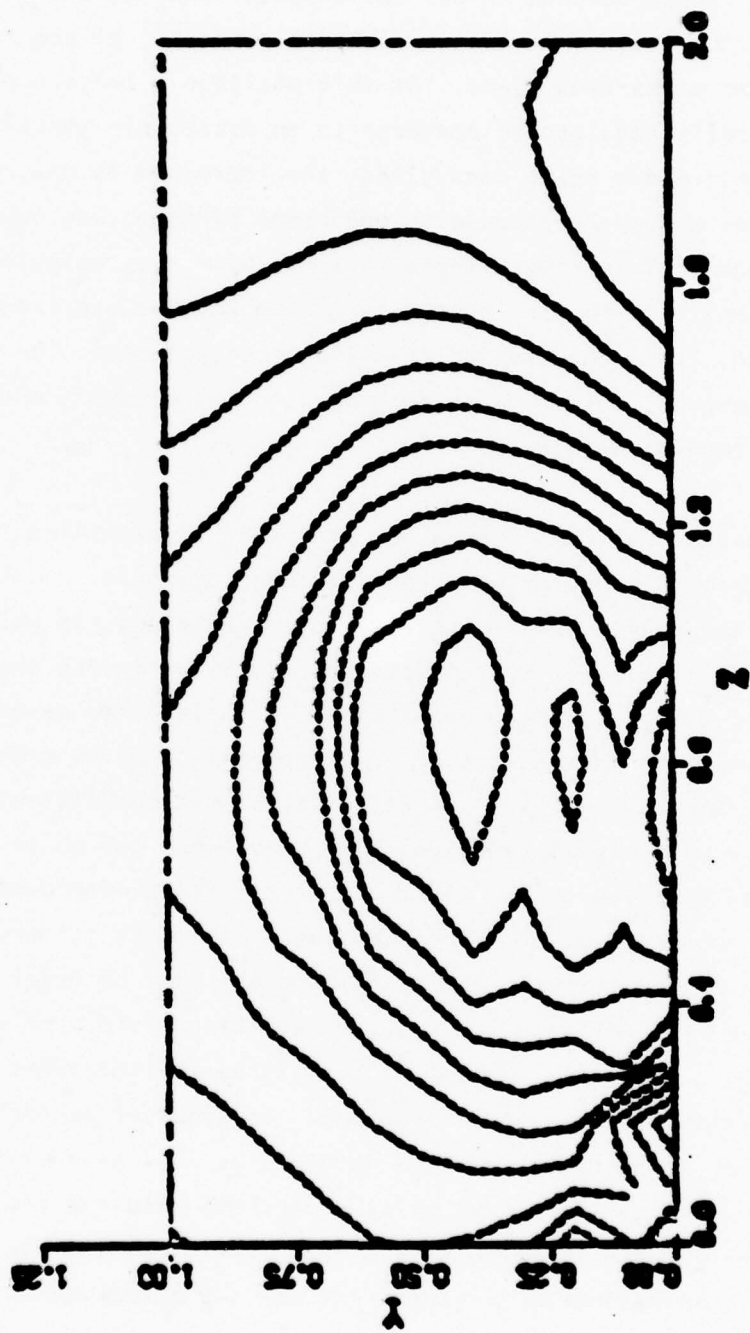


Figure 13 Pressure Coefficient Contours

"forget" the initial conditions and become dominated by the boundary values. If the initial conditions are not physically correct, it becomes very difficult and sometimes impossible to converge the iteration for the first step away from the starting plane. In the present study of leading edge vortex flows, exact starting values for some positions along the leading edge have not been available. The procedure in all the computations has been to make a guess of starting conditions and step a distance generally of the order of box dimensions in the cross-flow plane. At this position a large number of iterations are generally required to converge to an acceptable three-dimensional solution. Under these conditions, the iteration is not convergent when the initial x -step is reduced to one order of magnitude lower than the lateral dimensions. This simply means that the numerical solution procedure is more sensitive to the inaccuracy of the assumed starting values. It is noted, however, that once a valid solution is established, the marching procedure is well behaved, both with respect to stepping distance and to change of boundary conditions with x .

A "distance relaxation" computation was performed to determine if this would produce an improved starting solution. The analogy here is with the time relaxation of the full parabolic Navier-Stokes equations, in which steady flow solutions to the (elliptic) system are obtained by advancing the parabolic solution over a long time. In the present case, a single large x -step can be used to relax the solution independent of x . Since the solution procedure is implicit and fully nonlinear (i.e. no linearization about coefficients at the previous step), only one step is required. The conditions for which this was performed were those applying to the first box on the delta wing demonstration case, discussed in another section. The point here is simply to demonstrate the results of such a computation. The box dimensions were of order unity and a step length $\Delta x = 10^6$ was used. A typical iteration history of vorticity appears in Figure 14. As shown, the solution required 16 iterations to converge and the iteration history is well behaved. In order to perform the computation, a set of boundary values were required as well as initial conditions. The boundary values of velocity were those obtained from vortex lattice calculations for the starting face of the first box, and the leading edge vorticity was that estimated for the first box (as discussed in a later section). The cross-flow velocity vector and ξ -component vorticity fields

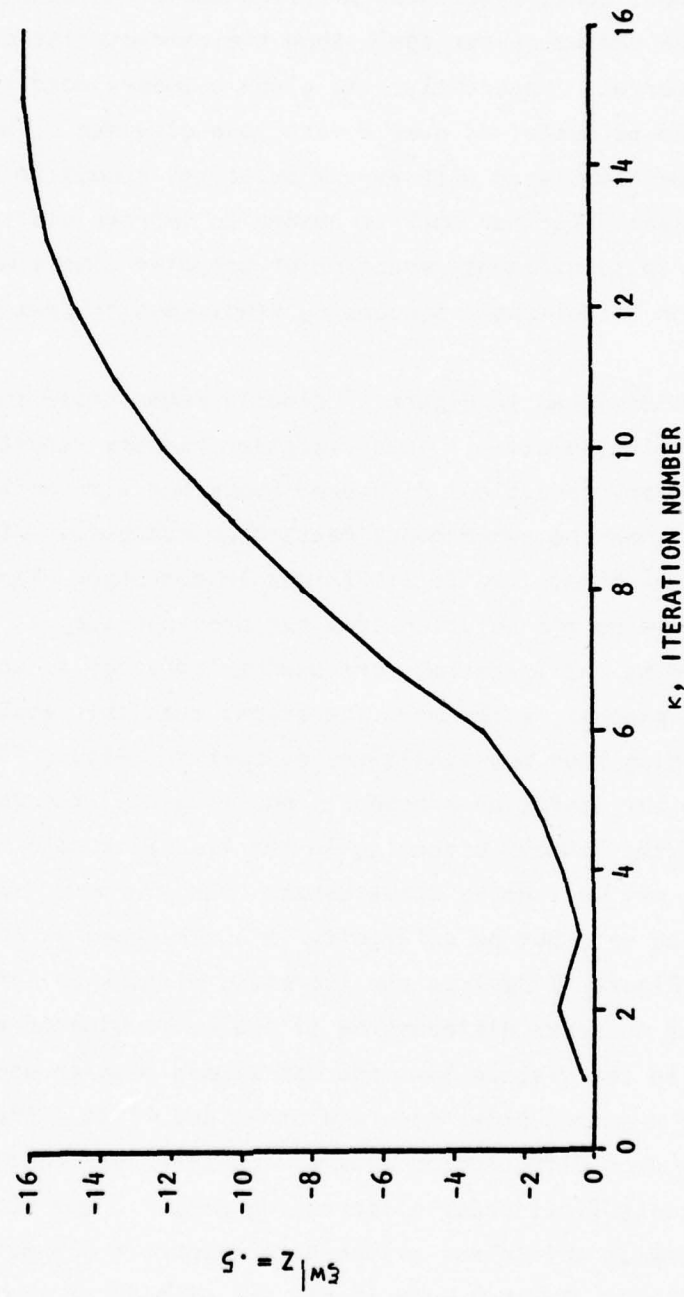


Figure 14 Iteration History of Starting Solution
for X-Step of 10^6

resulting from relaxation with those imposed values are shown in Figure 15. These would appear to represent reasonable initial values for beginning the downstream march. However, the U-component of velocity, as seen from Figure 16 has attempted reversal. Actual reversal is not allowed in the computer code since this leads to a divergent iteration. The profiles at $z = .15$ and $.25$ are representative of the behavior just forward of the apparent vortex center, and without constraint these profiles would indicate reversal. The profiles near the vortex center again show the characteristic axial acceleration under the vortex. Apparently, the given boundary conditions will not allow a vortex to be sustained over a very long distance. The indicated reversal could be associated with vortex bursting, though no axial pressure gradient is present. Further work is needed to improve starting values. This can result in significant reduction of computer time since, with an accurate solution established, succeeding steps require fewer iterations.

The results depicted in Figure 17 clearly demonstrate the advantage of an accurate starting solution. This iteration history resulted for the same initial and boundary conditions discussed above but with an X-step of unity. The solid lines show the convergence pattern on successive steps following the first one, which required 16 iterations to converge. These later steps, which are begun using the solution from the previous step as the initial guess for beginning the iteration, are seen to converge in about three iterations. In general, a few more iterations than this would be expected because of changing boundary conditions at each X. Figure 17 also reveals a difficulty with the iteration procedure resulting when the vorticity is near zero. Although the "shock" occurring in the iteration does not destabilize the process, it may well delay convergence. The source of this behavior has not been isolated yet, but no difficulty is anticipated in correcting it. The dashed line in Figure 17 depicts the iteration history at $X = 1$, resulting from first-order accurate differencing of the wall value of vorticity. The procedure used in the viscous box code has always been to update wall vorticity using a second-order accurate one-sided first difference. It has been noted that such differencing does not conserve vorticity whereas, at least theoretically first-order differencing does. Our numerical experiments do not provide sufficient evidence to support a change to the lower accuracy at present. Further experiments are planned to examine this question.

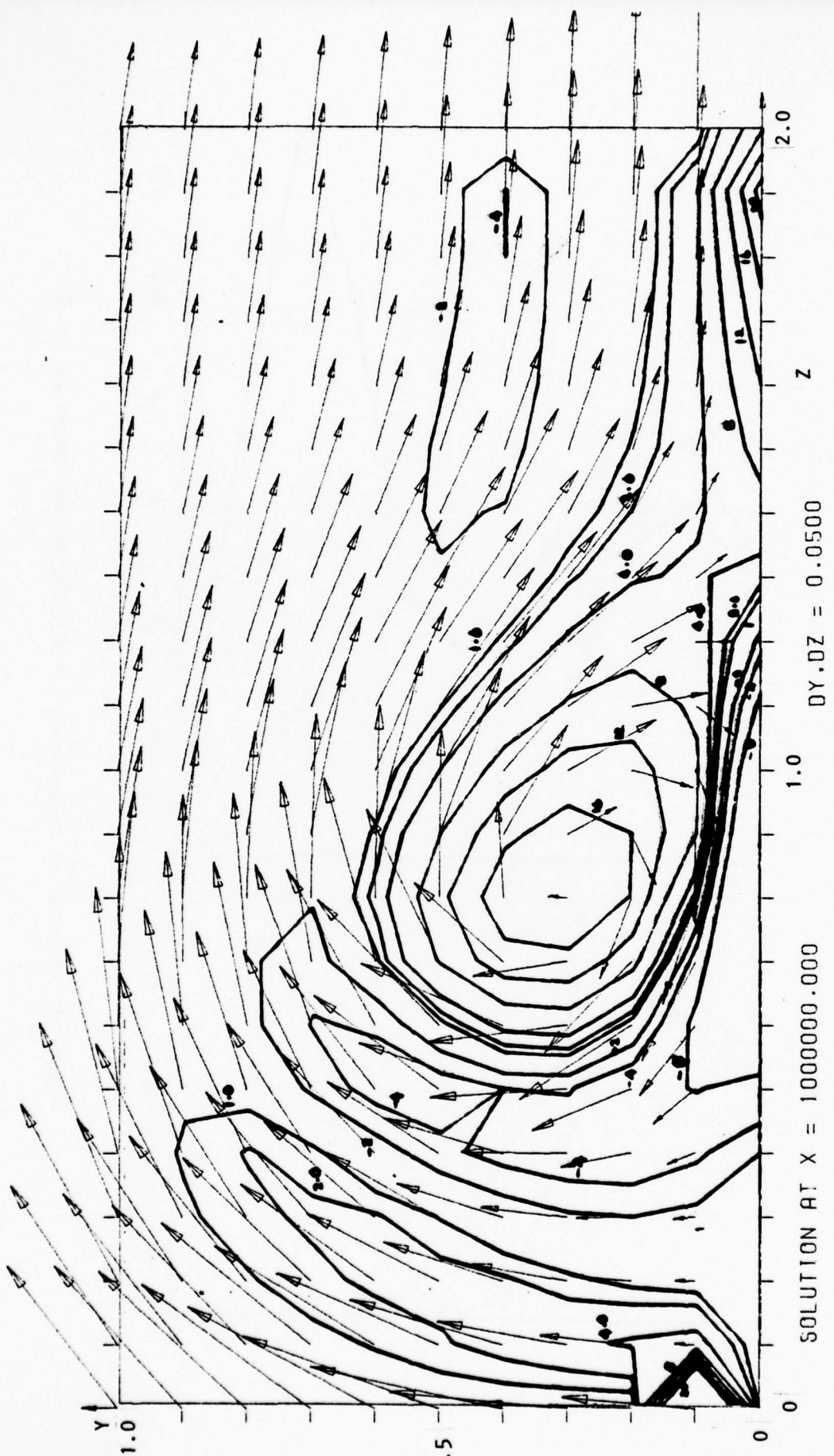


Figure 15 Inplane Velocity Vectors and ξ Component of Vorticity

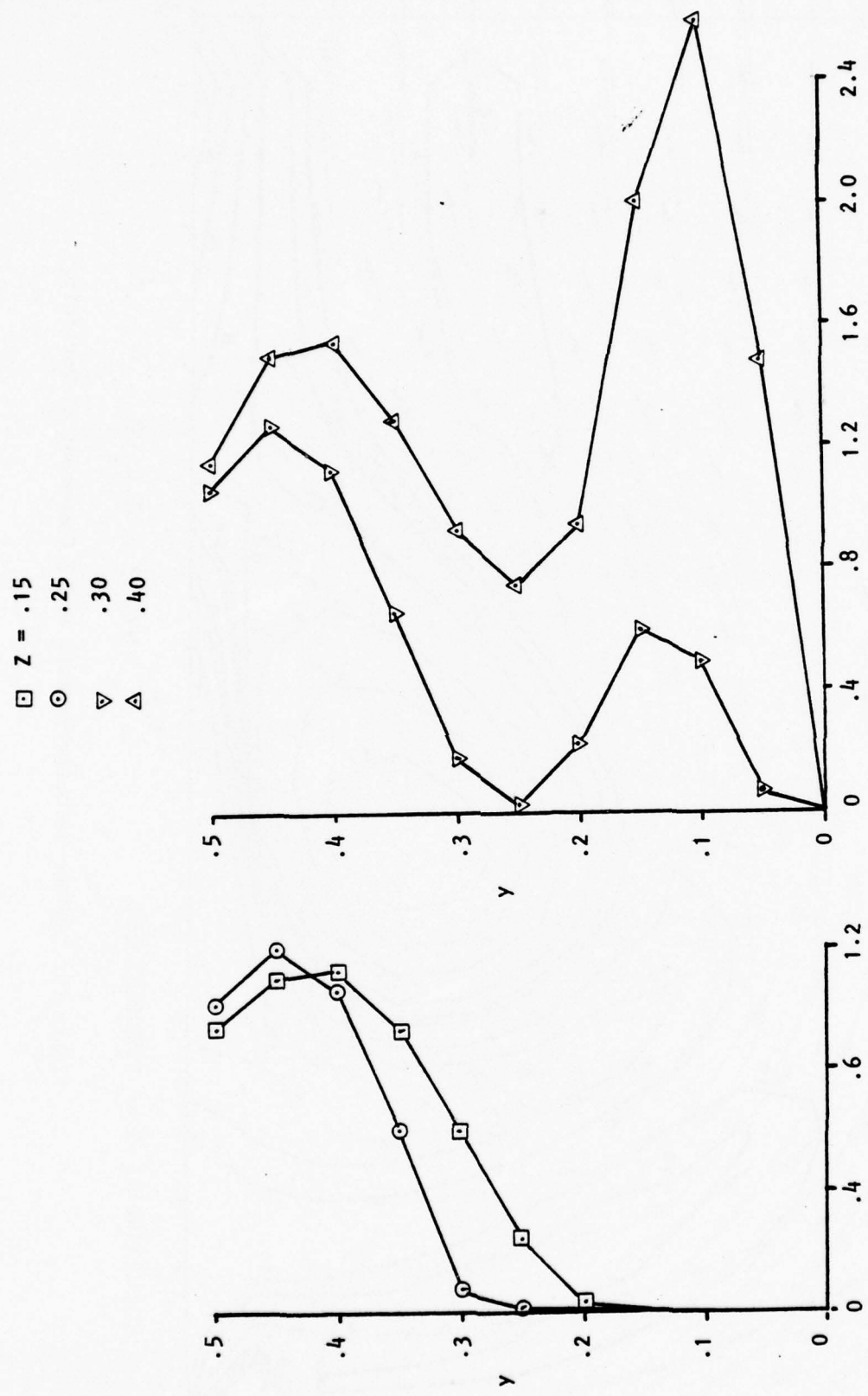


Figure 16 Behavior of U-component for $x = 10^6$, Vortex Center at $z = .40$

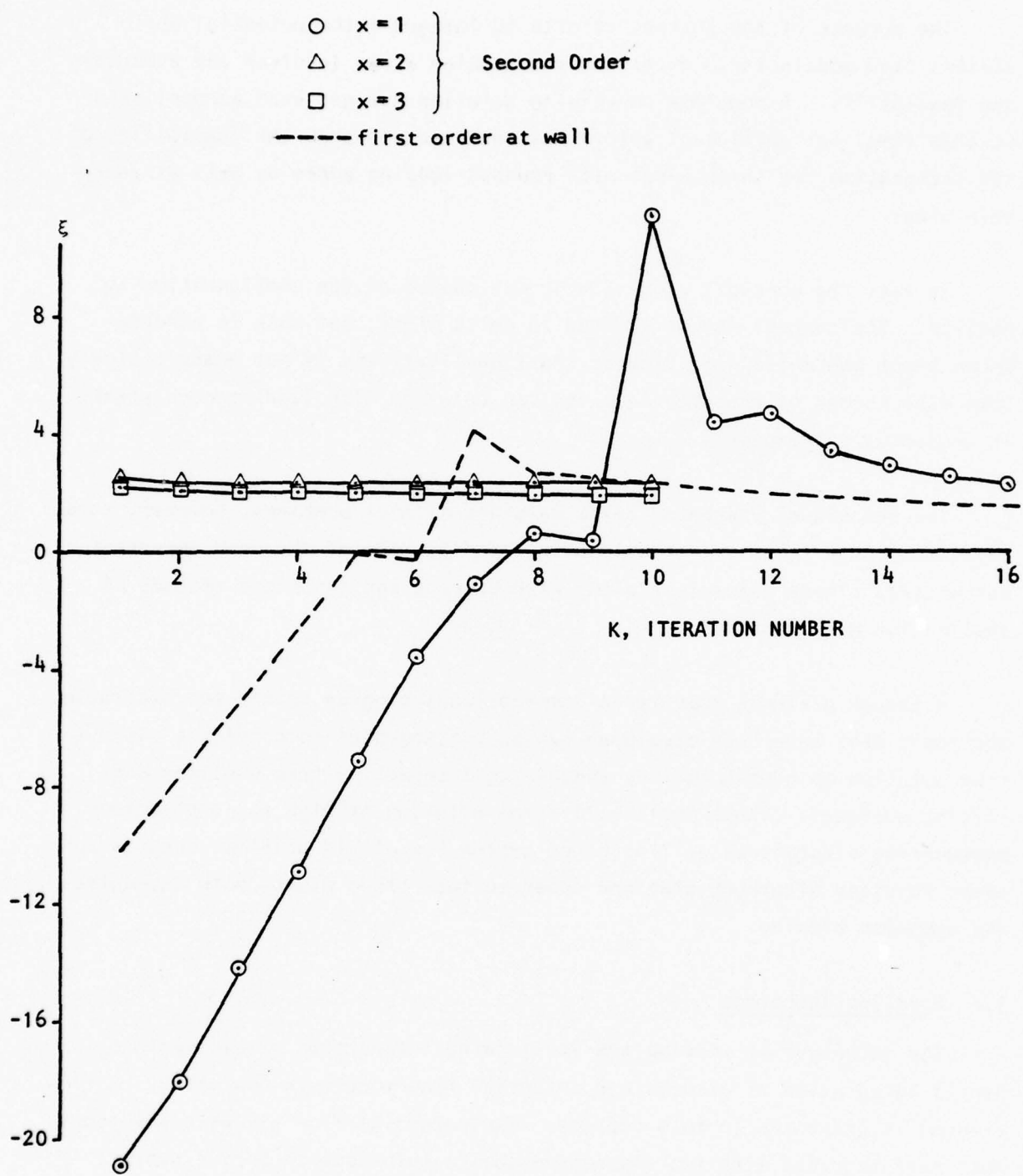


Figure 17 Effect of Initial Values on Iteration History, ξ at $y = 0$, $z = .462$

3. INTEGRATION OF THE VISCOUS BOX AND ELLIPTIC POTENTIAL FLOW MODELS

3.1 General

The purpose of the current efforts to integrate the potential and viscous flow models is to determine the problem areas involved and ascertain the feasibility. A complete converging solution has not been accomplished at this time, but sufficient effort has been made to show the feasibility of the integration for thick wings with rounded leading edges as well as sharp thin wings.

To test the concept, a delta wing was chosen as the configuration to analyze. The concept is not limited to delta wings, but much is already known about the delta wing flow at least qualitatively if not quantitatively. Some discussions of the technique applied to wings with leading edge strake is presented subsequently.

The techniques presented below were not without problems; however, these problems proved to be valuable in understanding some of the more important parameters. These parameters along with correct and incorrect methods of application are discussed.

Although a single converging computational program is not yet available, the tools that have been developed can be put together to provide a viscous flow solution to configurations containing interacting free vortices and lifting surfaces. These tools will allow solution of high angle-of-attack maneuvering aircraft as well as other vortex flow-field problems such as up-swept fuselage afterbody drag and upper surface blown wings, both chordwise and spanwise blowing.

3.2 Modeling Technique

The technique of solving the vortex/wing interaction problem with a hybrid integration of viscous and potential flow models is now clear. A flow diagram is presented in this section. Two potential flow elliptic solutions must be integrated with two viscous parabolic solutions to form a hybrid solution containing the best of each model. The four models are:

- (1) Thick or thin wing potential flow model
- (2) Free-vortex system
- (3) Viscous box
- (4) Leading edge boundary layer.

Figure 18 shows a flow diagram for integrating these models. At this time only the thin wing, sharp leading edge delta wing has been investigated. In general, however, the four methods are combined as follows. After a suitable first estimate of the free vortex system (strengths and positions, section 3.3), the free-vortex system is combined with the thick or thin wing potential flow model. The model provides the pressure distribution around the leading edge as well as boundary velocities on the viscous box boundaries. The pressure distributions are used in the leading edge boundary layer solution to get vorticity fed to the viscous box. With initial boundary conditions defined, the viscous box is then used to find more exact locations and strengths of the free-vortex system. Then the procedure is repeated until convergence occurs. Convergence occurs when the total strength and centroid of the circulation in the viscous box do not change more than certain prescribed limits. These procedures are detailed in Section 3.2.2.

The above procedures have been applied to a simple thin sharp-edge delta wing with 65° leading edge sweep at 22° angle of attack. This angle was chosen because it should have the leading edge vortex with incipient burst near the wing trailing edge. Figure 19 shows a planform and projected view of the wing with viscous boxes in place. Note that the front of the box starts at the leading edge. In a subsequent section it is noted the box should extend slightly ahead of the leading edge of the wing. More boxes would be desirable for detailed solution, but to keep computer time down while developing the procedure, only six boxes are used. The free-vortex system from the wing apex to the first box should be extrapolated according to the relations used for approximating the initial vortex system (see 3.2). This assumption will not significantly affect the overall results or purpose of this effort.

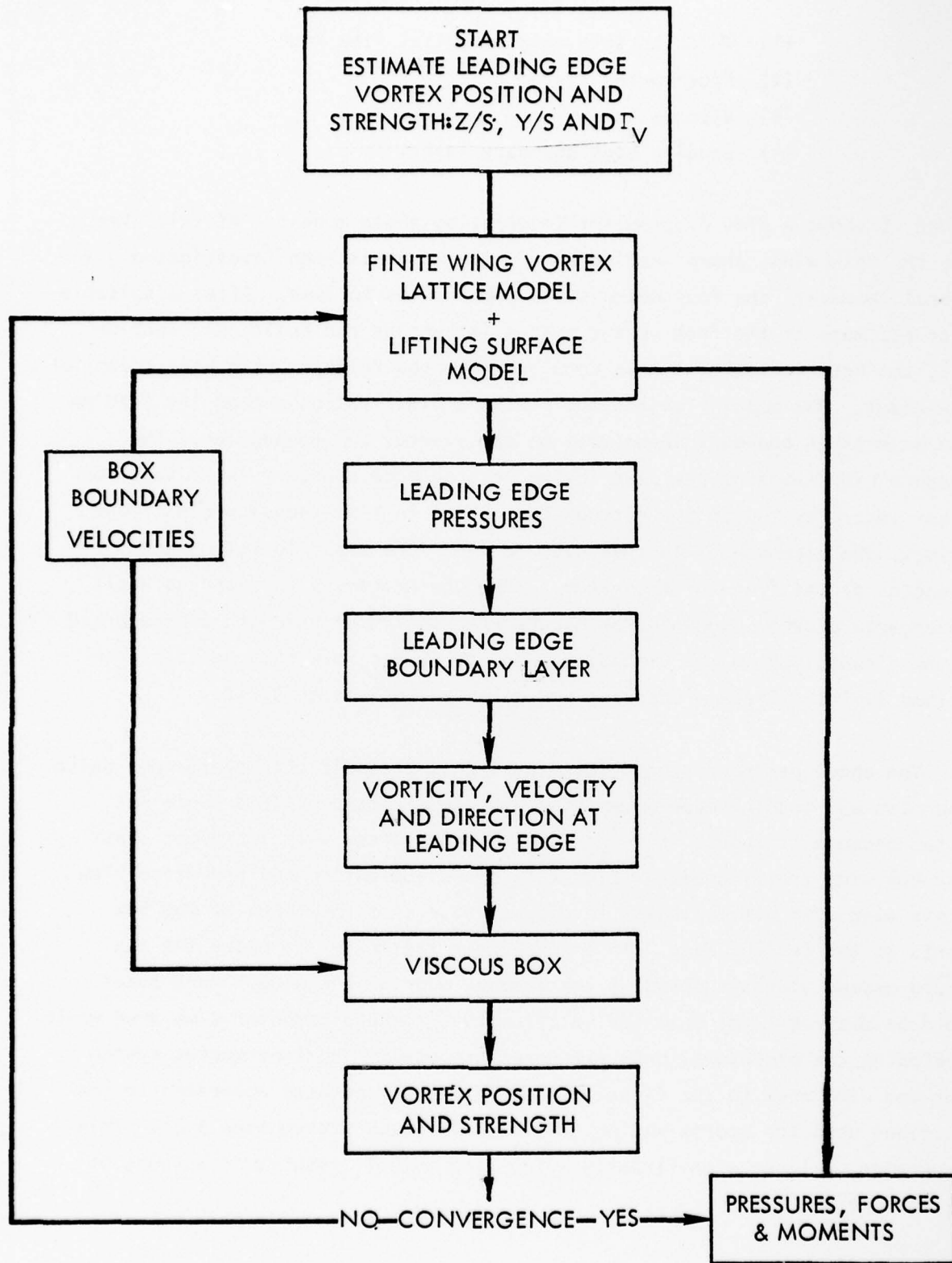


Figure 18 Flow Diagram for Wing Vortex Viscous/Potential Flow Interaction Models

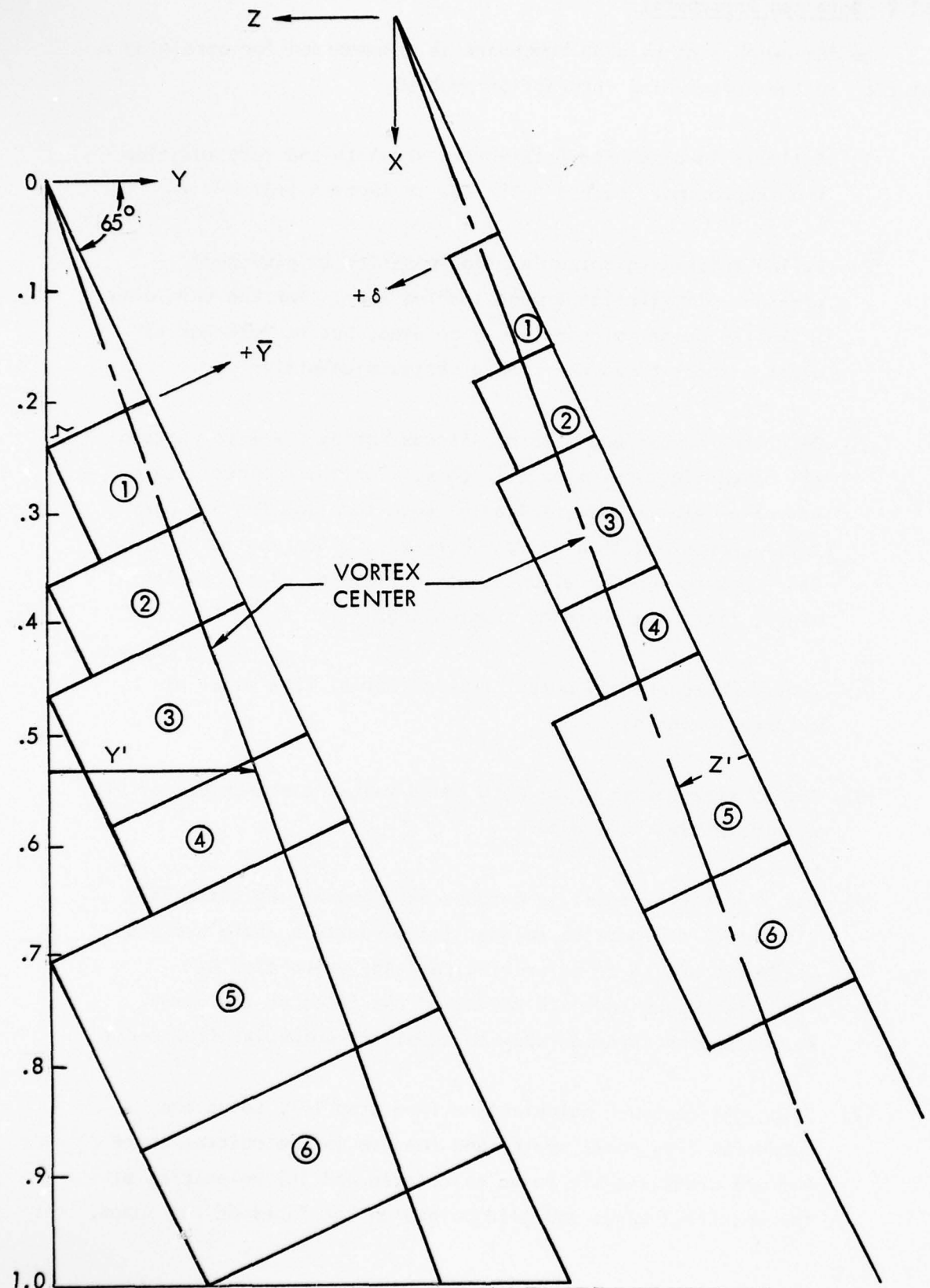


Figure 19 Viscous Box System for 65° Delta Wing

3.2.2 Detailed Procedures

The following step-by-step procedure is recommended for obtaining a solution to the vortex/wing interaction problem.

- (1) Estimate leading edge free-vortex strength and core position from approximate method described in Section 3.3.
- (2) Define thick wing potential flow paneling to give good pressure distribution around leading edge. For the thin wing a smaller number of panels may be used, but be sure not to place viscous boxes near bound vortex elements.
- (3) Determine number and size of viscous vortex boxes to contain all of vorticity of step (1) above. For thick wings, start box on an element aft of leading edge to allow for boundary layer growth and leading edge curvature. See Section 3.6. Start box near collocation points at leading edge. For thin wings, start box ahead of leading edge.
- (4) Provide card or tape output from potential flow model of collocation points.
- (5) Set up free-vortex model with bound vortex elements compatible with potential flow model.
- (6) Use free-vortex model to compute (a) downwash at potential flow model collocation points, (b) velocities where surface pressures are to be calculated, and (c) velocities at specified edges and grid points on the faces of the boxes. Put output on cards or tape to supply to potential flow model.
- (7) Using the downwash calculations from step (6), solve the potential flow model system and compute (a) velocities where surface pressures are to be calculated and (b) velocities at the specified edges and grid points on the faces of the boxes.

- (8) Add velocities of steps (6) and (7) for surface pressures and box locations to get total three component velocities.
- (9) Convert surface velocities to pressures and solve the boundary layer equations for flow around leading edge into viscous boxes.
- (10) Beginning with the first viscous box, use the *viscous box* method to compute the flow field in the box, at its face, its lee end and desired stations in between.
- (11) Use vorticities and velocities computed in step (10) for the lee end of box 1 for input to box 2 where box 1 covers box 2. See Section 3.5.
- (12) Where the face of box 2 is not covered by the lee end of box 1, use the velocities computed from the free vortex system and potential flow model for input to the face of box 2. See Section 3.5.
- (13) Repeat steps (10), (11), and (12) for all of the remaining boxes.
- (14) At each station where viscous box calculations are made, integrate the vorticity to obtain the total circulation about the box and its centroid.
- (15) Divide the box at each station into approximately negative and positive vorticity and find the centroid and strength of circulation for each area. See Section 3.7.
- (16) Define a new free-vortex system based on the distributed circulation computed in step 15. See Section 3.4.
- (17) Repeat steps 6 through 14 and check to see if total circulation and centroid changes are within prescribed limits (say 2 or 3%).

(18) If step (17) converges, calculate overall forces and moments and pressure distribution with the combined free-vortex model of step (16) and the thick wing potential flow model. Pressures at collocation points should be sufficient.

The following sections provide additional detail of the above steps.

3.3 Approximation for Estimating Vortex Strength and Position

A correlation of data from various experiments and the theory of Kandil, et al.⁶, has been made to provide the vortex position as a function of the parameter " a " = $\alpha/\tan\gamma$, where α is the angle of attack and γ is the angle made by the wing leading edge and the root chord. Figure 20 shows this correlation of various experimental data^{9,10}. Some of the various values of X/C_R are given. There is some scatter due to X/C_R varying but does not seem consistent. Therefore, a line is put through the points with the conical flow Smith theory as a guide¹¹. The value of " a " for the wing we have chosen to analyze is 0.8234 ($\alpha = 22^\circ$). This is in between the two sets of data shown in Figure 20.

To determine the effect of " a ", a crossplot is made in Figure 21. Again using Smith as a guide, lines are drawn for y and z as a function of " a ". This is crude for more values of " a " are needed from experiment. For our value of " a " the curve of Figure 20 gives good agreement with the vertical location of the vortex found in our laser velocimeter tests.

Vortex strength is determined as a function of X/C_R , α and γ and is plotted in Figure 22. Theoretical values for two delta wing configurations, analyzed in Reference 6, have been correlated to give a universal value K_V as a function of X/C_R , where

$$K_V = \frac{\Gamma}{U_\infty S \sin^2\alpha \cos\alpha} \quad (14)$$

Note, $K_V \sin^2\alpha \cos\alpha = C_{LV}$ as given by Polhamus, Reference 3, in his suction analogy. This is not the same K_V but the form and purpose is similar. It should be noted that the Γ obtained from Figure 22 does account for the

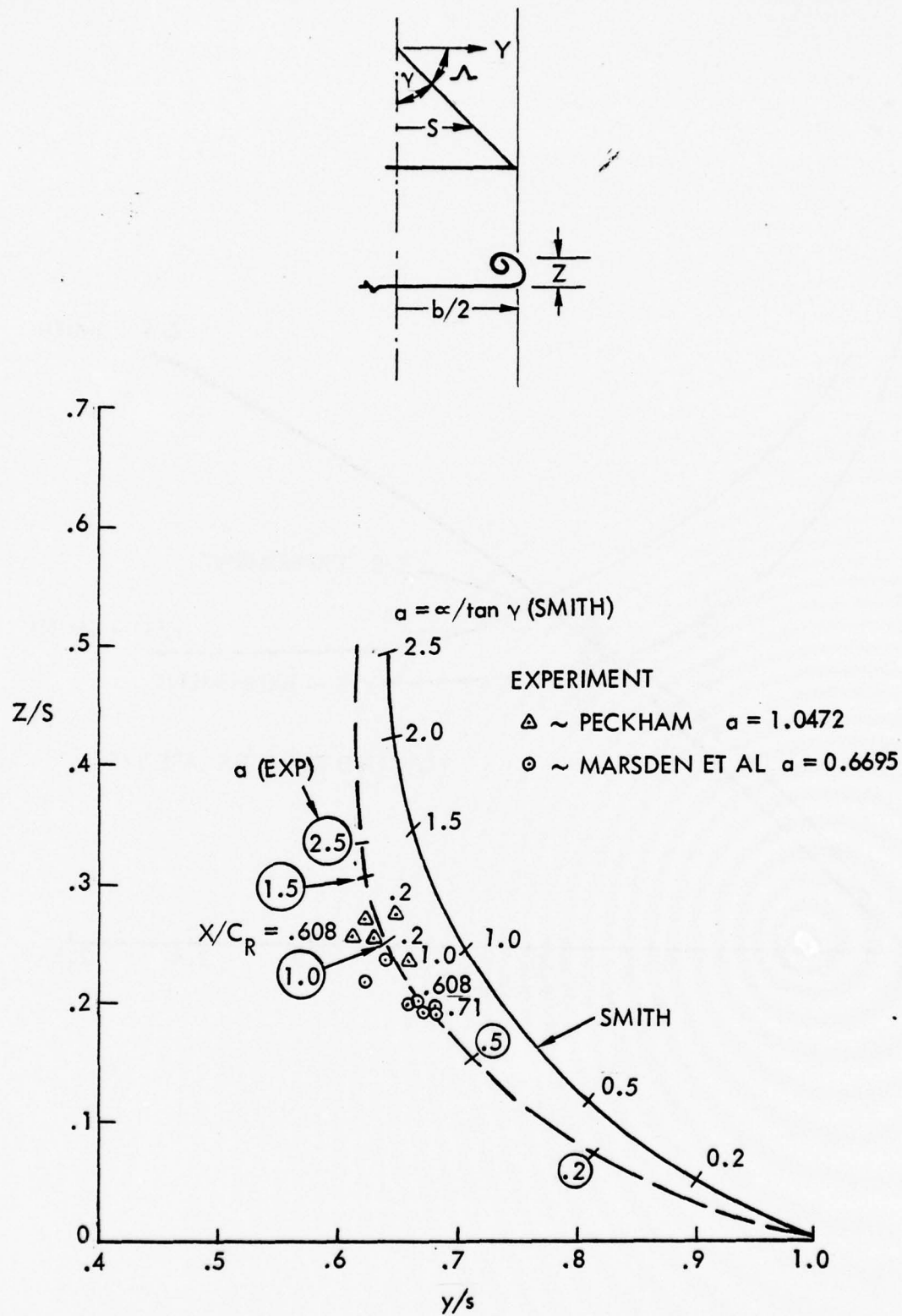


Figure 20 Vortex Core Location for Flat Delta Wings

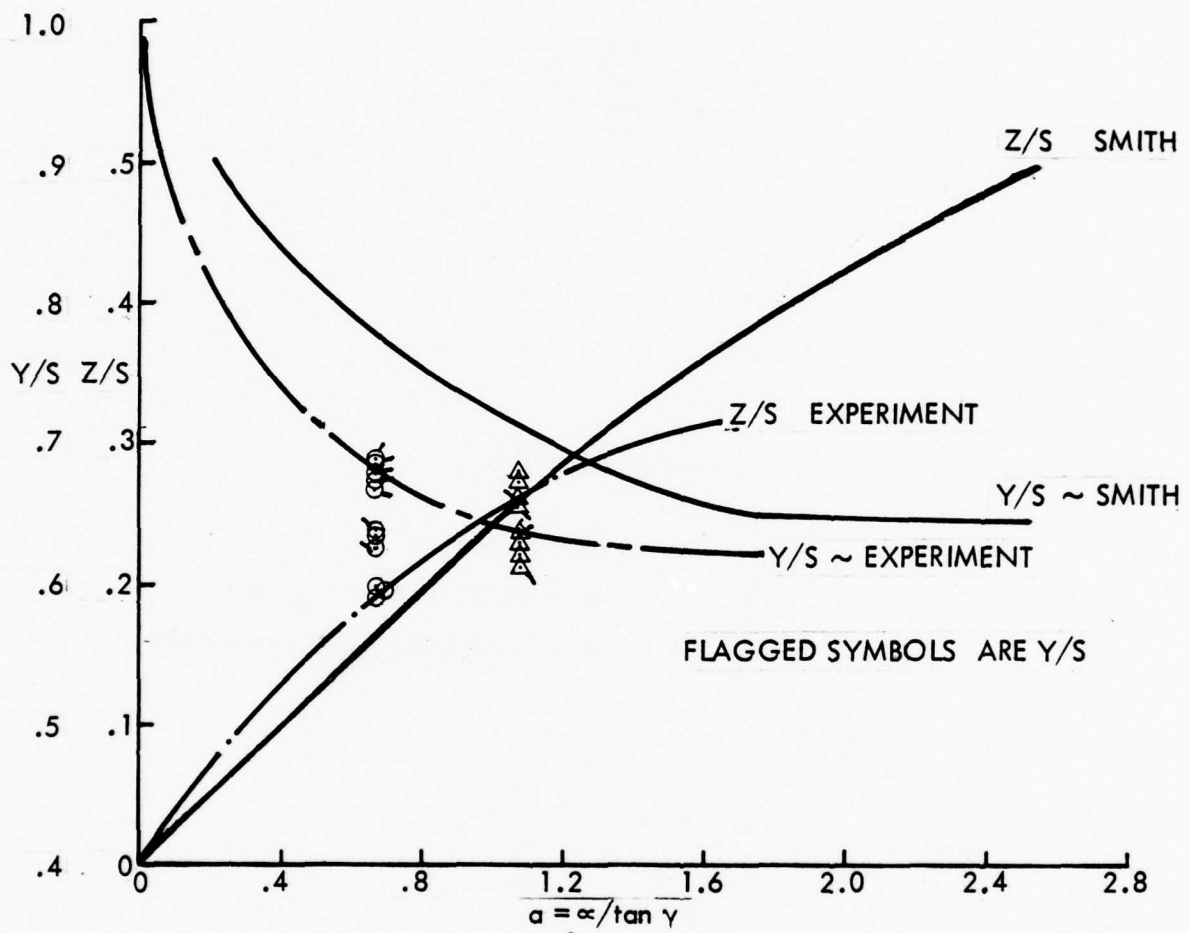


Figure 21 Vortex Location for Flat Delta Wings

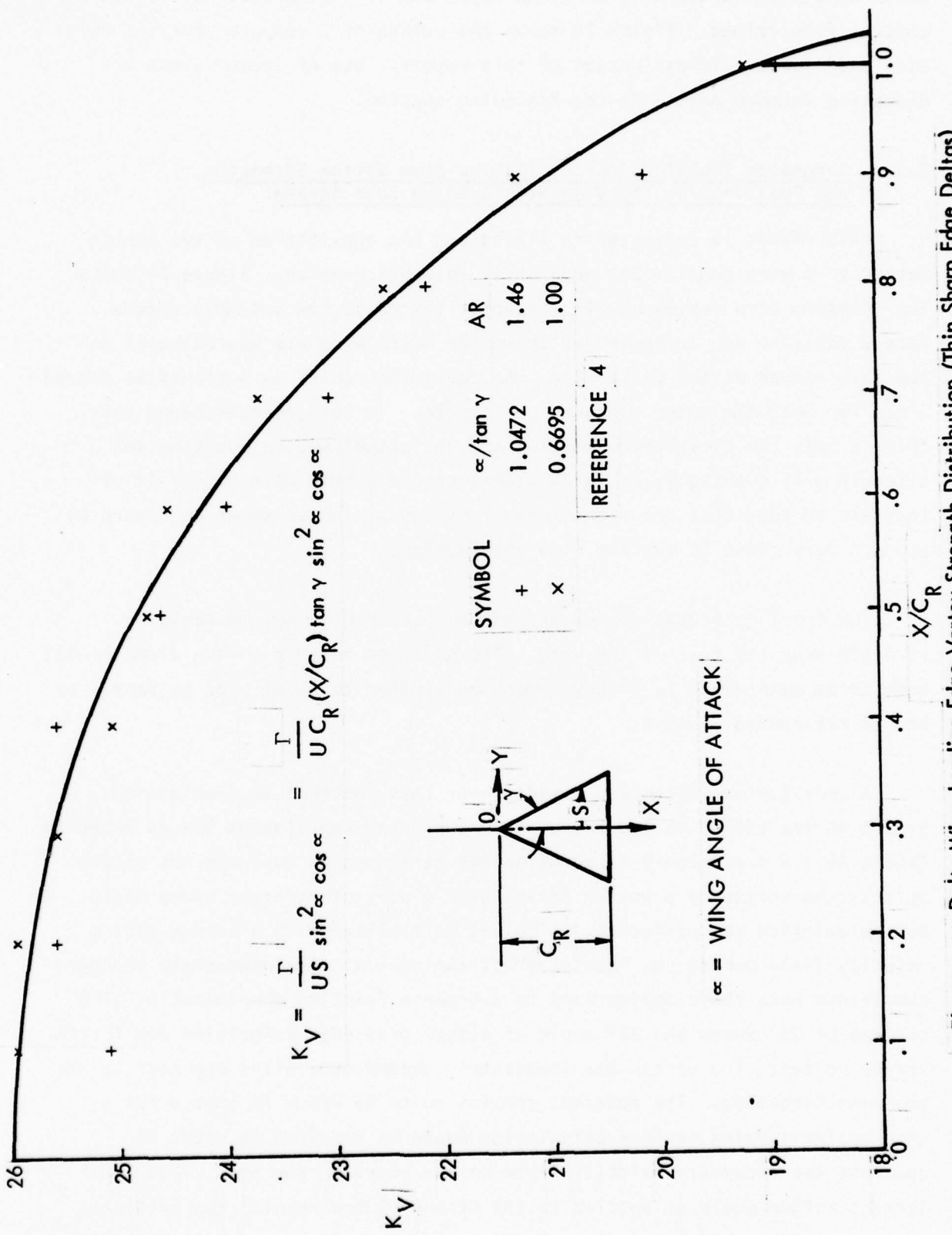


Figure 22 Delta Wing Leading Edge Vortex Strength Distribution (Thin Sharp Edge Deltas)

Kutta condition at the wing trailing edge, and this contrasts with Smith's conical flow values. Figure 23 shows the values of Γ computed for the delta wing used for the investigation of this report. Use of these values are discussed in more detail in the following section.

3.3.1 Suggested Technique for Estimating Free Vortex Strengths and Positions on the Wing With Leading Edge Strake

This effort is suggested to illustrate the application of the hybrid method to a very complex but apparently solvable problem. Figure 24 shows the planform of a semi-span wing recently tested at low subsonic speeds. Vortex position and strength for the outer basic wing are approximated in the same manner as the delta wing. An equivalent delta is outlined as dotted lines for both the outer wing and the strake. It must be remembered that this is only the first approximation and the actual vortex position and strength will eventually be calculated with the hybrid method. It is of interest to note that the approximate vortex position as shown in Figure 24 appears very close to surface flow observations.

The trailing strake vortex aft of the strake will not increase in strength over the rest of the wing. The position of this vortex element will have to be determined by tracking methods similar to those used by Kandil or Rao in References 5 and 6.

A very limited attempt was made under this contract to simulate the strake vortex effect on the outboard vortex using the viscous box as shown in Figure 24. A preliminary computation was performed to evaluate the effect of a strake vortex on a vortex formed over a wing of moderate sweep angle. A box calculation was performed, which was initialized with a vortex plus a velocity field due to the "upstream" strake vortex. The downstream boundary conditions were those appropriate to a Green's function approximation of a surface of 25° sweep and 22° angle of attack plus edge velocities due to the strake vortex. The vortex was immediately washed out, after one step in the spanwise direction. The apparent conclusion to be drawn is that a fully interacting lifting surface calculation would be required in order to generate the necessary velocity field on the edges of the box. Thus, the lattice method would be applied to the strake-plus-wing with two vortices

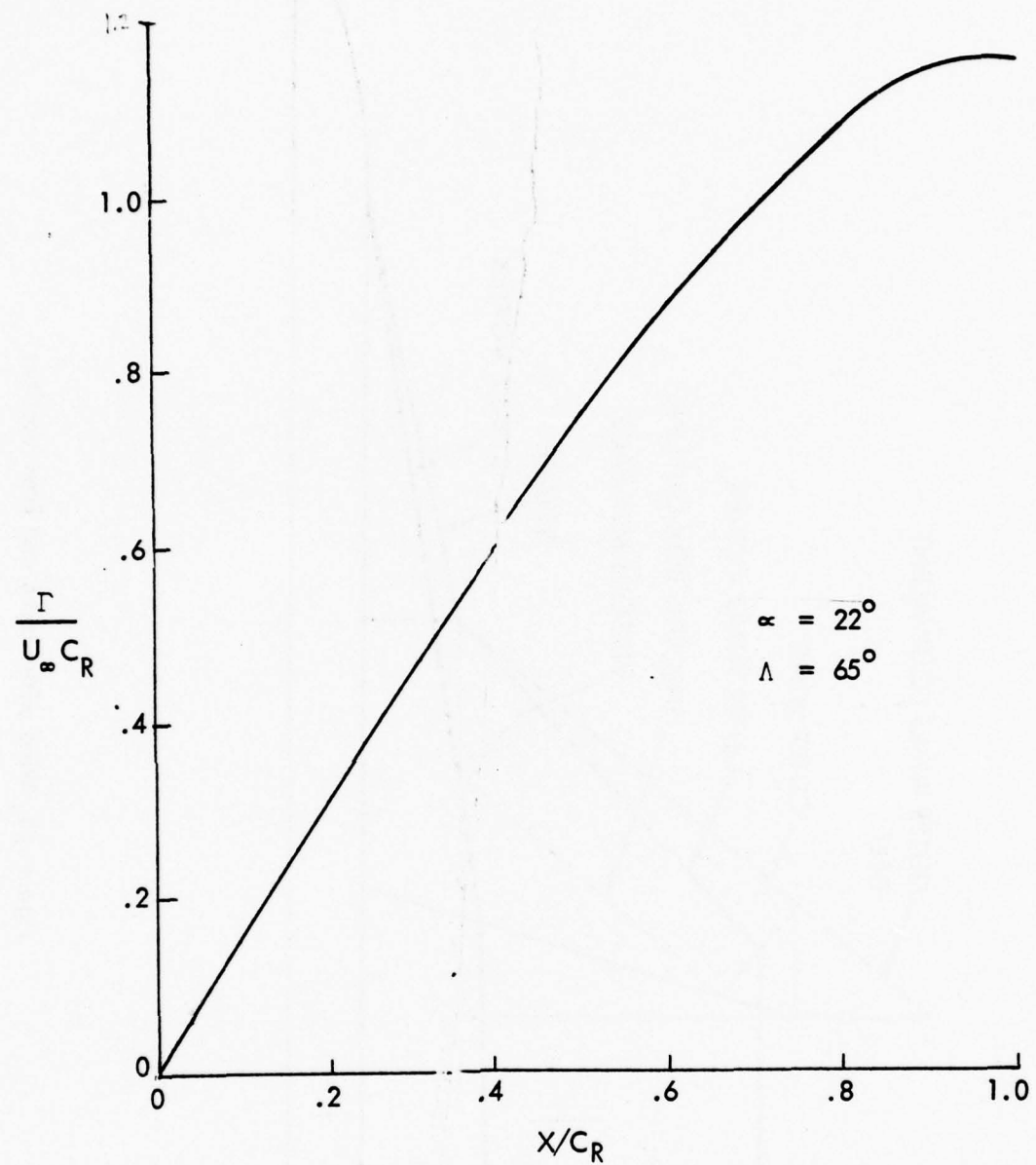


Figure 23 Vortex Strength Input for 65° Delta Wing

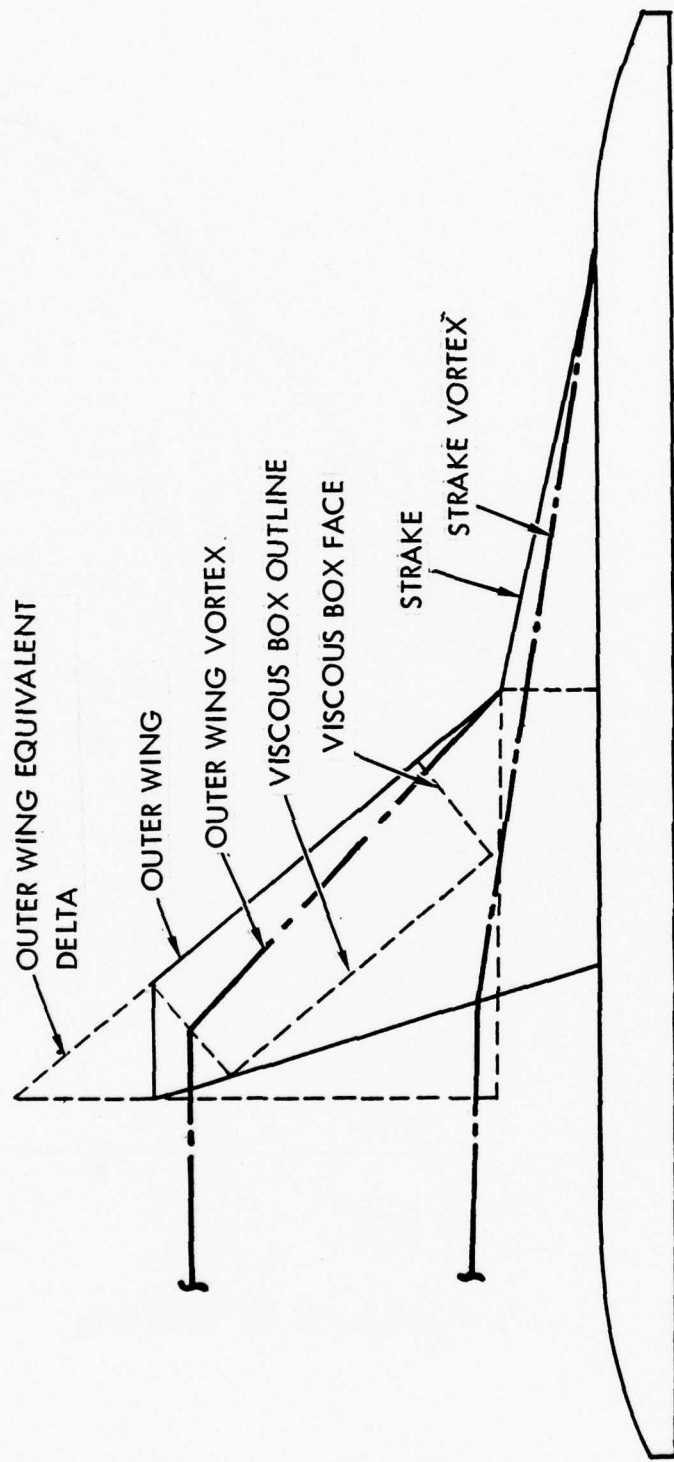


Figure 24 Wing with Strake and Free Vortices

imposed at approximately the correct locations and with prescribed strength distributions. With this information, plus information about the separating region upstream, the box computation could be expected to estimate the viscous development in the vortex formation region.

3.4 Vortex Lattice Method

For the thin delta wing investigated in the feasibility study, the flow has been modeled with a vortex lattice representation of the wing surface and with two alternative vortex system representations of the separated leading edge vortex. These provide initial conditions for input into the vorticity box program, which performs a viscous calculation with the Navier Stokes equations over rectangular box faces normal to the wing surface, see Figure 19. First, the velocities induced by the leading edge vortex system are calculated at the collocation points on the wing and on the faces and edges of the boxes. Then, the velocities induced by the wing, under the influence of the leading edge vortex, are found for the faces and edges of the boxes and superimposed on those induced by the leading edge vortex system. This provides a starting condition from which the vortex strength and locations can be modified via the output of the vorticity box program. Output of the vorticity box is discussed in Section 3.7.

The vortex lattice arrangement is shown in Figure 25; it features a spanwise cosine spacing of nine panels and five equally spaced chordwise panels. The spanwise panel spacing concentrates them at the leading edge and near the inboard edge of the rolled-up vortex sheet.

The first of the leading edge vortex systems is shown in Figure 26. There are five vortex systems in all that progressively feed into the core vortex, the location and strength of which was defined using a conical assumption and guidance from experimental data (Section 3.3). The individual vortex systems consist of vortex segments which are input in order from the root to the leading edge, from the leading edge to the core, and then to the core position at the trailing edge and thence downstream. The root to leading edge segment is aligned with the wing bound vortex.

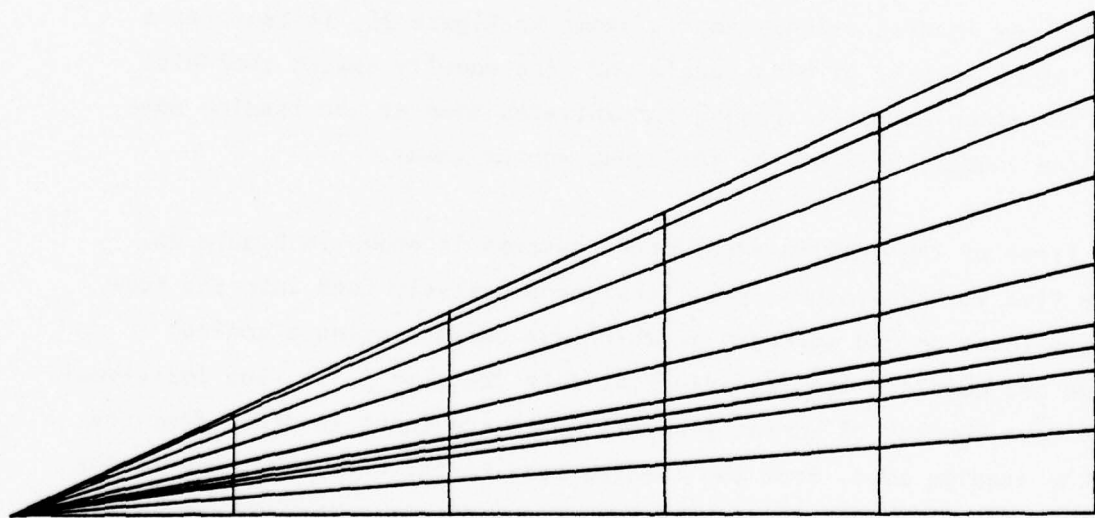


Figure 25 Wing Vortex Lattice

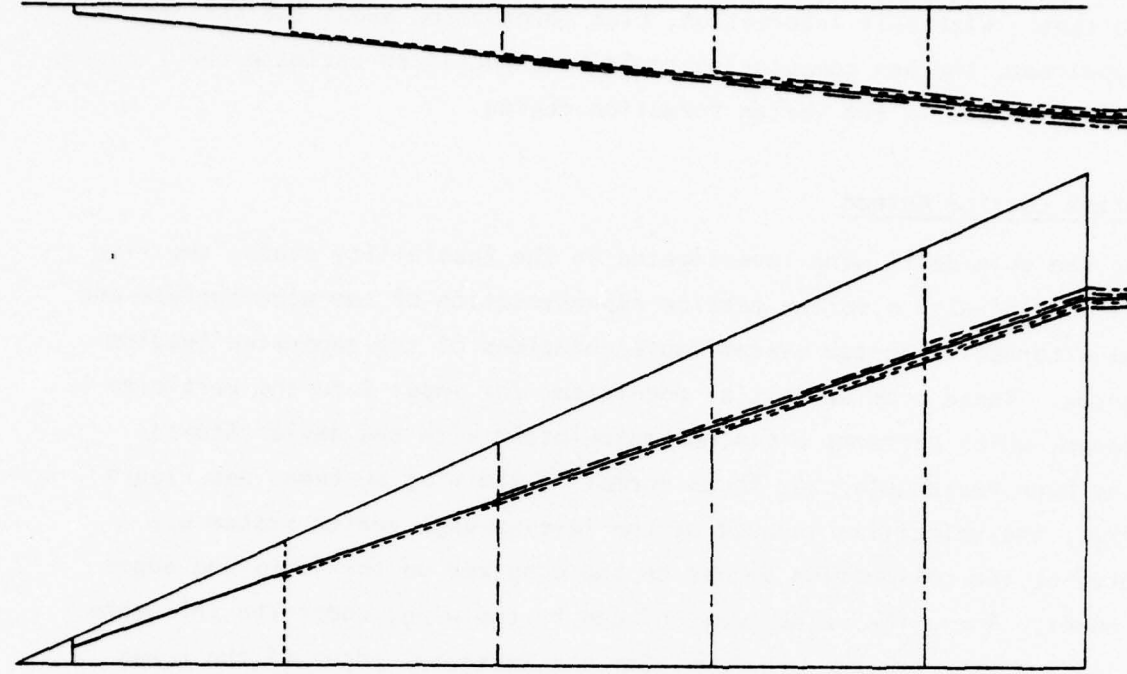


Figure 26 Discrete Leading Edge Vortex System

Results using this system are shown in Figures 27 and 28. The spanwise, vertical, and axial velocity perturbations are presented for the top edge of the second box. Most remarkable is the axial induction of flow for the leading edge vortex system. Also, velocity components are calculated for the inboard and outboard vertical edges of the box and demonstrate a strong upwash and strong lateral velocities on the outboard edge.

A second and more realistic leading edge vortex system which distributes vorticity in the feeding sheet is shown in Figure 29. There are two vortex systems at each chordwise position, one of which feeds into the core and the other of which feeds into the vortex sheet. The filaments feeding into the sheet are arbitrarily assumed to feed into the vortex core, and the vortex systems at each chordwise position has the same total strength as that assumed for the concentrated vortex system. Also, the vortices are input in a manner similar to that for the concentrated vortex, except that more vortex segments must be used to model the sheet. For the first pass, the filaments comprising the vortex sheet are assumed to be distributed along a radial arc from the leading edge to a position directly over the vortex core. This sheet position is determined later by the vorticity box. Once the vortex sheet filaments leave the chord position at which they are introduced, they are assumed to follow a straight conical line to their position on the trailing edge vortex sheet.

Figures 27 and 28 show the velocity components for this leading edge vortex system and are qualitatively similar to those of the concentrated vortex system. The most remarkable difference is the stronger vertical component induced on the outboard edge of the box due to the proximity of the vortex sheet filaments. Experimental data on these plots are discussed in Section 4.3.

3.5 Interface Between Different Size Vorticity Boxes

In order to apply the vorticity box calculation over a delta wing planform, it is necessary to vary box size while marching in the downstream direction, as indicated in Figure 19. Since the vortex grows with distance downstream, the physical dimensions of the box must increase in order to contain the motion free of boundary interference. The need for a curvilinear

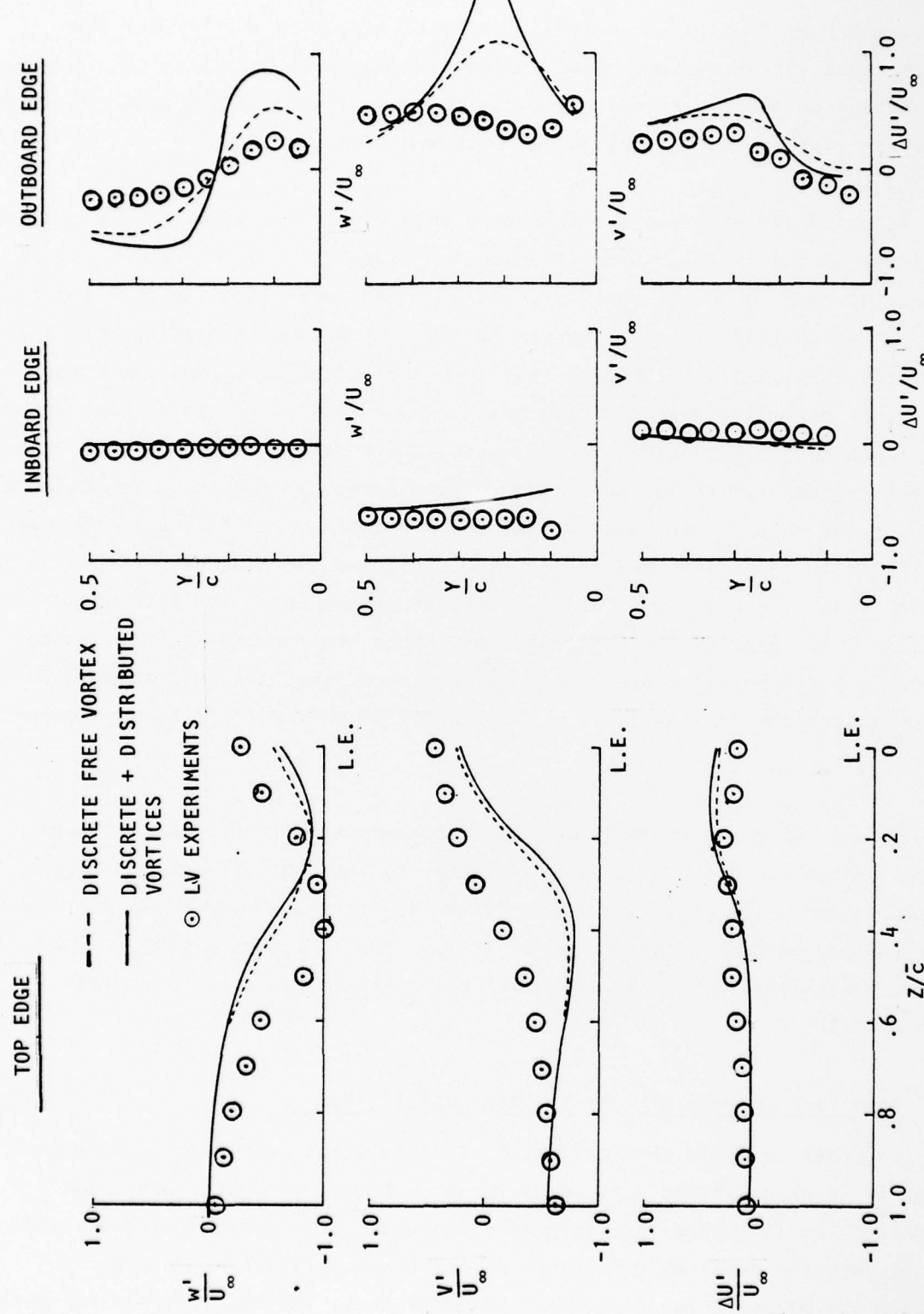


Figure 27 Velocities at Top Edge of Box 2 Face

Figure 28 Velocities at Side Edges of Box 2 Face

Figure 28 Velocities at Side Edges of Box 2 Face

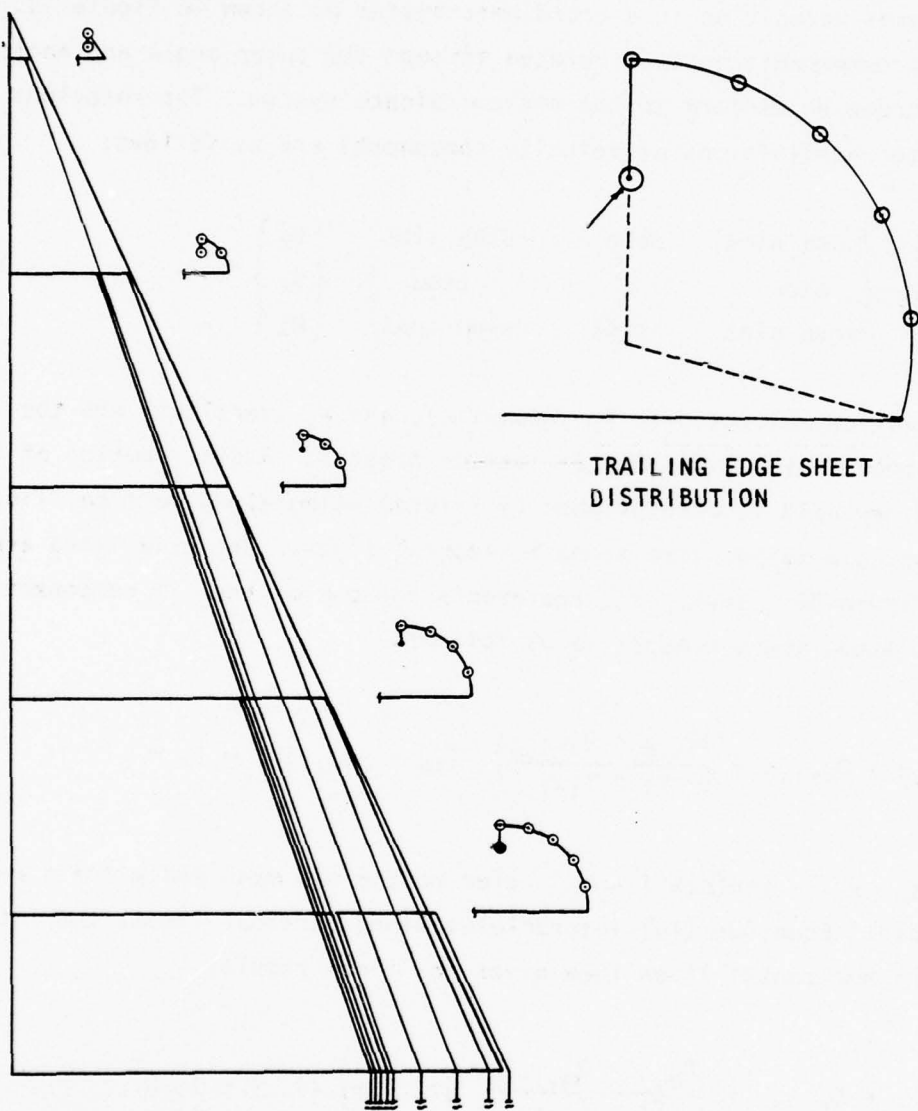


Figure 29 Distributed Leading Edge Vortex

coordinate system to treat this configuration is obvious. Such a formulation will be discussed in a later section. The present objective is to test the feasibility of coupling the viscous box with a potential flow model, and for this purpose the rectangular domain will suffice. The major requirements for implementing the coupling procedure are to read in boundary values from the lattice method and to perform, at each box interface, an interpolation of velocities and vorticities to the new grid points. The vortex lattice program generates velocities in a coordinate system as shown in Figure 19. These velocity components must be related through the sweep angle and angle of attack in order to conform to the box coordinate system. The rotations and appropriate redefinitions of velocity components are as follows:

$$\begin{Bmatrix} U \\ V \\ W \end{Bmatrix} = \begin{Bmatrix} \cos\alpha \sin\Lambda & \cos\Lambda & -\sin\alpha \sin\Lambda \\ \sin\alpha & 0 & \cos\alpha \\ \cos\alpha \sin\Lambda & -\sin\Lambda & -\sin\alpha \cos\Lambda \end{Bmatrix} \begin{Bmatrix} U_\ell \\ V_\ell \\ W_\ell \end{Bmatrix} \quad (15)$$

where U_ℓ (freestream direction), V_ℓ (spanwise), and W_ℓ (vertical) are the velocity components as defined in the lattice program. Redistribution of the solution to a new grid is accomplished by interpolating along vertical lines and interpolating a second time along horizontal lines. The grid lines are depicted in Figure 30. Thus, if Q represents any one of the six components to be interpolated, the procedure is as follows:

$$Q_{m,j} = Q_{i-1,j} + \left[\frac{Q_{i,j} - Q_{i-1,j}}{y_i - y_{i-1}} \right] (y_m - y_{i-1}), \quad i = 1, M \quad (16)$$

where $y_{i-1} < y_m < y_i$. Indices i and j refer to the old mesh and m and n refer to the new mesh. Equation (16) interpolates along vertical lines; the interpolation along horizontal lines then gives the final result:

$$Q_{m,n} = Q_{m,j-1} + \left[\frac{Q_{m,j} - Q_{m,j-1}}{z_j - z_{j-1}} \right] (z_n - z_{j-1}), \quad j = 1, N \quad (17)$$

where $z_{j-1} < z_n < z_j$. Thus, as is clear from Figure 30, the upstream solution is distributed to the new box, but its dimensional extent is unchanged. This

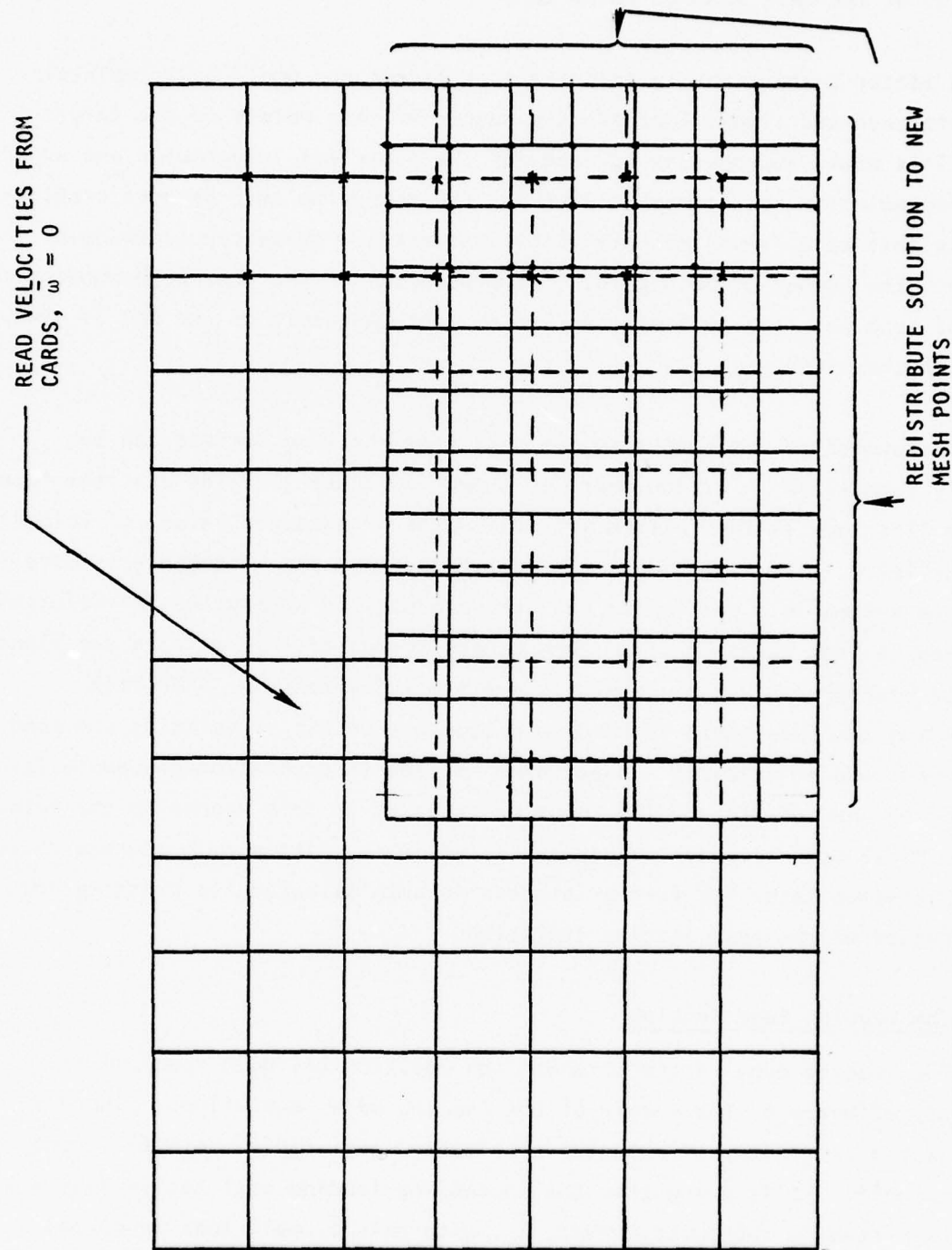


Figure 30 Box Interface Interpolation

leaves a portion of the new box without initial values. Velocities for this region are taken from the lattice program. The vorticity for this region is left zero except at the wall, where the no-slip condition must be satisfied. A starting value for the wall is computed from the given velocity field with velocity at the wall assumed to be zero.

A better arrangement in shifting to a larger box would be to maintain a constant mesh and simply increase the number of mesh points in the larger box. This would improve the accuracy of the numerical integration and avoid the interpolation requirement. However, the computing cost becomes prohibitive in this case, thus the only viable alternative presently is to hold constant the number of mesh points. For purposes of the present demonstration of mesh was held at $N=11$, $M=21$, so that the depth of the box is always one-half the width.

The procedure for computing one pass over the wing surface can be briefly summarized in a flow chart as shown in Figure 31. The upstream face of the first box is initialized with estimated or measured values of velocity and vorticity. The solution is then marched downstream. If there is more than one x-step in a particular box, the appropriate edge values of velocity are read in from cards (or from some other storage device) at each y-z plane and the boundary values of vorticity are similarly read in. For each succeeding box face, both interior and boundary values of velocity are read from cards and an overwrite is performed by the interpolation procedure for part of the new box face. The solution proceeds in this manner to the output of the final box. At each x-step the solution is written to a storage device, to be accessed later for further processing such as automatic plotting and preparation of the next lattice iteration.

3.6 The Leading Edge Problem

The leading edge vortex strength and position has been found to be strongly affected by the nature of the leading edge separation. Figure 32 shows a typical effect of changing the leading edge radius on a 67.1° swept delta wing¹². It is noted that the increasing leading edge radius causes a large increase in chordwise thrust, C_s , with only a small loss in normal force, C_N , or vortex lift. Also, the aerodynamic center is moving aft

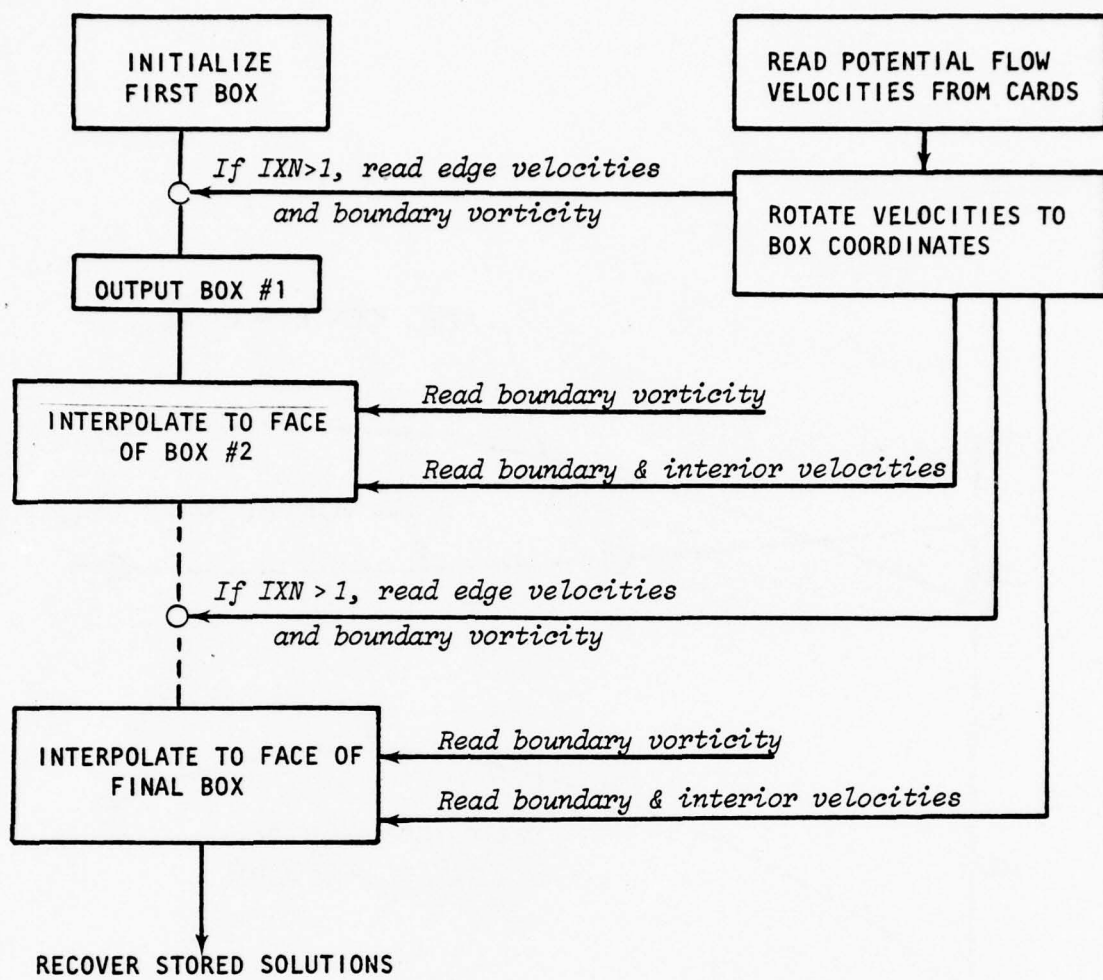


Figure 31 Procedure for Advancing the Viscous Solution

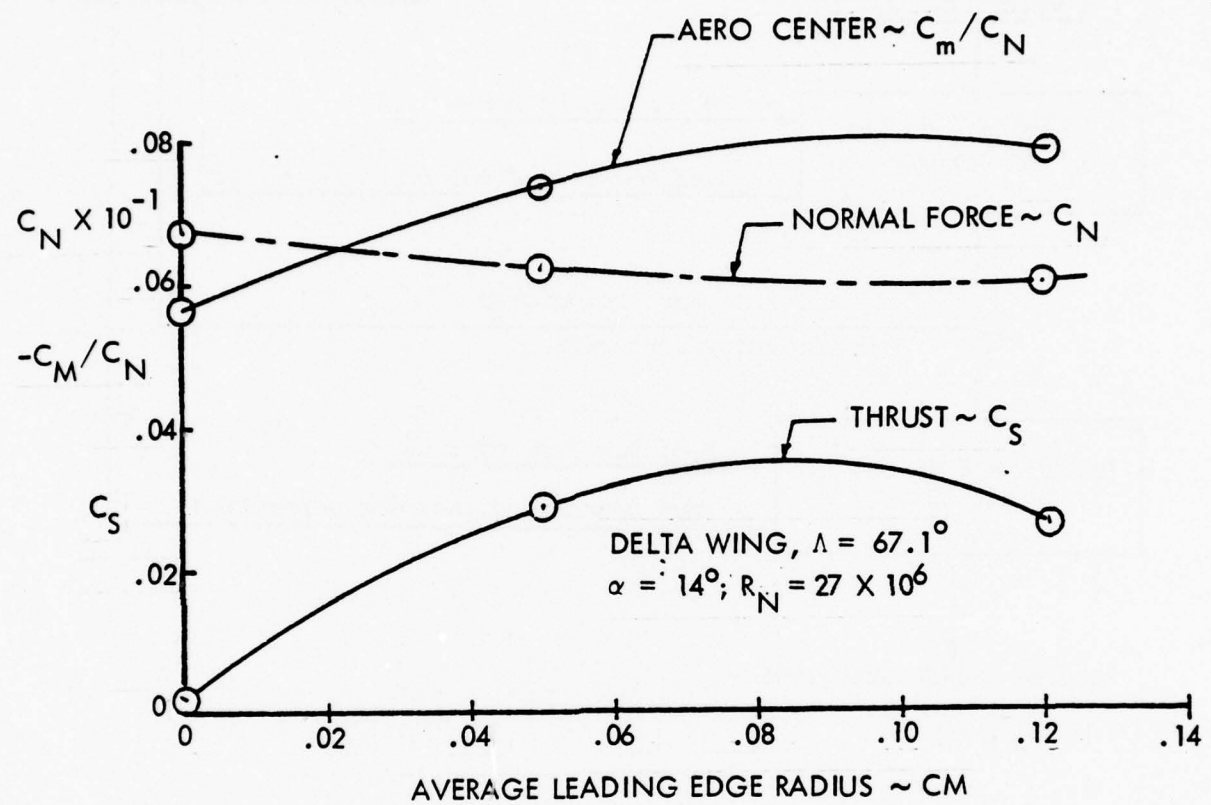


Figure 32 Effect of Changing Leading Edge Radius

indicating a shift aft of the leading edge vortex with increasing leading edge radius. This movement of the vortex core is associated with the orientation of the vortex sheet originating at the point of flow separation. The strength of the vortex is also related to the orientation of the vortex sheet and to the level of vorticity shed from the boundary layer. These viscous phenomena are critically affected by the design of the leading edge.

Obviously, the best leading edge design for supersonic cruise may not be the best for efficient subsonic or transonic speeds. It may not be the best for transient and stability effects. Therefore, a rounded leading edge may have to be designed to give the best all-around performance and stability. With the tools to analyze the rounded leading edge in the presence of a leading edge vortex, the most efficient all-around leading edge may be designed. It may well be that neither stability nor performance need be compromised.

The available theoretical tools for wing/vortex analyses are very sensitive to the starting conditions at the leading edge. In the thin wing potential flow solutions, such as those of References 5 and 6, it is correctly assumed that the vortical elements and velocity vectors at the wing leading edge lie in the plane of the wing, but their orientation in the plane must be assumed. Techniques using quadrilateral panels for the feeding sheet, such as that of Weber, et al.⁴, apparently avoid this orientation problem for thin wings. For thick wings, however, the panel would have to be oriented with the actual direction of the feeding sheet leaving the boundary layer. The "Viscous Box" method has also shown (Sections 2.2 and 2.4) that the orientation and strength of the vorticity coming from the boundary layer into the box is critical. Therefore, it is quite conclusive that a boundary layer analysis at the wing leading edge is necessary.

Additional computations must be made to represent the boundary layer region forward of the box. Strictly speaking, it is required to compute a boundary "region", i.e. a region including higher-order effects than those occurring in first-order boundary layer theory (see Figure 33). In order to establish with accuracy the forward edge velocity and vorticity values for the box, it is necessary to perform a computation from the wing attachment

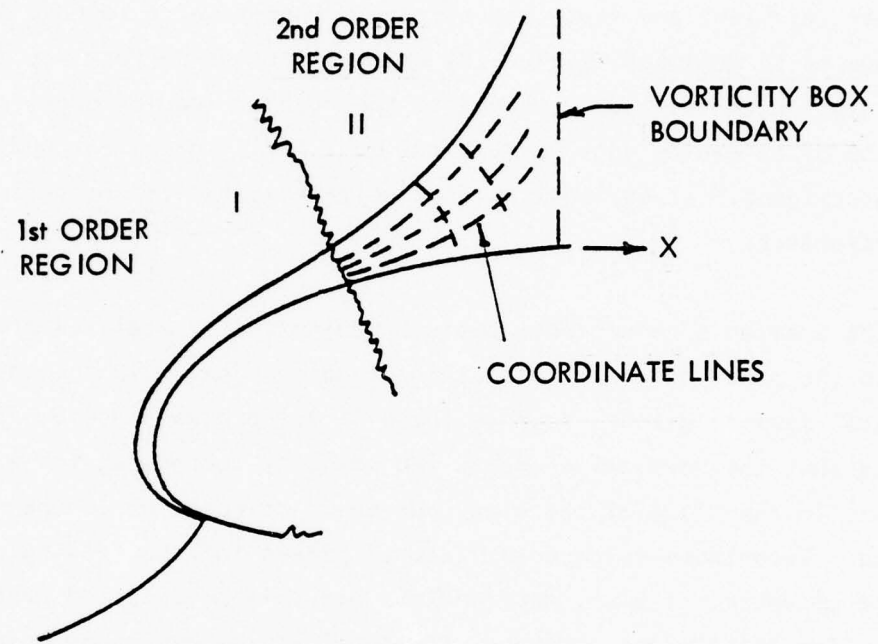


Figure 33 Section Showing First and Second Order Boundary Layer Domains

line through the boundary layer and into the second order, rapidly thickening, boundary layer region.

Recognizing the sensitivity of the viscous box vortex flow region to the vorticity imposed by the leading edge boundary layer region, it is essential that three dimensionality be accounted for in any model of the boundary region. For this purpose, it is deemed necessary and sufficient to apply the "infinite yawed wing" assumption. This method has proven quite fruitful in the analysis of boundary layers near attachment lines and even for some complete wings of sufficiently high aspect ratio¹³.

This boundary layer problem will be investigated in follow-on efforts of this program, and it will be applied to the thick leading edge configuration. Only the thin sharp edge wing is considered in this report.

The thin wing is not without leading edge problems for it is also necessary to know the strength of the vorticity being shed from the leading edge. It is also necessary to locate it appropriately on the leading edge of the vorticity box to assure that the vorticity is shed into the box. In the discussion of "Results of First Iteration for a Thin Delta Wing," Section 3.8, some problems related to this input vorticity are discussed.

Obtaining the leading edge vorticity for the thin sharp edge wing is not as readily available from theory as it is for the thick leading edge. Some theoretical or empirical techniques must be used other than vortex lattice to determine the pressure distribution on the lower surface of the thin airfoil which in turn is used to compute the boundary layer vorticity. At this time the theoretical method is not available, and vorticity deduced from laser velocimeter data (see Section 4.0) is used for input to the thin delta wing investigation.

3.7 Distributed Circulation from Viscous Box Results

After the first iteration of the hybrid viscous vorticity box method and potential flow vortex lattice method, circulation distribution can be defined from the vorticity box results. These distributions can in turn be used for

the second and following iterations of the vortex lattice method. A distributed free vortex system was discussed in Section 3.4

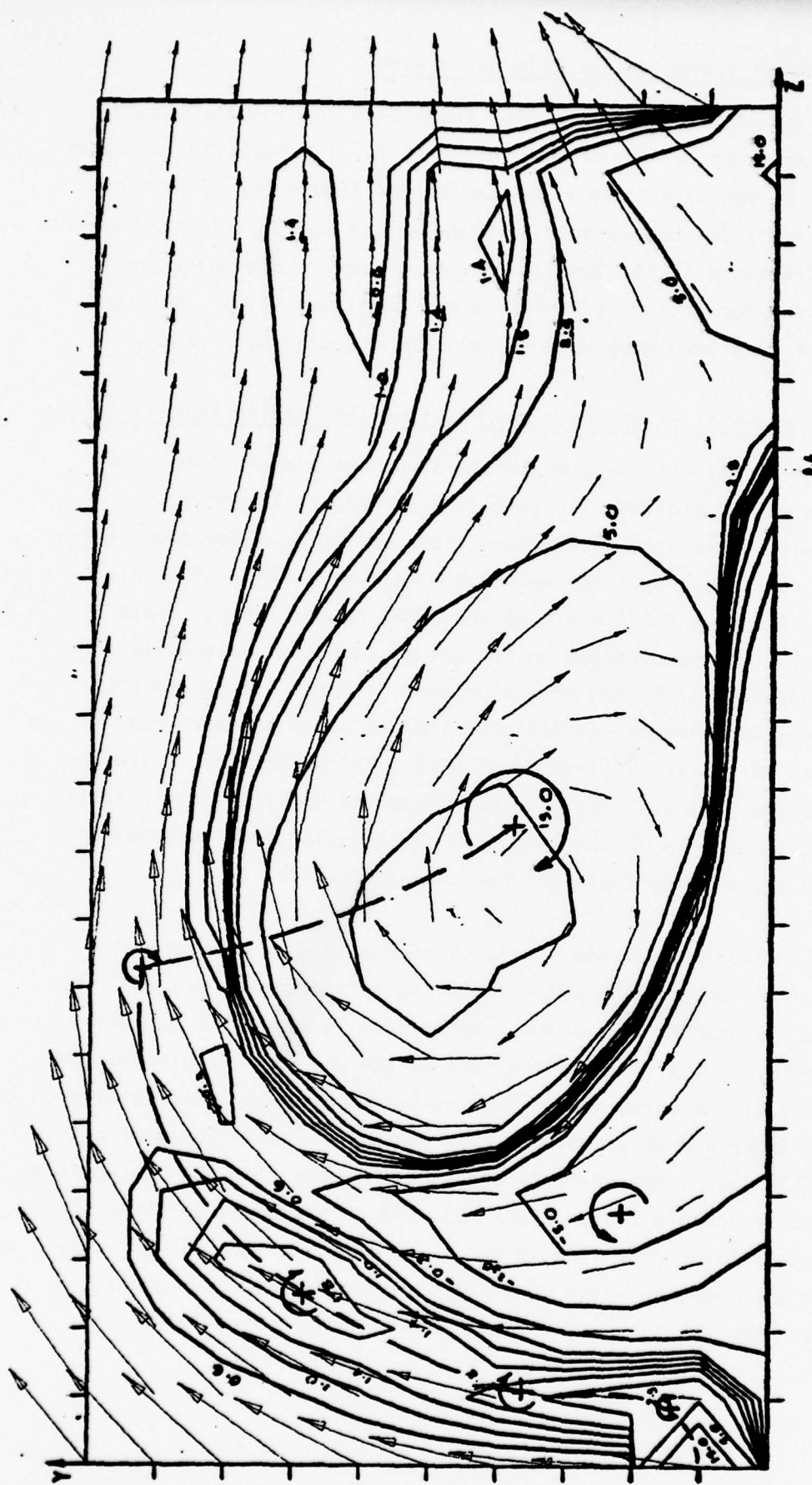
Figure 34 shows the lines of constant vorticity for one of the cases run for box one of Figure 19. The isovars shown are for the downstream end of box one or the upstream face of box two. Positive and negative discrete circulations can be formed as shown by the rotation symbols of Figure 34, where the circulation is

$$\Gamma = \iint_A \xi \, dA \quad (18)$$

and A is area chosen to represent the vortex core circulation or portions of the vortex sheet. The centroid of each circulation is obtained from moments. In the case shown, four elements make up the vortex sheet and one element for each of the remaining positive and negative vorticities make up all other circulation. The vorticity at the lower right corner of the box is not too realistic because this part of the box is too close to a bound vortex element of the vortex lattice. This gives unrealistic vertical velocities as shown in Figure 34.

It is noted that the vortex sheet is of unusual shape. This is not as expected and recommendations for correcting this are given in Section 3.8.

In order to maintain a realistic representation of the distributed free vortex system, the elements chosen to make up the vortex sheet of box one will have to remain constant as they move through the boxes. It will therefore be necessary to investigate the vortex sheet at each box face to obtain its total circulation, then divide it into areas that will integrate to give the same circulation elements as previously generated in the preceding face; so, each new box face will contain each of the elements previously generated plus one more for new vorticity being fed into the box. This method will be compatible with the distributed free vortex lattice discussed in Section 3.4.



SOLUTION AT $X = 1.100$ $0Y.02 = 0.0500$
PLOT OF XI-COMPONENT OF VORTICITY.

Figure 34 Velocities and Isovortices for Aft Face of Box One

3.8 Results of First Iteration for Thin Delta Wing

The various programs and the modeling techniques for integrating the programs have been given in Section 3.1 through 3.7. The modeling technique has been applied to the thin delta wing planform of Figure 19. Only one angle of attack (22°) is considered. Both the single and distributed free-vortex systems discussed in Section 3.4 have been used to determine the boundary conditions for each of the six viscous vorticity boxes. Viscous flow computations have been completed for all the boxes in both cases.

3.8.1 Input for Free-Vortex Strength and Position and Leading Edge Vorticity

To begin the iterations the free vortex strengths and positions are estimated by the method presented in Section 3.3. Figure 23 shows the estimated free-vortex circulation strength distribution as a function of the fraction of the root chord C_R . The value of $a = \alpha/\tan\gamma = .8234$. For this level the values of Y/S and Z/S are 0.66 and 0.22, respectively. These positions are not fixed percentages on the actual case, but reasonable estimates are made for initiaiton of the program. It was discovered after much of the effort was already accomplished that an error had been made in reading the value of Y/S at .75 instead of 0.66. This makes the vortex too close to the leading edge and both the laser data and vorticity box results indicate the vortex core is further inboard. This indication from the vorticity box is a good sign that convergence is possible.

Another input required is the vorticity at the leading edge of each vorticity box. This information was not available from theory but the laser data was at least a good approximation. Laser data is available for this estimate from only one box, i.e. at the face of box 2. At this station, the vertical velocity was measured along lines normal to the wing leading edge at various heights above and very near the wing surface. Due to the physical arrangement of the laser, measurements could not be made right at the surface level. The results are plotted in Figure 35. If points could be obtained across the boundary layer on a line in the plane of the wing, the vorticity would simply be the boundary layer edge velocity divided by the boundary layer thickness. The data is very limited to accomplish this, but a line

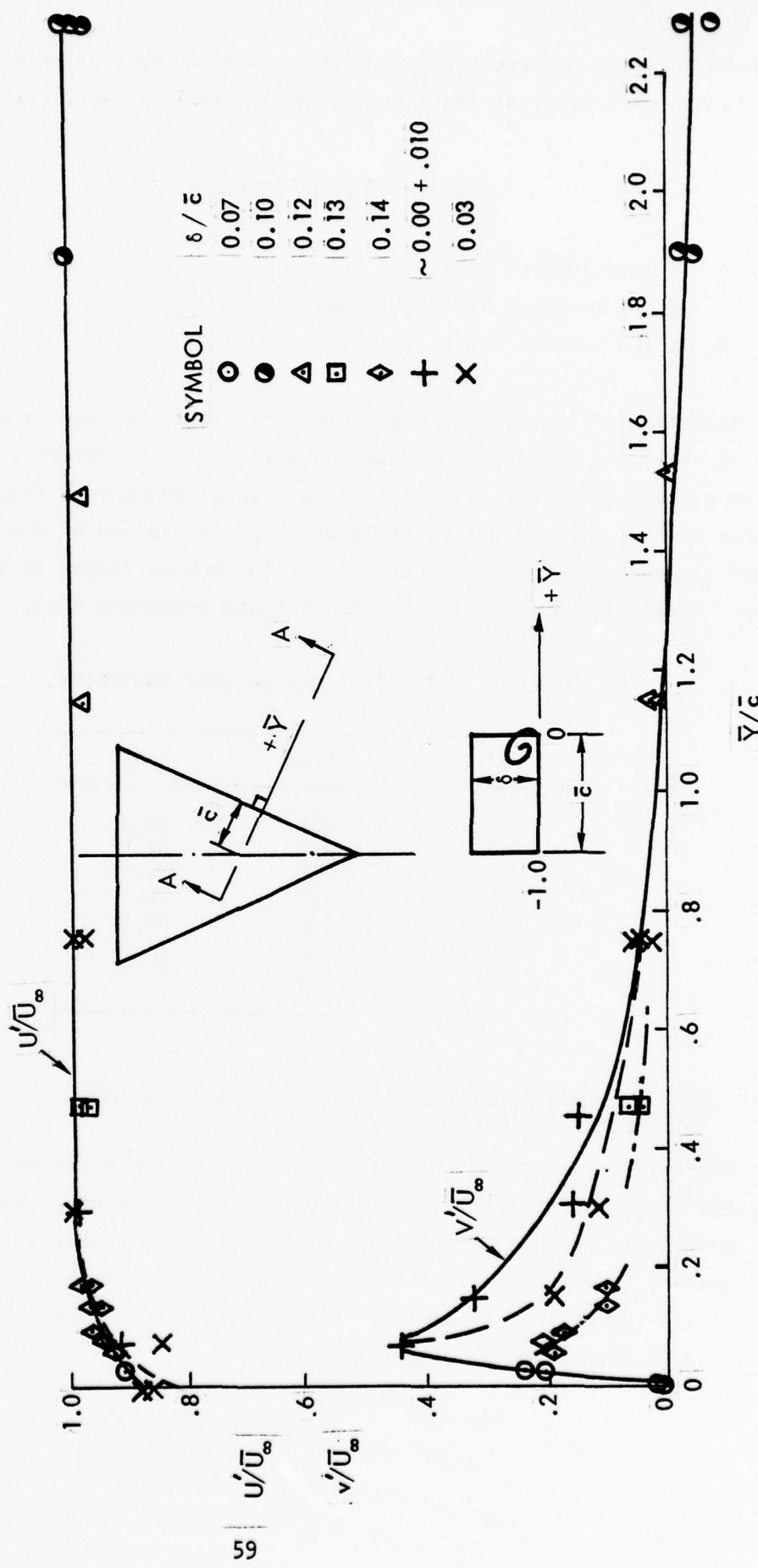


Figure 35 Velocities on Line Normal to Wing L.E. $\alpha = 22^\circ$

has been drawn to represent crossing the boundary layer. The slope of this line is the vorticity, at least the major component of vorticity.

$$\therefore \xi \left(\frac{c}{U_\infty} \right) \approx \partial(v/U_\infty)/\partial(n/c) \approx 70 \quad (19)$$

where c is the width of box 2,

n is the boundary layer thickness,

v is the vertical velocity.

Variation of the leading edge vorticity along the leading edge of the wing is estimated from the logic that the vorticity is directly proportional to the circulation growth at the leading edge as determined from vortex lattice method. The values of the growth in circulation of the leading edge vortex element are given as a function of the box positions in the following table. Proportioned vorticity values of ξ are presented also.

TABLE 1 ESTIMATED LEADING EDGE VORTICITY

X/C_R	$\Delta\Gamma/U_\infty$	ξ/U_∞
.2	.486	50.9
.3	.438	45.5
.382	.358	37.1
.5	.252	26.1
.578	.195	20.3
.75	.160	16.6
.878	.180	18.7

3.8.2 Resulting Vorticity Box Circulation, Velocity, and Vorticity Distribution

Figures 36 through 38 shows the vorticity contours and velocity vectors as computed by the vorticity box method for the aft faces of boxes 1 through 3. The results are not satisfactory at this time, but they do indicate what is necessary to make them satisfactory. Boxes 4, 5, and 6 results are not instructive and are not presented. Difficulties and changes required are presented in the following discussion.

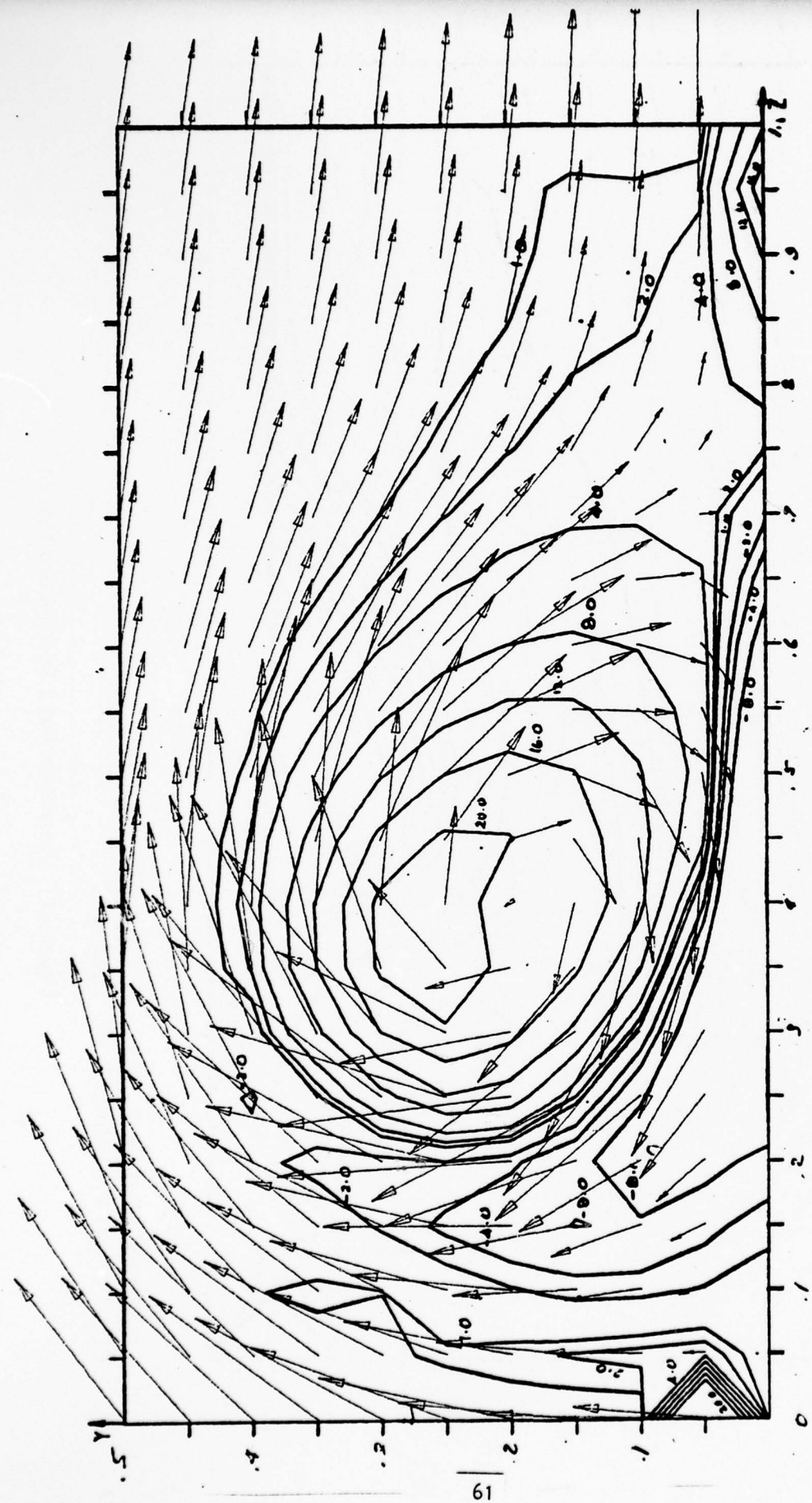
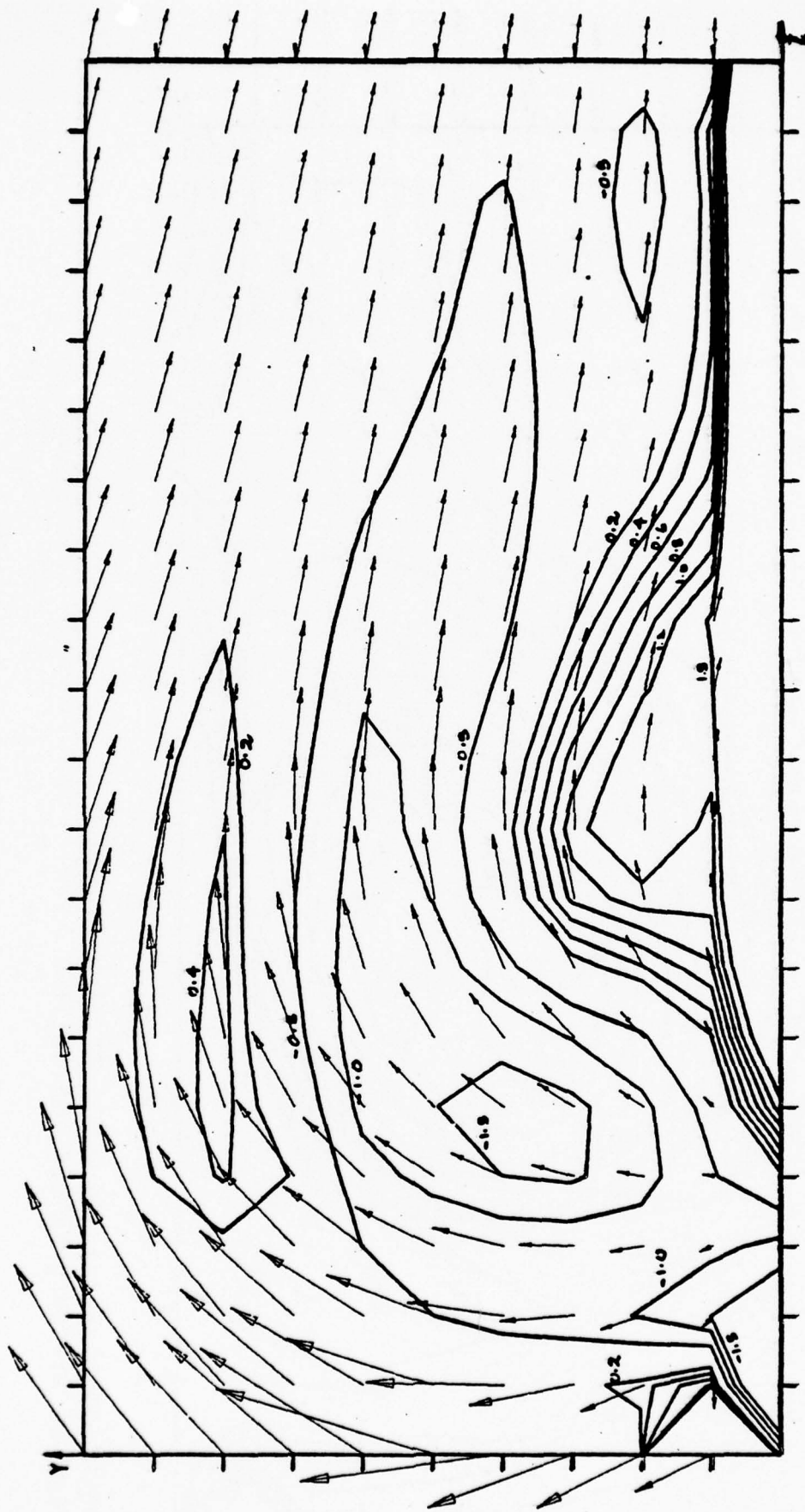
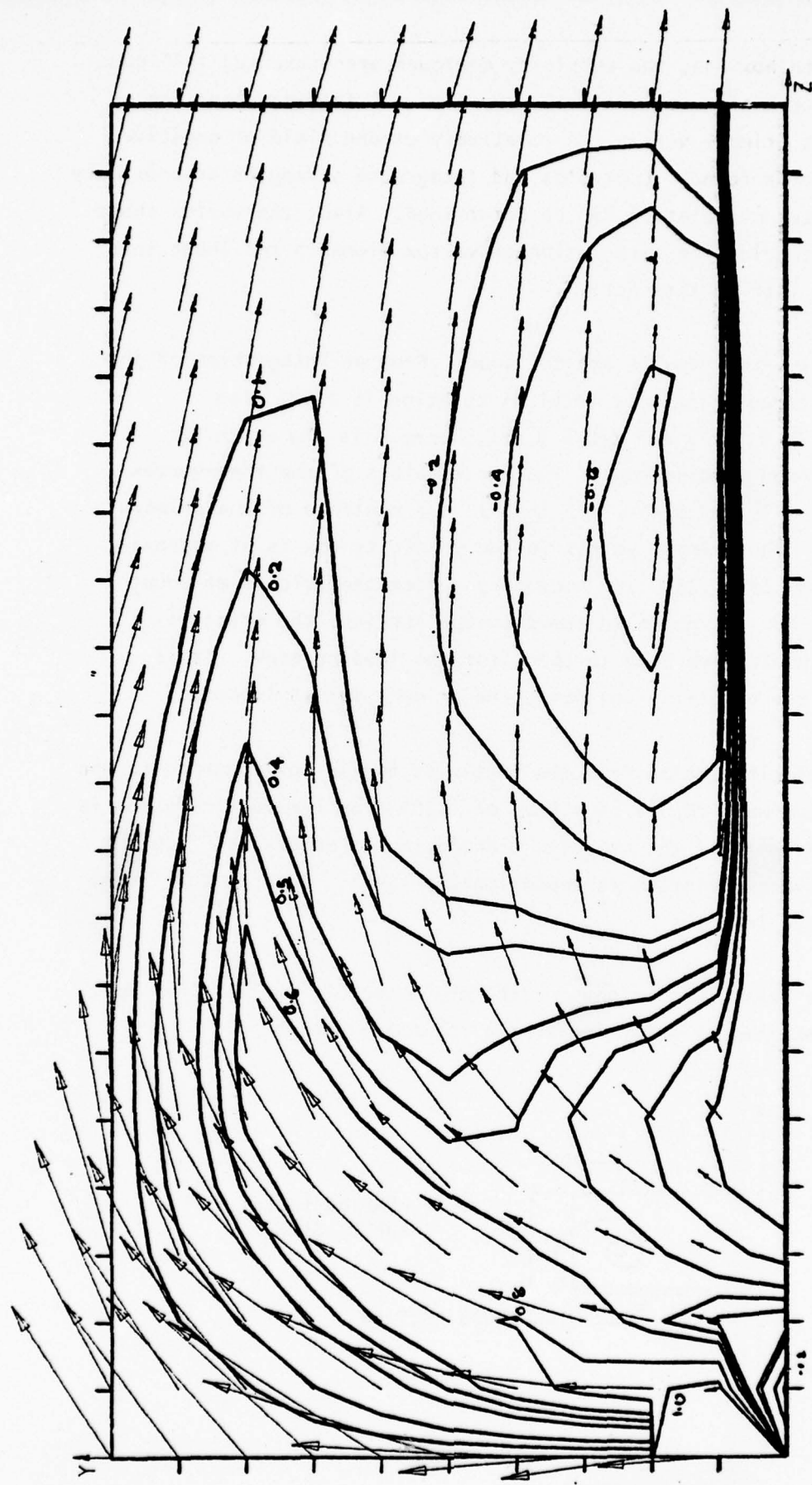


Figure 36 Downstream Box 1 Contours and Velocities



SOLUTION AT $X = 2.005$
 $\partial Y / \partial Z = 0.0770$
 PLOT OF X_1 -COMPONENT OF VORTICITY.

Figure 37 Downstream Box 2 Contours and Velocities



SOLUTION AT $X = 3.307$ $\partial Y / \partial Z = 0.0983$
 PLOT OF ξ_1 -COMPONENT OF VORTICITY.

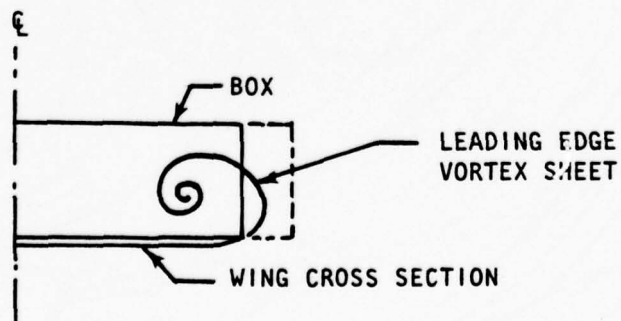
Figure 38 Downstream Box 3 Contours and Velocities

Beginning with box one, the vorticity contours are presented in Figure 36. The results here are qualitatively very good. A feeding sheet can be noted as well as a primary vortex. A relatively strong field of negative vorticity can also be found. Centroids and integrated strengths of a primary and secondary vortex circulation can be determined. Also, the vortex sheet can be divided into discrete circulation of vortex elements for input into the second vortex lattice interaction.

Quantitatively, the results are not good. From an integration of the vorticity to get circulation, the total circulation is 1.202 with the centroid at $Y/C = 0.275$ and $Z/C = 0.551$, where c is the width of the box and Y is from leading edge. The input values of the free-vortex centroid were $Y/C = .34$ and $Z/C = .30$. This is the centroid of the primary circulation only. The primary vortex in the vorticity box is at approximately $Y/C = .42$ and $Z/C = .23$. The secondary vortex centroid is at about $Y/C = .2$ and $Z/C = .08$. As noted in the previous section, the original estimate of Y/C should have been further from the leading edge. It is encouraging that the vorticity box moves the primary vortex inboard.

The amount of circulation from the vorticity box is low compared to the initial input which was $\Gamma/U_\infty = 4.85$. Γ/U_∞ of 1.202 from the vorticity box is the total circulation. If the negative circulation is subtracted from the total, the positive circulation is approximately 1.488. This is still very low compared to the input.

There are at least two reasons for the above anomaly. First, and most important, is described by referring to the following sketch.



The vorticity box used has its vertical edge at the leading edge; however, the vorticity contours of the computed results indicate the vortex sheet is forced to have a reverse curve, not as the sketch shows it. The velocity vectors on the vertical edge of the box, figure 36, show very little inflow into the box; therefore, very little of the input vorticity, at the first vertical mesh point, is fed into the box. The remedy for this is to extend the box ahead of the leading edge as shown by the dotted lines in the sketch. Now, the input leading edge vorticity will be put on the bottom of the box just ahead of the leading edge. The strong vertical components of velocity there will feed the vorticity into the box, and the correct shape of the vortex sheet should be made. This proposed correction to the box boundaries is not available at this time. It will probably not be necessary for the thick rounded leading edges since the boundary layer turns over the airfoil before separating except at very high angles of attack.

The second reason for losing vorticity may be due to the relatively large mesh used for these trial investigations. The effect of numerical accuracy cannot be determined until the problem above is explored.

Vorticity contours and velocity vectors for boxes two and three are shown in Figures 37 and 38. These suffer even worse than box one because of the same reasons as well as the fact that each are dependent on the preceding box results. In order to check our theory that vorticity is not being fed into the boxes, the leading edge input vorticity for box two was moved to a position where strong inflow is occurring on the leading edge, i.e. at vertical grid positions 6 and 7. This indeed shows a large increase in circulation, about three times. Figure 39 shows the vorticity and velocity vectors for this case.

It was decided that another check was necessary. Vorticity entering a box at its face must travel downstream on the order of 3 or 4 box widths before entering the primary vortex core. Results of Figure 39 are for a downstream distance of less than one box width; so this case was run again keeping all boundary conditions the same while stepping further down the box. The results do indicate a rolling up of vorticity into primary vortex.

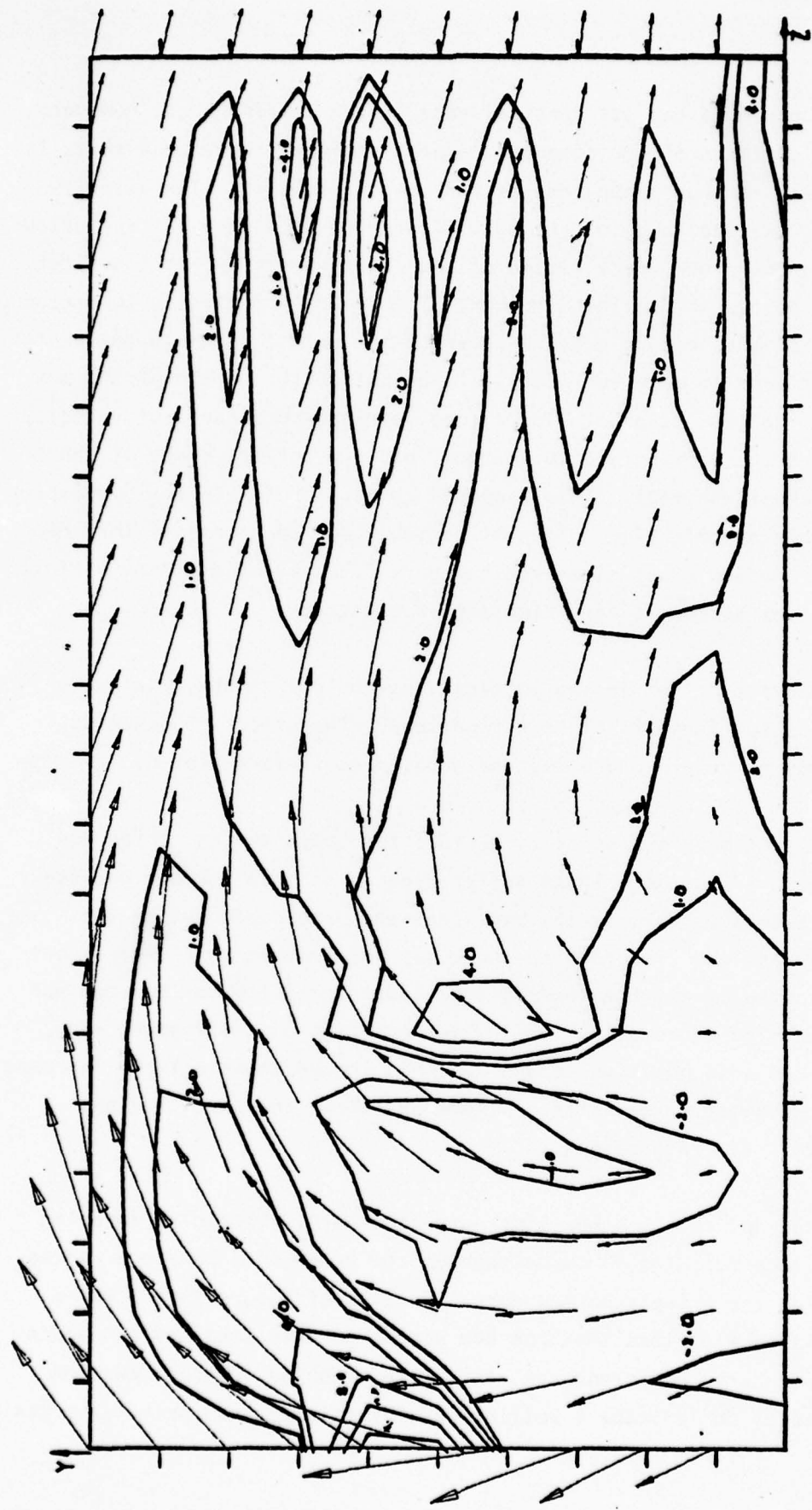


Figure 39 Downstream Box 2 Contours and Velocities
 with Leading Edge Vorticity Shifted Vertically

The use of rectangular boxes leads to difficulty in sustaining a smooth numerical computation of the flow. In fact, the present demonstration indicates a breakdown of the vortex flow pattern following transition to a larger box, and the requirement of solution interpolation, as discussed in Section 3.5, appears to be a major cause of this behavior. As noted earlier, curvilinear coordinate system is needed for the viscous computation in order to take account of vortex growth. A spherical system would probably be required, in which case terms involving two curvatures would be added to the governing equations. Such a curvilinear mesh could also be extended forward of the leading edge, as depicted in Figure 40. Thus, a system possessing two curvatures would increase in physical dimension with downstream distance while retaining a fixed number of mesh points, and, most importantly, no discontinuities would be encountered in the stepping direction.

3.8.3 Pressures from Vorticity Box

The most realistic results to date have been obtained from box one of the thin delta wing investigation. It is believed the pressure calculation technique as described in Section 2.5 is satisfactory (at least for the fine grid solutions). Results from box one are presented in Figure 41. Absolute values are not correct, but the shape is typical of delta wing pressure distribution except at the leading edge. Better definition of leading edge input conditions should improve the leading edge pressures.

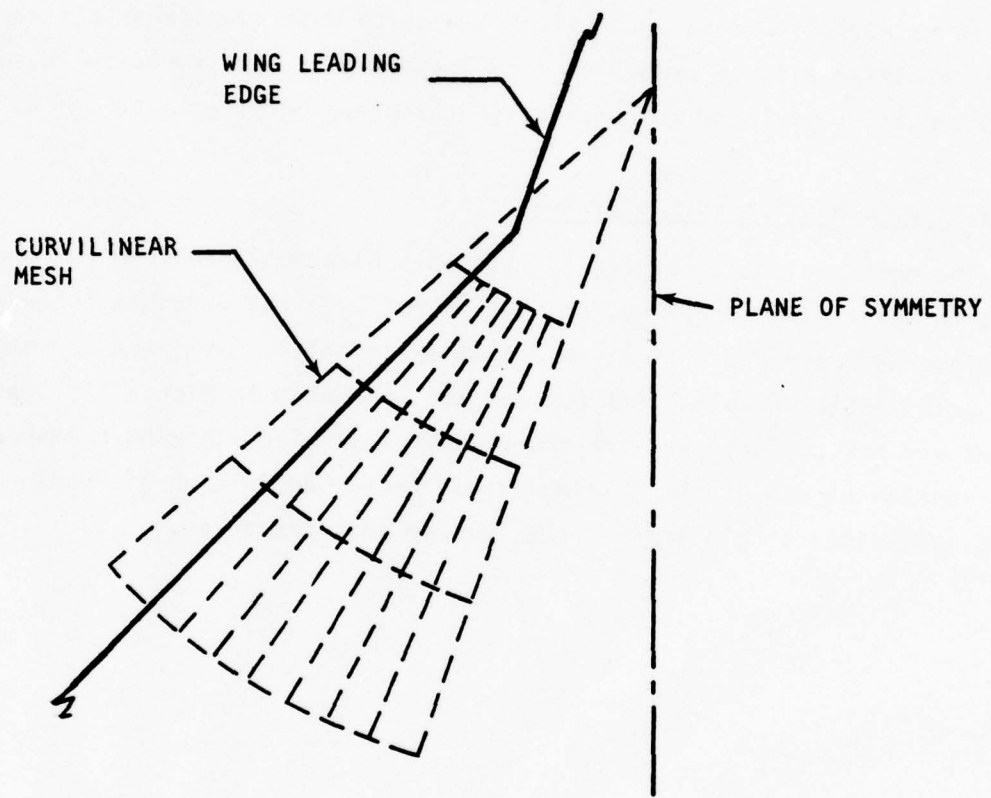


Figure 40 Proposed Curvilinear Mesh

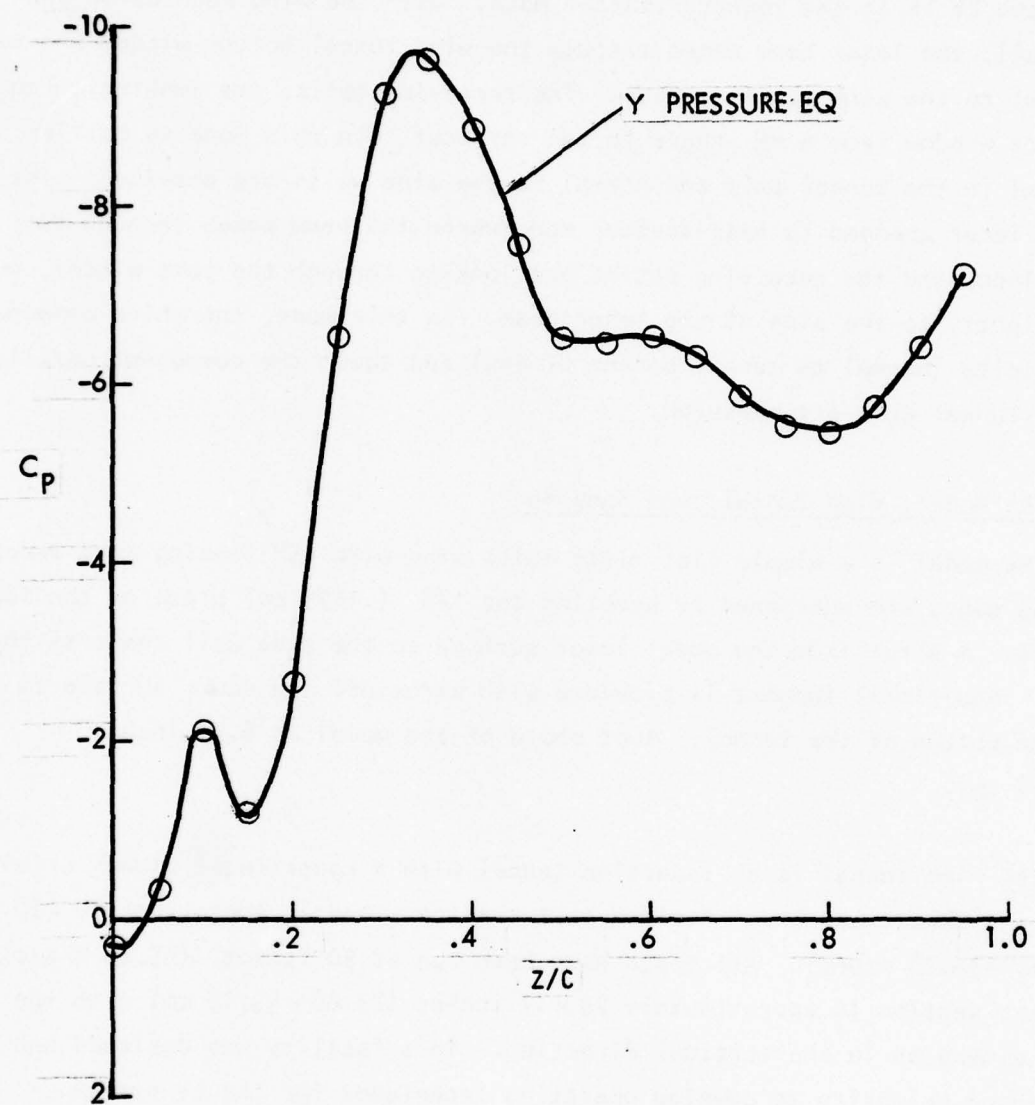


Figure 41 Pressure Distribution at Wall of Box 1

4. LASER VELOCIMETER EXPERIMENTS

4.1 General Description

Laser velocimeter, LV, experiments were conducted, primarily to determine the velocity vectors for the boundary conditions at the face of one of the boxes. The delta wing and LV optics are shown in Figure 42. In this photograph the LV is in the forward-scatter mode. With the wing mounted on the side wall, the laser beam comes through the wind tunnel bottom window and runs parallel to the wing upper surface. The receiving optics are looking through the side window from a 45° angle to the vertical. In this mode velocities parallel to the tunnel axis and normal to the side walls are obtained. The LV was later changed to back-scatter mode where the beam comes through the side window and the receiving optics are looking through the same window, but off slightly to the side of the laser beam. In this mode, the third component of velocity (normal to tunnel bottom window) and again the component parallel to the tunnel axis are measured.

4.2 The Model, Wind Tunnel, and Seeding

The model is a simple flat plate delta wing with 65° leading edge sweep. Leading edges are sharpened by beveling the 1/8" (.3175 cm) plate on the lower surface. A strut from the model lower surface to the side wall supports the model. Additional support is provided with wires off the lower surface to the top and bottom of the tunnel. Root chord of the model is 8.57 inches (21.768 cm).

The wind tunnel is an induction tunnel with a centrifugal blower driving it at its downstream end. Maximum test section speed is approximately 120 ft/sec. (36.58 m/sec). All tests have been run at 50 ft/sec. (15.24 m/sec). The test section is approximately 29 × 17 inches (73.66 × 43.18 cm) with the large dimension in the vertical direction. This facility was designed and fabricated primarily to develop operating techniques for the LV system.

One of the systems under study is the method of seeding the tunnel. In this case a Sommenist ultra-sonic atomizing nozzle is used upstream in the contraction section of the tunnel. Water seemed to give good seeding rates



Figure 42 Laser Velocimeter Optics and Delta Wing Mounted in LV Induction Wind Tunnel

and it was used as the seeding material. Particle size has not yet been determined. This will be done once the purchased particle analyzer arrives.

4.3 Results of Delta Wing Test

Boundary conditions were desired at one box to obtain typical input conditions for the viscous vorticity box. Specifically, it was desired to measure the edge velocities on the box face and velocities on a line normal to the leading edge in the plane of the upper surface of the delta wing and extending from the leading edge out to free-stream conditions. Since the box face is normal to the leading edge, the single line ahead of the wing is also in the plane of the box face.

The face of box 2 is chosen for the LV analysis. A sketch of the model and results of the velocities measured along the extended line are given in Figure 35. It was very difficult to measure exactly on a line in the plane of the wing upper surface; therefore, the velocities are given for several heights. As a first approximation, results from the vertical velocity distribution across the boundary layer at $\delta/c = .07$ provides an estimate of the leading edge vorticity; i.e.

$$\xi(\bar{c}/U_\infty) = \partial(v/U_\infty)/\partial(Y/\bar{c}) = 70 \quad (20)$$

where \bar{c} is the width of the box face (leading edge to plane of symmetry). (Note, for investigations presented in Section 2.0, the reference chord is $.5 \bar{c}$; therefore, $\xi/U_\infty = 35$). Values of U and V are based on tunnel wind axis coordinates, and it would be slightly more correct to convert to model box coordinates; i.e. U , V , W which are calculated from U' , V' , W' by equation (15) of Section 3.5. The data of Figure 35 have not been converted partly because the W component is not available and partly because the U component in the edge boundary layer could not be measured at $\delta/\bar{c} = 0$.

The next objective was to measure the boundary conditions around the face of box 2. This has been done twice. The first time only the U' and V' velocity components in the tunnel coordinate system were measured. The W' component was measured at a later date with the LV in the backscatter mode.

In the first test the model support and the tunnel seeding methods were different than when the backscatter was done on the second test. It was felt the support and seeding was much better in the second test; so forward scatter (U' and V' components) were measured again.

During the forward-scatter measurements of the second test, it proved to be more accurate and faster to take data in planes normal to the tunnel axis. This is faster data acquisition, but causes much more analyses. Three planes of data grouped in the area of the box coordinate plane were taken and then cross plots are made to get all data in the box coordinate system plane. (The box coordinate system plane is normal to the wing surface and wing leading edge.) Both forward and back-scatter data were taken, i.e. U' , V' , and W' components, and enough data has been taken to map the flow-field vectors over most of the box face. Only the edge velocities are obtained at this time due to time-consuming data analyses. These are shown in Figure 43 with the vectors rotated to box coordinates. Figures 27 and 28 show the measured vectors in the wind axis system comparing with the results from the vortex lattice. The latter show the initial assumed vortex location is too close to the surface and the wing leading edge. The experimental velocities along the leading edge of the box also indicate the vortex feeding shed crosses at about $0.25 Y/c$ as is also shown in Figure 43.

Figure 43 also shows the effective vortex center as obtained from LV data by finding the intersection of the lines for zero spanwise and vertical velocity. A further observation of the LV data indicates the vortex core extends beyond the upper bounds of the assumed box. This of course violates the theory and will have to be corrected on subsequent efforts.

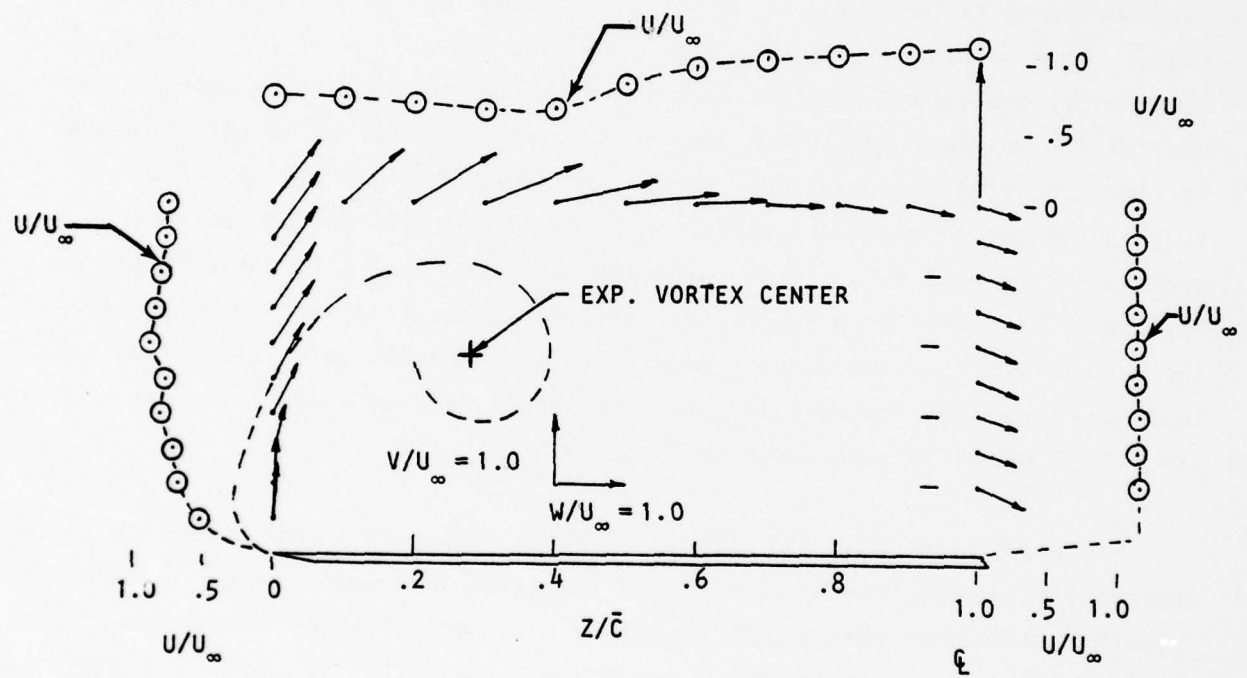


Figure 43 Experimental Edge Velocities (Vectors) at Box 2
(Rotated to Box Coordinates)

5. CONCLUSIONS

1. The computational viscous flow model has been developed to provide a qualitatively valid solution to the vortex/wing interaction problem.
2. It is shown how the viscous method can be combined with a potential flow model in an iterative technique to produce the flow field for a delta wing at high angle of attack. Some difficulties in getting the appropriate boundary and starting conditions are apparent, but none discredit the feasibility of the technique.
3. Accuracy of the viscous box method appears satisfactory, but as of now there is no exact solution to compare with. The only proof will appear when results of a converged solution for a finite wing are compared with accurate experimental data.

6. RECOMMENDATIONS FOR FURTHER EFFORT

There are some additional efforts already planned towards the fruition of this program. These are: (1) Provide a leading edge boundary layer program to compute the input vorticity and boundary layer velocities in order to make the program applicable to thick leading edge configurations, (2) interface the boundary layer and viscous box theory with a thick wing potential flow theory, and (3) include the secondary vortex in the potential flow theory.

There are further efforts not yet in the planning stage that should be accomplished soon. Among these are: (1) change coordinate system to spherical to eliminate stepping the box size, (2) modify program to allow the viscous box to extend beyond the leading edge to improve the thin wing calculations and to eliminate high angle of attack limitations on the thick wing problem.

Future efforts should include: (1) the complete integration into one program, all of the related viscous and potential flow models described above, (2) the method should be applied to wings other than deltas and to other related viscous problems such as "Upper Surface Blowing," Spanwise Blowing, and Afterbody Drag, (3) a turbulence model should be integrated into the viscous model, and (4) the viscous box model should also be extended to include two sides with no-slip flow.

REFERENCES

1. Thomas K. Matoi: On the Development of a Unified Theory for Vortex Flow Phenomena for Aeronautical Applications," Massachusetts Institute of Technology Report, 1 November 1973 - 31 October 1974, for Office of Naval Research, April 14, 1975.
2. K. W. Mangler and J. H. B. Smith: Calculation of the Flow Past Slender Delta Wings With Leading Edge Separation," RAE Rep. Aero. 2593, May 1957.
3. E. C. Polhamus: A Concept of Vortex Lift of Sharp-Edge Delta Wings Based on a Leading Edge Suction Analogy, NASA TN C-3736, 1966.
4. James A. Weber, W. B. Guenter, J. J. Forrester, Paul Lu, and Paul E. Rubbert: A Three-Dimensional Solution of Flows Over Wings With Leading Edge Vortex Separation, AIAA Paper 75-866, June 1975.
5. B. M. Rao, and J. K. Nathman: Analytical and Experimental Investigations of Delta Wings in Compressible Flow, Texas A&M University Report TEES-3167-76-01, May 1976.
6. O. A. Kandil, D. F. Mook, and A. H. Nayfeh: New Convergence Criteria for the Vortex-Lattice Models of the Leading Edge Separation, *Vortex-Lattice Workshop*, NASA SP-405, May 1976
7. R. M. Scruggs, C. J. Dixon: Theoretical and Experimental Investigations of a Jet Parallel to Wing in Cross Flow, Final Report, Office Of Naval Research Contract, Lockheed-Georgia Engineering Report LG75ER-0028, April 1975.
8. R. M. Scruggs and C. J. Dixon: Vortex/Jet/Wing Viscous Interaction Theory and Analysis, Office of Naval Research Report ONR-CR215-233-2, February 2, 1976.
9. D. J. Marsden, R. W. Simpson, and B. E. Rainbird: An Investigation into the Flow Over Delta Wings at Low Speeds with Leading Edge Separation, The College of Aeronautics, Cranfield, Report No. 114, February 1958.
10. D. H. Peckham: Low-Speed Wind Tunnel Tests on a Series of Uncambered Slender Pointed Wings with Sharp Edges, R&M No. 3186, Brit. ARC, 1961.
11. J. H. B. Smith: Improved Calculations of Leading Edge Separation from Slender, Thin, Delta Wings, Proc. Roy. Soc., London, Ser. A, 306, pp. 67-90, 1968.
12. W. P. Henderson: Effects of Wing Leading Edge Radius and Reynolds Number on Longitudinal Aerodynamic Characteristics of Highly Swept Wing-Body Configurations at Subsonic Speeds, Langley Research Center, NASA TN D-8361, December 31, 1976.
13. J. F. Nash and R. R. Tseng: The Three-Dimensional Turbulent Boundary Layer on an Infinite Yawed Wing, *Aeronautical Quarterly*, 1971.

14. J. C. Wu: Velocity and Extraneous Boundary Conditions of Viscous Flow Problems, AIAA Paper 75-47, AIAA 13th Aerospace Sciences Meeting, January 1975.

LIST OF SYMBOLS

AR	aspect ratio
\mathbf{F}	column vector of vorticity components
H	total pressure function
u, v, w	velocities in the x, y, z directions, respectively
$\bar{u}, \bar{v}, \bar{w}$	mean velocities in the x, y, z directions, respectively
u', v', w'	wind tunnel velocities in the x, y, z directions, respectively
\bar{c}	box chord, normal to leading edge
C_R	wing root chord
S	wing span, normal to plane of symmetry
C_{ℓ_v}	lift coefficient, vortex lift
C_p	pressure coefficient
x, y, z	streamwise, vertical, and spanwise coordinates
ξ, η, ζ	vorticity in x, y, z directions, respectively
α	angle of attack of wing
Γ	circulation
γ	included angle between wing leading edge and C_L
δ	distance normal to wing surface and leading edge
	boundary layer thickness
ν	kinematic viscosity
ρ	density of flow in wind tunnel
$\bar{\omega}$	vorticity vector
$(\overline{})$	denotes vector unless otherwise noted
Λ	wing leading edge sweep

APPENDIX

VORTICITY BOX PROGRAM DOCUMENTATION
AND TYPICAL OUTPUT

VORTICITY BOX PROGRAM - DOCUMENTATION

CONTENTS

<u>Section</u>		<u>Page</u>
A	General Comments on the Capabilities to the Program	82
B	References	82
C	Computational Sequence	83
D	Input Details	84
E	Definition of Key Fortran Variables	86
F	Tape or Mass Storage File Requirement	86
G	Table of Subroutines and Their Purpose	87

A. General Comments on the Capabilities of the Program

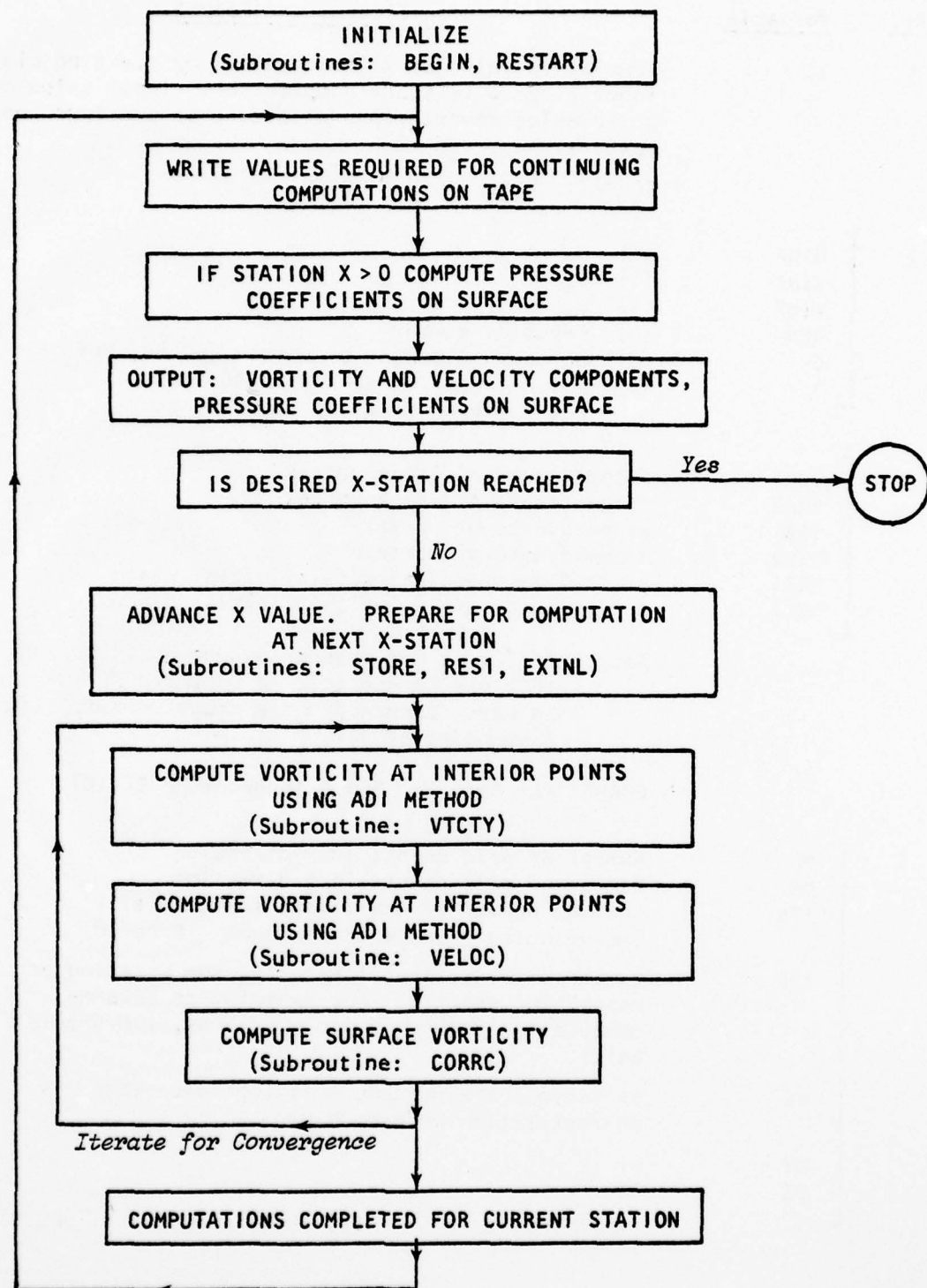
The program solves approximated steady-state Navier-Stokes equations using finite differences. Vorticity and velocity vectors are employed as dependent variables. The vorticity transport equation is parabolized in one of the coordinate directions by assuming diffusion to be negligible in this direction. This direction is labelled as X in the programs coding. With initial values of vorticity and velocity specified at $x = 0$ plane, the solutions are obtained by marching forward in the X-direction. The domain of integration is box-shaped and one face of the box ($y = 0$ plane in program coding) has no-slip boundary conditions applied on it. On the other faces of the box vorticity is specified as zero. The box size must be sufficiently large to meet this condition. The velocity values on the edges of the box are computed using Green's function technique. Alternatively, these values can be specified, for example, using potential flow solutions. The program is capable of numerically simulating vortex-type flows near no-slip wall and flows with wall jet interaction.

Discussions on the formulation of governing equations and the finite difference equations used in the computations will be found in References 1 and 2. In the following sections details that a user should know for running case studies with this program are presented.

B. References

1. R. M. Scruggs and C. J. Dixon, "Vortex/Jet Wing Viscous Interaction Theory and Analysis," Report No. LG76ER0007, Lockheed-Georgia Company, Feb., 1976.
2. C. J. Dixon and R. M. Scruggs, "Further Development of a Viscous Vortex/Wing Interaction Program," Interim Report to Office of Naval Research, Contract N00014-74-C-0151, NR215-233.

C. Computational Sequence



D. Input Details

<u>Card</u>	<u>Nr.</u>	<u>Variable</u>	<u>Significance and Format</u>														
1		XC	Cumulative value of x from initial or starting plane. Input as zero to start computation. Input value of x up to which computations were done on previous sum to restart. FORMAT: Free (MAIN Program)														
2		<table border="1"> <tr><td>UINF</td><td>(1) u_{∞}</td></tr> <tr><td>VINF</td><td>(2) v_{∞}</td></tr> <tr><td>WINF</td><td>(3) w_{∞}</td></tr> <tr><td>REN</td><td>(4) Reynolds number</td></tr> <tr><td>C_1</td><td>(5) a_v, core diameter of vortex (p. 46, Ref. 1)</td></tr> <tr><td>A</td><td>(6) a_j, defines jet shape (p. 46, Ref. 1) Set to zero if no jet is present.</td></tr> </table>	UINF	(1) u_{∞}	VINF	(2) v_{∞}	WINF	(3) w_{∞}	REN	(4) Reynolds number	C_1	(5) a_v , core diameter of vortex (p. 46, Ref. 1)	A	(6) a_j , defines jet shape (p. 46, Ref. 1) Set to zero if no jet is present.			
UINF	(1) u_{∞}																
VINF	(2) v_{∞}																
WINF	(3) w_{∞}																
REN	(4) Reynolds number																
C_1	(5) a_v , core diameter of vortex (p. 46, Ref. 1)																
A	(6) a_j , defines jet shape (p. 46, Ref. 1) Set to zero if no jet is present.																
3		<table border="1"> <tr><td>YZA1</td><td>y-coordinate of image vortex</td></tr> <tr><td>YZA2</td><td>z-coordinate of image vortex</td></tr> <tr><td>YZB1</td><td>y-coordinate of vortex</td></tr> <tr><td>YZB2</td><td>z-coordinate of vortex</td></tr> <tr><td>YZC1</td><td>y-coordinate of jet axis in initial plane</td></tr> <tr><td>YZC2</td><td>z-coordinate of jet axis in initial plane.</td></tr> </table>	YZA1	y-coordinate of image vortex	YZA2	z-coordinate of image vortex	YZB1	y-coordinate of vortex	YZB2	z-coordinate of vortex	YZC1	y-coordinate of jet axis in initial plane	YZC2	z-coordinate of jet axis in initial plane.	<i>Note: If jet is not present, values given to YZC1 and YZC2 are immaterial. A variable EPA when set to zero 'turns-off' the image vortex. (Line 68, Subroutine BEGIN.)</i>		
YZA1	y-coordinate of image vortex																
YZA2	z-coordinate of image vortex																
YZB1	y-coordinate of vortex																
YZB2	z-coordinate of vortex																
YZC1	y-coordinate of jet axis in initial plane																
YZC2	z-coordinate of jet axis in initial plane.																
			FORMAT for Card 3: 8F8.0 (Subroutine BEGIN).														
4		<table border="1"> <tr><td>MM</td><td>Number of grid points in y-direction.</td></tr> <tr><td>NN</td><td>Number of grid points in z-direction.</td></tr> <tr><td>ITN</td><td>Maximum number of iterations for vorticity and velocity (Recommended value: 10 to 20)</td></tr> <tr><td>IXN</td><td>Number of x-stations (including the starting or restarting station. For example, to advance computation from $x = x_1$ to $x = x_1 + \Delta x$, IXN should be 2).</td></tr> <tr><td>DX</td><td>Δx. Since the procedure is implicit, there is no restriction on step size.</td></tr> <tr><td>DY</td><td>Δy</td></tr> <tr><td>DZ</td><td>Δz</td></tr> </table>	MM	Number of grid points in y-direction.	NN	Number of grid points in z-direction.	ITN	Maximum number of iterations for vorticity and velocity (Recommended value: 10 to 20)	IXN	Number of x-stations (including the starting or restarting station. For example, to advance computation from $x = x_1$ to $x = x_1 + \Delta x$, IXN should be 2).	DX	Δx . Since the procedure is implicit, there is no restriction on step size.	DY	Δy	DZ	Δz	FORMAT for Card 4: 413, E8.2, 2F8.0 (Sub. BEGIN).
MM	Number of grid points in y-direction.																
NN	Number of grid points in z-direction.																
ITN	Maximum number of iterations for vorticity and velocity (Recommended value: 10 to 20)																
IXN	Number of x-stations (including the starting or restarting station. For example, to advance computation from $x = x_1$ to $x = x_1 + \Delta x$, IXN should be 2).																
DX	Δx . Since the procedure is implicit, there is no restriction on step size.																
DY	Δy																
DZ	Δz																

<u>Card Nr.</u>	<u>Variable</u>	<u>Significance and Format</u>				
5	<table border="0"> <tr> <td>DYP</td> <td>$\Delta y'$. New value of Δy when box size changes. (See Fig. 19, Ref. 2).</td> </tr> <tr> <td>DZP</td> <td>$\Delta z'$. New value of z when box size changes.</td> </tr> </table>	DYP	$\Delta y'$. New value of Δy when box size changes. (See Fig. 19, Ref. 2).	DZP	$\Delta z'$. New value of z when box size changes.	FORMAT for Card 5: 10F8.0 (Subroutine RESTART)
DYP	$\Delta y'$. New value of Δy when box size changes. (See Fig. 19, Ref. 2).					
DZP	$\Delta z'$. New value of z when box size changes.					

6 VORTLE Leading edge value of vorticity component ξ .
FORMAT: F8.0 (Subroutine RESTART).

7 Potential flow velocity values, punched in the following sequence.

Component u_p

$u_{P2,NN}$ $u_{P3,NN}$ $u_{PMM,NN}$

$u_{P2,NN-1}$ $u_{P3,NN-1}$ $u_{PMM,NN-1}$

⋮
⋮
⋮

$u_{P2,1}$ $u_{P3,1}$ $u_{PMM,1}$

Component v_p

(Sequence as above)

Component w_p

(Sequence as above)

FORMAT: 10F8.0 (lines 18 + 22, Subroutine RESTART).

E. Definition of key FORTRAN VARIABLES

ALPH Angle of attack, α in degrees (defined in line 14 of subroutine RESTART).

SLAM Sweep angle, λ in degrees (defined in line 15 of subroutine RESTART).

ICON {
 = 1 Continuity equation will be used to compute and over-write u-component of velocity.
 = 0 Continuity equation will not be used.
(Lines 11, 12 MAIN. Recommended value zero.)

IMAP {
 = 1 Green's function will be used to compute boundary velocity.
 = 0 Green's function will not be used.

Note: If Green's function is to be used, the calling sequences to subroutines must additionally be changed, to suppress input of potential flow velocity values. See MAIN program in listing.

CP(M,N) Pressure coefficient at m,n.

F(M,N,I) Components of vorticity vector at current x-station.

F0(M,N,I) Vorticity components at previous x-station.

FP(M,N,I) Vorticity components at current x-station corresponding to previous iteration.

FA(M,N,I) Alternate solution of vorticity obtained using $w=0$ on the wall. Used in determining surface vorticity.

V, VO, VP Velocity - with meanings similar to F, F0, and FP.

VA(M,N,I) Velocity values corresponding to FA.

YZ(M,K) y and z values of modal points.

F. Tape or Mass Storage File Requirement

One tape or mass storage file with a designated name TAPE10 is required. Value of XC, DY, DZ, V and F are written on this file. These values are used for restarting the computations and for usage subsequent machine plotting.

G. Table of Subroutines and Their Purpose

<u>Subroutine Name</u>	<u>Purpose</u>	<u>Other Subroutines Used</u>
1. BEGIN	Read in key parameters - Initialize vorticity and velocity fields.	None
ENTRY-EXTNL	Advance x-station and re-initialize.	None
2. CONTN	Compute surface vorticity.	None
3. CORRC	Compute surface vorticity.	None
4. EQTNS	Form coefficients in finite difference equations. That is, matrices [A], [B], [C], [D] of Eq. (8), Ref. 1.	None
5. GUESS	Make an initial guess for velocity and vorticity. (Not used).	None
6. INVRT	Invest a 3×3 matrix. Augmented: A Matrix to be inverted B Inverse IE Test parameter which returns a value of zero if determinant of matrix is less than 10^{-15} .	None
7. OUTPT	Prints out computed results.	None
8. SOLVE	Inverted tri-diagonal block matrix using Cholesky's method.	INVRT, MULTY
9. MULTY	Multiplies two matrices (3×3).	None
10. STORE	Sets $V0 = V$ and $F0 = F$ before advancing x-station.	None
<u>ENTRY-STORE2</u>	Sets $VP = V$ and $FP = F$ before advancing iteration.	
11. VELOC	Computer velocity values at interior points using ADI method.	SOLVE
12. VTCTY	Computes vorticity values at interior points using ADI method.	EQTNS MULTY SOLVE

<u>Subroutine Name</u>	<u>Purpose</u>	<u>Other Subroutines Used</u>
13. DVEL	Computes velocity on boundaries using Green's function.	None
14. CPDIS	Computes pressure distribution (Page 11-12, Ref. 2).	None
15. RESTART	Reads potential flow velocities and converts them into box coordinates. Interpolates field values when box size changes.	
<u>ENTRY-RES1</u>	Reads potential flow velocities when there are intermediate stations within same box.	
<u>ENTRY-SHIFT</u>	Writes on TAPE10 the values of XC, DY, DZ, F and V.	

AD-A046 342

LOCKHEED-GEORGIA CO MARIETTA
FURTHER DEVELOPMENT OF A VISCOUS VORTEX/WING INTERACTION PROGRAM--ETC(U)
JUN 77 C J DIXON, R M SCRUGGS
L677ER0209

F/G 20/4

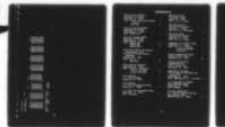
N00014-74-C-0151

ONR-CR215-233-3

NL

UNCLASSIFIED

2
AD
A046342



END
DATE
FILED
12-77
DDC

42

SOLUTION OUTPUT
 $x = 1.000$ $z = 1.500$
 VELOCITY PROFILES

y	x_1	η	ζ	u	v	w	cp
.1000E-05	-.6710E-01	0.	-.6751E+01	.4185E-05	-.4258E-06	-.3198E-08	-.4702E+00
.1000E+00	-.1173E+00	.4061E+00	.6028E+00	.4805E+00	-.2590E-01	.9851E-02	-.6715E+00
.2000E+00	-.1277E+01	.4009E+01	.1038E+01	.5710E+00	-.3518E-01	.5202E-01	-.8918E+00
.3000E+00	-.1699E+01	.5939E+00	.9641E+00	.6240E+00	-.1625E-01	.7608E-01	-.1070E+01
.4000E+00	-.1654E+01	.8063E+00	.7764E+00	.6127E+00	-.1753E-01	.7371E-01	-.1276E+01
.5000E+00	-.1722E+00	.1187E+01	.3613E+00	.6890E+00	-.9019E-01	.7017E-01	-.1402E+01
.6000E+00	-.3133E-01	.1069E+01	.1042E+01	.7562E+00	-.2195E+00	.1645E+00	-.1550E+01
.7000E+00	-.4398E+01	.1114E+01	.6619E+00	.6614E+00	-.2701E+00	.4056E+00	-.1376E+01
.8000E+00	-.4216E+01	.9650E+00	.1326E+01	.9200E+00	-.2866E+00	.6586E+00	-.1282E+01
.9000E+00	-.2337E+01	.4324E+00	.9116E+00	.9551E+00	-.2299E+00	.6175E+00	-.5024E+00
.1000E+01	-.7219E-33	0.	0.	.68682E+00	-.9933E-01	.3015E+00	-.1810E+00

WALL SHEAR STRESS COMPONENTS
 $T_{Wx} = .006751$ $Cfx = 0.000000$
 $T_{Wz} = -.000067$ $Cfz = 0.000000$

DISTRIBUTION LIST

Chief of Naval Research Department of the Navy Arlington, VA 22217 ATTN: Vehicle Technology Program, Code 211 Code 430B	5	ONR Branch Office 495 Summer Street Boston, MA 02210 ATTN: Dr. A. D. Wood	1
Chief of Naval Development Department of the Navy Washington, DC 20360 ATTN: NAVMAT 0331	1	ONR Branch Office 536 South Clark Street Chicago, IL 60605 ATTN: Mr. M. A. Chaszeyka	1
Naval Air Systems Command Department of the Navy Washington, DC 20361 ATTN: NAVAIR 320D NAVAIR 5301 NAVAIR 53013	1 1 1	ONR Branch Office 1030 East Green Street Pasadena, CA 91106 ATTN: Mr. B. F. Cagle	1
David Taylor Naval Ship Research & Development Center Aviation and Surface Effects Department Bethesda, MD 20034 ATTN: Code 16 Code 522.3	1 1	Commandant of the Marine Corps Washington, DC 26320 ATTN: Dr. A. L. Slafkosky Scientific Advisor (Code RD-1)	1
Naval Research Laboratory Washington, DC 20375 ATTN: Technical Information Office, Code 2627 Library, Code 2629	1 1	Defense Documentation Center Cameron Station, Bldg. 5 Alexandria, VA 22314	12
Superintendent U. S. Naval Academy Annapolis, MD 21402	1	Contract Administrator Southeastern Area 2110 G. Street, N.W. Washington, DC 20037	1
Superintendent U. S. Naval Postgraduate School Monterey, CA 93940	1	Department of the Army DCS for Research Development and Acquisition Washington, DC 20310 ATTN: DAMA-WSA (Mr. R. L. Ballard)	1
U. S. Naval Air Development Center Warminster, PA 18974 ATTN: Code 3015	1	U. S. Army Material Command 5001 Eisenhower Avenue Alexandria, VA 22333 ATTN: AMCRD-F	1
		Director, Headquarters U. S. Army Air Mobility R&D Lab. Ames Research Center Moffett Field, CA 94035	1

Director, Ames Directorate U. S. Army Air Mobility R&D Lab. Ames Research Center Moffett Field, CA 94035	1	Lockheed Missiles & Space Co., Inc. Huntsville Research & Engineering Ctr. P. O. Box 1103 Huntsville, AL 35807 ATTN: Mr. A. Zalay	1
Director, Langley Directorate U. S. Army Air Mobility R&D Lab. Langley Research Center Hampton, VA 23665	1	Nielson Engineering & Research, Inc. 510 Clyde Avenue Mountain View, CA 94043	1
Director, Eustis Directorate U. S. Army Air Mobility R&D Lab. Fort Eustis, VA 23564	1	Northrop Corporation Ventura Division 1515 Rancho Conejo Blvd. Newbury Park, CA 91320 ATTN: Dr. A. Wortman	1
U. S. Air Force Flight Dynamics Laboratory Wright Patterson AFB, OH 45433 ATTN: PT, Prototype Division FXM, Aeromechanics Branch	1	Boeing Aircraft Company P. O. Box 3707 Seattle, WA 98124 ATTN: Dr. P. Rubbert	1
Air Force Office of Scientific Research Bldg. 410 Bolling AFB, DC 20332 ATTN: Aerospace Sciences (NA)	1	Analytical Methods, Inc. 100 - 116th Avenue, S. E. Bellevue, WA 98004 ATTN: Dr. F. Dvorak	1
National Aeronautics and Space Administration 600 Independence Avenue, SW Washington, DC 20546 ATTN: Code RAA Code RAV	1	General Dynamics/Convair Div. Kearny Mesa Plant P. O. Box 80847 San Diego, CA 92138 ATTN: Dr. E. Levinsky	1
National Aeronautics and Space Administration Ames Research Center Moffett Field, CA 94035 ATTN: Dr. T. Gregory, FAE Dr. G. Chapman, FAR	1	Virginia Polytechnic Inst. and State University Engineering Science Dept. Blacksburg, VA 24061 ATTN: Dr. D. Mook	1
National Aeronautics and Space Administration Langley Research Center Hampton, VA 23665 Subsonic, Transonic Aerodynamic Division ATTN: Dr. James F. Campbell	1	McDonnell Douglas Aircraft Company P. O. Box 516 St. Louis, MO 63166 ATTN: Dept. 241, R. B. Jenny Dept. 230, R. W. McDonald	1

Change of Address

Organizations receiving reports on the initial distribution list should confirm correct address. This list is located at the end of the report. Any change of address or distribution should be conveyed to the Office of Naval Research, Code 211, Washington, D. C. 22217.

Disposition

When this report is no longer needed, it may be transmitted to other organizations. Do not return it to the originator or the monitoring office.

Disclaimer

The findings and conclusions contained in this report are not to be construed as an official Department of Defense or Military Department position unless so designated by other official documents.

Reproduction

Reproduction in whole or in part is permitted for any purpose of the United States Government.